TOPICS IN PARTICLE PHYSICS WITH COLLIDING PROTON BEAMS

J.C. SENS

Foundation for Fundamental Research on Matter, The Netherlands and CERN, Geneva, Switzerland

Lectures presented at:

1) The Scottish Universities Summer School, July-August 1973 (Sections I-VI).
2) Summer Institute on Particle Interactions at Very High Energies, Louvain, August 1973 (Sections I, II, V, VI).

D. Speiser et al. (eds.), *Particle Interactions at Very High Energies*

I. BASIC CHARACTERISTICS OF THE CERN ISR *

I.1 Energy, Intensity of the Stored Protons

In high energy accelerators with stationary targets the total energy in the centre of mass system is given by

$$E^* \simeq \sqrt{2mE_A} \qquad \text{(I.1)}$$

(E_A = accelerator energy). In head-on colloding beam collisions this is

$$E^* = 2E_S \qquad \text{(I.2)}$$

(E_S = energy of each beam). Colliding beams with energies E_S are thus equivalent to an accelerator with an energy

$$E_A \equiv E_{eq} = \frac{2E_S^2}{m} \qquad \text{(I.3)}$$

If the colliding beams cross at angle α (I.2) and (I.3) become:

$$E^* = 2E \cos\frac{\alpha}{2} \qquad E_{eq} = m\ 2\frac{E^2}{m^2}\cos^2\frac{\alpha}{2} - 1 \qquad \text{(I.4)}$$

Currently the CERN-ISR runs at one of 5 sets of energies (GeV):

E_1/E_2	$E^* = \sqrt{s}$	E_{eq}
11.7/11.7	23	290
15.3/15.3	31	500
22.5/22.5	45	1100
26.5/26.5	53	1500
31.5/31.5	63	2100

In all other respects storage rings and equivalent accelerators are manifestly different: in storage rings the centre of mass is at rest in the laboratory, hence in particular heavy particles have a chance of being produced with low laboratory-velocity; particle detection can be done with standard, ~25 GeV type techniques, the luminosity is several orders of magnitude lower, only collisions involving p, e^+, e^- are feasible in practice,

* This is a slightly expanded version of a lecture given at the Erice Summer School 1972.

there are particular problems of detection at very small angles. Fig. 1 shows the layout of the storage rings and the accelerator from which they are fed.

The number of stored protons can be estimated by noting that, apart from a loss in the transfer, the phase space density in the accelerator which supplies the particles is equal to the phase space density of the stored beams:

$$\frac{N_S}{(\Delta p \Delta\phi)_S} = \eta \frac{N_A}{(\Delta p \Delta\phi)_A} \qquad (I.5)$$

where η = loss factor in the transfer $\simeq 0.5$
$\Delta\phi_{S/A}$ = phase width of stored/accelerated particle w.r.t. RF frequency.
$\Delta p_{S/A}$ = momentum spread of stored/accelerated particles.

The CERN PS has
$\Delta p_A \simeq 7$ MeV/c
$\Delta\phi_A = \frac{1}{8} \times 2\pi$
$N_A = 5 \times 10^{10}$ protons/bunch
(1 pulse = 20 bunches)

while at the ISR:

$$\Delta\phi_S = 2\pi \times \frac{\text{period of revolution}}{\text{bunch spacing}} = 2\pi \times \frac{3000 \text{ nsec}}{100 \text{ nsec}}$$

Hence

$$N_S = 0.9 \times 10^{12} \Delta p_S$$

With a stored momentum bite of 2% at 25 GeV, we would have

$$N_S \simeq 4.5 \times 10^{14} \text{ protons.}$$

This takes 450 PS pulses, or $\simeq$ 900 sec transfer time; the current is

$$I = \frac{Nec}{2\pi R} \simeq 20 \text{ Amp} \qquad (I.6)$$

These are design figures. In practice one has reached ~18 Amp, physics is done with $\leq$ 14 Amp beams (July 1973).

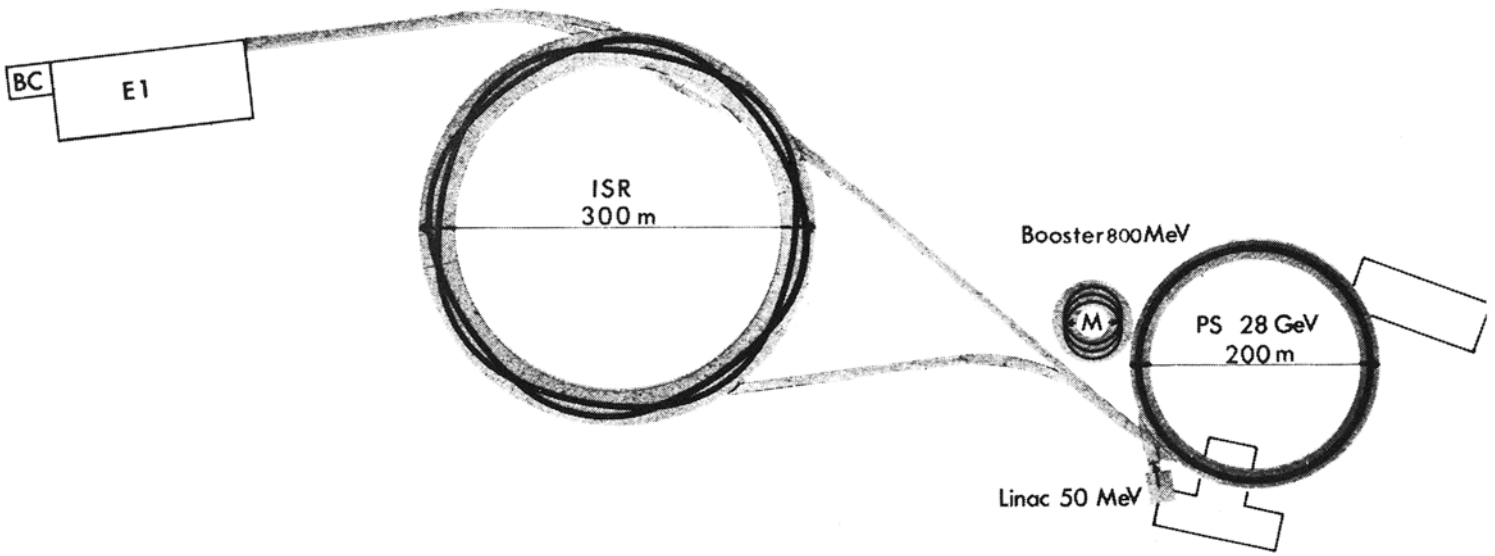

Fig. 1

Fig. 1. Layout of the CERN PS and CERN ISR. E1 = Experimental Hall for PS experiments, BC = Hall in which a large buble chamber (BEBC) is placed.

I.2 Number of Interactions

The rate of collisions leading to a particular final state is given by:

$$N_c = 2\,\sigma c \cos^2\frac{\alpha}{2} \int n_1(x,y,z)\,n_2(x,y,z)\,dxdydz \qquad (I.7)$$

σ = cross-section for collisions leading to the final state in question $n_{1,2}$ = No. of protons/cm^3 in the beams; c = velocity of the protons; α = crossing angle.

In order to prove this formula[1] we define $v_{REL} \equiv$ velocity of a proton in beam 1 w.r.t. restframe of beam 2. Then in the restframe of 2(c = 1):

$$dN = \sigma\beta_{REL}\; n_1 n_2 dtdV \qquad \text{(stat. target)} \qquad (I.8)$$

In order to obtain the equivalent of I.8 valid for any frame we put

$$dN = A\; n_1 n_2\; dtdV \qquad (I.9)$$

dN and dtdV are Lorentz invariant, hence An_1n_2 is also Lorentz invariant. In the restframe of 2, $A = \sigma\beta_{REL}$. Now the densities transform like energies, since $n_i = n_{oi}\gamma = n_{oi}\,E_i/m$, where n_{oi} is the density in the restframe of particle i. Hence AE_1E_2 and also $AE_1E_2/\underline{p}_1\underline{p}_2$ are invariants ($\underline{p}$ = 4 - vector). In the restframe of 2

$$\frac{AE_1E_2}{\underline{p}_1\underline{p}_2} \rightarrow A = \sigma\beta_{REL} \qquad (I.10)$$

Hence in an arbitrary frame

$$A = \frac{\underline{p}_1\underline{p}_2\;\sigma\beta_{REL}}{E_1E_2} \qquad (I.11)$$

and, with (I.9)

$$dN = \frac{\underline{p}_1\underline{p}_2\;\sigma\beta_{REL}}{E_1E_2}\; n_1 n_2 dtdV \qquad (I.12)$$

Now

$$\underline{p}_1\underline{p}_2 = m_1 m_2 \gamma_{REL} = m_1 m_2 (1-\beta_{REL}^2)^{-1/2} \qquad (I.13)$$

and also

$$\underline{p}_1\underline{p}_2 = E_1E_2 - \vec{p}_1\vec{p}_2 = E_1E_2(1-\vec{\beta}_1\vec{\beta}_2) = m_1m_2\gamma_1\gamma_2(1-\vec{\beta}_1\vec{\beta}_2) \qquad (I.14)$$

From (I.13), (I.14)

$$\left(\frac{\underline{p}_1\underline{p}_2}{E_1E_2}\right)^2 \beta_{REL}^2 = (1-\vec{\beta}_1\vec{\beta}_2)^2 - (1-\beta_1^2)(1-\beta_2^2)$$

$$= (\vec{\beta}_1-\vec{\beta}_2)^2 - (\vec{\beta}_1\times\vec{\beta}_2)^2 \qquad (I.15)$$

For the ISR, with equal energies in the two beams and $\beta \to 1$ we have

$$dN = 2c\sigma \cos^2\frac{\alpha}{2}\, n_1 n_2 dt dV \qquad (I.16)$$

leading to (I.7). For unequal energies, e.g. 11.8 GeV versus 31.4 GeV the correction to (I.16) is less than 0.2%.

If the protons in each ring are uniformly distributed over the circumference $2\pi R$, the beam height h and the beam width w we have

$$N_c = 2\sigma c \cos^2\frac{\alpha}{2}\left(\frac{N_S}{2\pi R h w}\right)^2 \frac{w^2 h}{\sin\alpha} \qquad (I.17)$$

The last factor is the volume of the "diamond" formed by the two crossing, rectangularly shaped beams.

$$N_c = \frac{\sigma c}{h \operatorname{tg}\frac{\alpha}{2}}\left(\frac{N_S}{2\pi R}\right)^2 = \frac{\sigma I^2}{e^2 c h \operatorname{tg}\frac{\alpha}{2}} \equiv L\sigma \qquad (I.18)$$

This defines the luminosity L of the machine; if the currents I in the two rings are not the same, and if the particle densities are not uniform we have, instead of (I.8):

$$L = \frac{I_1 I_2}{e^2 c \, \mathrm{tg}\frac{\alpha}{2} \, h_{eff}} \qquad (I.19)$$

with

$$\frac{1}{h_{eff}} = \frac{\int \rho_1(z)\rho_2(z)dz}{\int \rho_1(z)dz \int \rho_2(z)dz} \qquad (I.20)$$

$\rho_{1,2}(z)$ = the vertical density distribution in beams 1, 2. At present the effective height $h_{eff} \simeq 5$ mm, $L = 2 \times 10^{28}/\mathrm{cm}^2/\mathrm{sec}/\mathrm{Amp}^2$ in each of the 8 intersections of the ISR.

I.3 Aperture of the ISR

For each particle with momentum p there is an orbit, the equilibrium orbit, which closes on itself after each revolution. The particles oscillate around this equilibrium orbit, both in the horizontal and vertical plane, with amplitudes given by [2]:

$$y(s) = a\sqrt{\beta(s)}\cos\left[\int \frac{ds}{\beta(s)}\right] + \delta = a\sqrt{\beta(s)}\,\mathrm{Cos}\,(Q\phi(s) + \delta) \qquad (I.21)$$

$\beta(s)$ = betatron amplitude function at position s along the azimuth.
$\phi(s)$ = betatron phase function, increases by 2π per revolution.
Q = number of betatron oscillations per revolution.
a, δ = constants.

$\beta(s)$ is fixed by the focussing/defocussing properties of the magnets, which have steep gradients, by magnet imperfections and by the presence of straight sections.

If we now admit particles with different momenta into the ring, then the equilibrium orbit of a particle with momentum $p + \Delta p$ will be horizontally displaced with respect to the one with momentum p by an amount:

$$\Delta x(s) = \alpha_p(s)\frac{\Delta p}{p} \qquad (I.22)$$

where $\alpha_p(s)$ is the momentum compaction function at azimuthal position s.

Eqs (I.21) and (I.22) determine the aperture required for the stored beams. The vertical aperture is specified by the

vertical betatron amplitude $\beta_V(s)$, the horizontal aperture by both $\beta_H(s)$ and the momentum compaction function, $\alpha_p(s)$. Note that in storage rings where Δp can be very large (typically a few hundred MeV at ISR) the horizontal aperture is mainly determined by the momentum compaction. In accelerators where Δp is small (at the CERN PS $\Delta p < 10$ MeV/c) the horizontal betatron amplitude is the dominating factor.

By applying suitable quadrupole magnetic fields to the stored beams, one can make the function $\alpha_p(s) = 0$ locally (Terwilliger scheme). This has recently been applied succesfully to several intersections, where the volume of interacting particles (the "diamond") is then reduced from typically 40 x 5 x 0.5 cm^3 to just a few cm^3 without loss in luminosity.

I.4 Injection and Stacking

During the typically 20 minute long period of injection, every 2 seconds a pulse consisting of 20 bunches with ~10^{11} accelerated protons per bunch is sent through one of the transfer tunnels to the ISR. The bunch lenght is ~15nsec, spacing ~100 nsec, total time for 20 bunches 2.3 μsec. Near the ISR rings the particles pass through two septum magnets (2.2 m long, 10 KGauss each), whose function is to bend them sideways (and slightly upwards as well) without affecting the particles that are already circulating in the rings. Fig. 2 shows the trajectory after the second septum magnet. The trajectory is then made to cross the ISR "injection orbit". At the crossing point a 1.2 m long, ~3/4 KGauss, inflector magnet turns the trajectory by ~2.5 mrad onto the injection orbit. Since the ISR diameter is 1.5 x the PS diameter, the pulse train fills only 2/3 of the ISR circumference, hence after the last bunch of the pulse there is ~1 μsec to turn the inflector magnet off before the front end of the train reaches the magnet again after one revolution in the ring.

As soon as the pulse is parked on the injection orbit the R.F. is switched on at 9.54 MHz, corresponding to the bunch spacing on the injection orbit. A slow change in frequency then increases the energy and moves the orbit towards a correspondingly larger radius (see Fig.3). During this stacking process the R.F. voltage is run down from ~20 KV to a few hundred volts. When the final orbit has been reached the R.F. is switched off. Two kinds of stacking are possible. In the "repetitive stacking" scheme the newly injected pulse is always deposited at the same place near the outside of the vacuum chamber and the previously stacked particles are automatically (as a result of the requirements of phase space density conservation) pushed inwards. In this scheme both the R.F. voltage and the rate of change of frequency remain constant no matter how many pulses have already been injected. In the "non-repetitive" stacking scheme the pulses

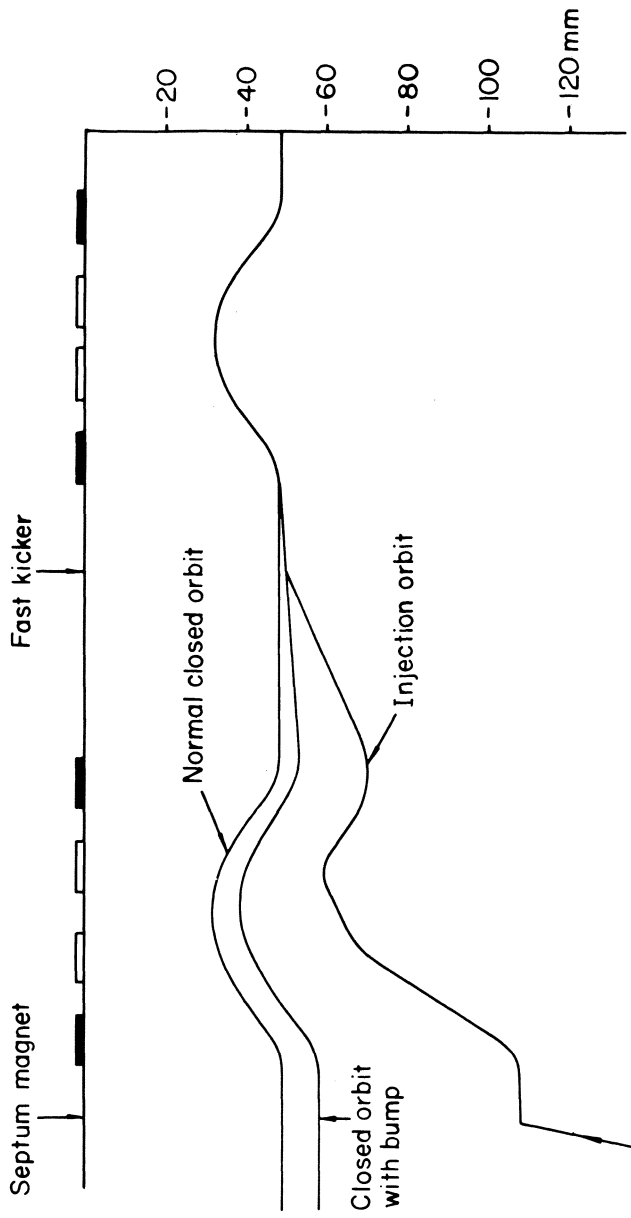

Fig. 2. Trajectory at injection into the ISR.

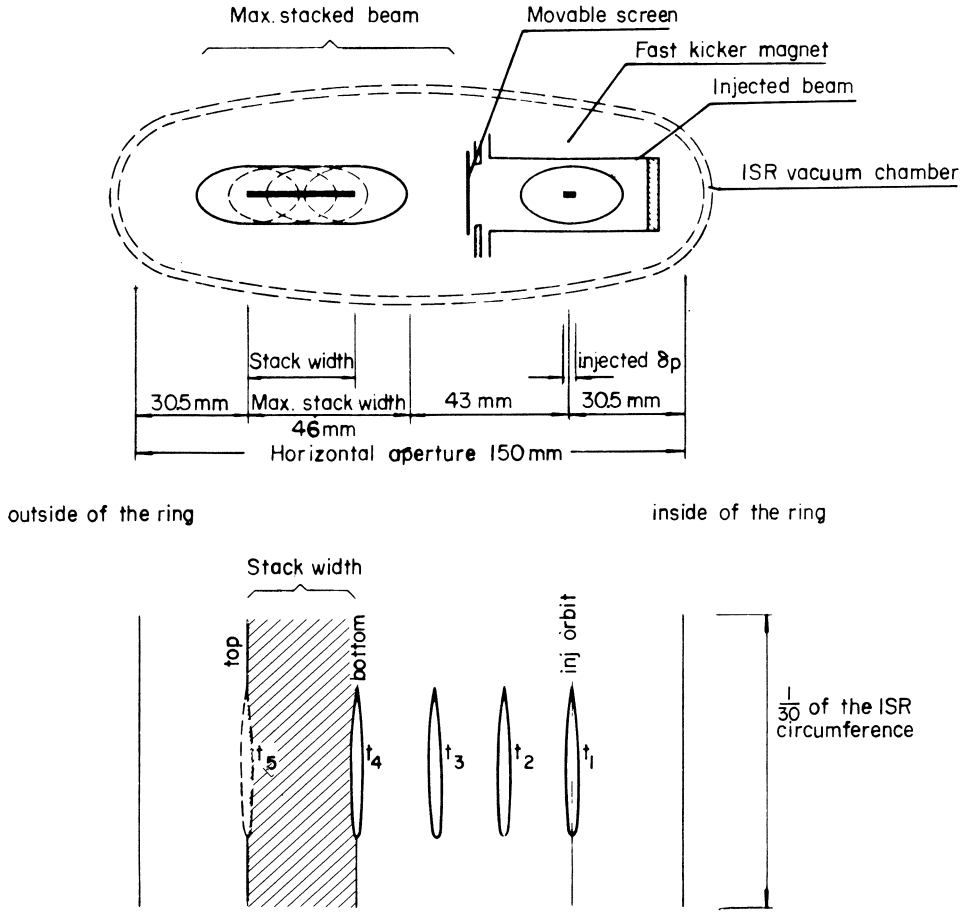

Fig. 3. Inflector magnet and stack.

are put side by side, wothout disturbing previously stacked particles. In this scheme the R.F. amplitude is not constant and the time dependence of the R.F. frequency is more complicated than in the repetitive scheme. About 4.3 KHz frequency variation will shift the beam over ~6 cm in ~2 seconds. As soon as the R.F. is switched off the beam begins to debunch (as a result of momentum spread and magnet imperfections) and will gradually fill the entire circumference. The system is then ready for the next pulse from the accelerator. The stacked DC beam is to a good approximation not affected by the R.F. voltage which transports the next pulse across the chamber.

I.5 Working Lines

It is well known that in accelerators coupling between horizontal and vertical betatron oscillations leads to beam blow up. This happens if the condition

$$nQ_H + mQ_V = k \quad n,m,k \text{ integers} \tag{I.23}$$

is satisfied by the Q - values of the machine. In storage rings where the same condition applies, there is the added complication that, as Q varies with radius, typically ~2% over a ~5 cm wide stack, there is a range of values $\Delta\Phi_H$, ΔQ_V which must all be avoided if a stable stack is to be maintained. The Q - values can be adjusted with 24 pole face windings (extra coils wound around the main bending + focussing magnets of the ring) while in addition the radial dependence of Q is adjustable by means of 8 sextupole magnets, especially installed for this purpose. Fig. 4[3] shows the Q_H, Q_V diagram of the ISR. The straight lines satisfy (I.23). The curved lines ("working lines") indicate actual stacks ("1" = inner edge, CL = centre line, "2" = outer edge). The working line "bare machine" is seen to lie across a third order resonance ($3Q_V = 26$) and was found to give unstable beams. The line "ANNA" was obtained by shifting the "bare machine" line by means of the pole face windings. The line CLEO was obtained by applying sextupole corrections with the effect of rotating the stack in the Q_H, Q_V plot. The line FATA crosses only 5th order resonances. Currents up to 6 Amp were reached with the line 15 FA.

The Q_H, Q_V diagram can be probed for resonance lines by injecting just one pulse into one ring and moving it outwards by changing the main magnetic field. An example[4] is shown in Fig. 5. A beam of ~14 mA is injected at - 32 mm with respect to the centre of the vacuum chamber. When moving the beam outwards losses occur at given radii. The corresponding Q - values satisfy the following resonance conditions:

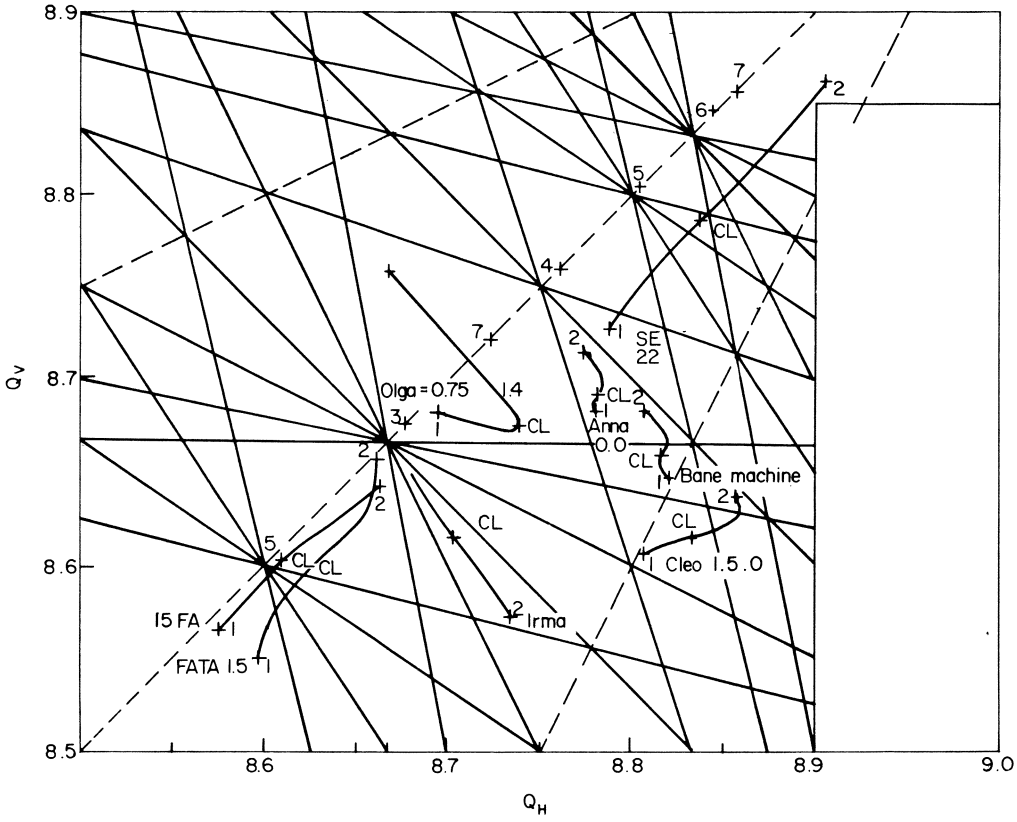

Some working lines established for ring I

1 corresponds to the injection orbit: $(\frac{\Delta p}{p}) = -0.018$

2 corresponds to a radial displacement of +42 mm from the centre line: $(\frac{\Delta p}{p}) = +0.022$

Fig. 4. Examples of working lines in the Φ_H, Φ_V plot.

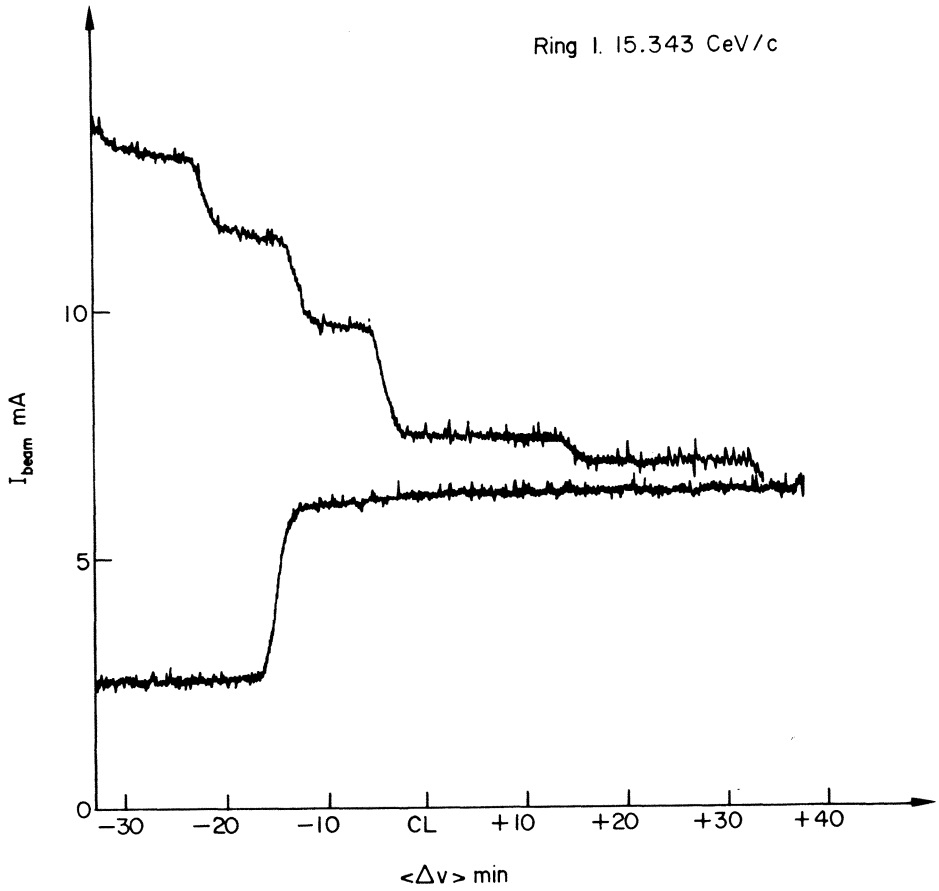

Fig. 5. Probing the Φ_H, Φ_V diagram for resonances by moving one bunch across the vacuum chamber. The bunch is displaced by changing the main magnetic field of the ISR. CL = centre of vacuum chamber. The vacuum chamber is of elliptical shape (see fig. 3), its semi long axis is 80 mm.

POSITION (mm)	RESIDUAL LOSS (%)	RESONANCE LINE
- 23 → - 21	11	$3Q_H + Q_V = 35$
- 15 → - 11	14	$3Q_V = 26$
- 5 → - 3	23	$2Q_H + 2Q_V = 35$
+ 13 → + 16	7	$3Q_V + Q_H = 35$ and others
+ 32 → + 34	7	$4Q_V = 35$

When returning the beam to the inner side further losses occur at some (not all) of the resonance radii.

Over 50 different working lines have been investigated to date.

I.6 Beam/Gas Interactions

Even if an ideal working line could be set up there would still be losses due to the interactions of the circulating protons with the residual gas. These losses fall into 3 categories. Nuclear scattering is the least serious. For a nuclear interaction cross-section on the residual gas of 400 mb and a pressure of 10^{-10} Torr the loss is 0.3% per 12 hours. Multiple Coulomb scattering results in a gradual growth of the stack. It has been computed[5] that the height h of the stack varies with time t as

$$h^2(t) = h_o^2 + 6.2 \times 10^{-5}\ t$$

(h in mm, t in sec) for a pressure of 10^{-10} Torr. It will thus take ~300 hours to double the height of a ~5 mm high stack.

Experiments indicate losses which are very much higher than expected on the basis of nuclear interactions and Coulomb scattering alone. It appears that electrons and negative ions which have been liberated by collisions are attracted to the centre of gravity of the protons and set up coherent electron - proton oscillations. The oscillations are governed by equations of the type

$$\ddot{z}_e = \Phi_e^2\, \Omega^2\, (z_e - \bar{z}_p)$$

$$\ddot{z}_p + \Phi_p^2 \Omega^2 z_p = \Phi_p^2 \Omega^2 (z_p - \bar{z}_e)$$

i.e. the driving force is provided by the distance of the electron from the mean proton position and v.v.. $\Phi_{e,p}$ are the "bounce" frequencies of one particle in the potential of the other, is the betatron oscillation frequency. Both amplitudes grow, but the electron amplitude grows faster, resulting in a "shaking out" of the electrons from the beam, after which the proton amplitude reduces until sufficient electrons have been attracted towards the beam again. A beat-pattern results. Upon reaching the walls of the vacuum chamber more electrons are liberated and the background increases further. Good vacuum, clean surfaces and clearing electrodes (plates with several KV, to suck away the electrons) are the remedy. Fig. 6 shows the striking effects of the clearing electrodes. Considerable theoretical effort is going into understanding these instabilities, see e.g. ref. 6.

I.7 Instrumentation for Beam Diagnostics

Around the ISR there is a wealth of instruments designed to contribute in one way or another to monitor the behaviour of the beams and vacuum. In order to give you a glance at what they are like, four examples are shown in figs. 7, 8, 9, 10.

Fig. 7 shows a luminescent screen monitor. It is located in the transfer lines, which connect the proton synchroton with the ISR. Beam passing through one of the fluorescent screens is made visible on a T.V. screen.

Fig. 8 shows secondary emission profile monitor (S.E.M.), also placed in the transfer lines. It consists of a number of Aluminium strips. Each strip is connected to an amplifier in which the charges liberated by the beam protons are collected. There are guard electrodes to prevent secondaries escaping from the Aluminium from travelling away. There are 2 sets of strips, separated by an isolating electrode.

Fig. 9 shows a Beam probe. This is mounted in the ISR rings themselves. It consists of Ti rods. Charge amplifiers detect at which positions the beam is intercepted.

Fig. 10 shows a Beam scraper. Thin foils are moved into the beam and used to scrape away the tails of the stack. This last device has proven very useful in reducing background from low momentum tails. These tails occasionally reach out to the wall of the vacuum chambers and produce high background in the experiments.

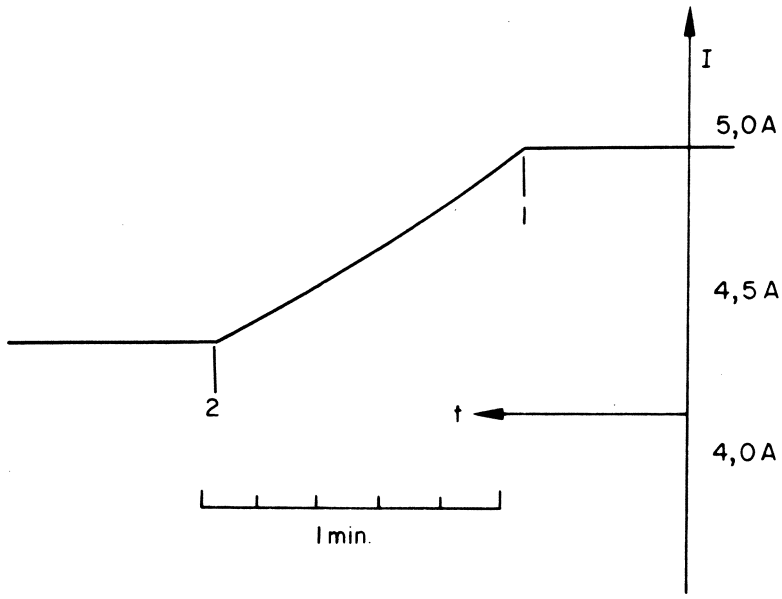

Effect on beam intensity decay of turning clearing fields off (1) and on again (2) in one octant

Fig. 6. Arresting beam decay by means of clearing electrodes.

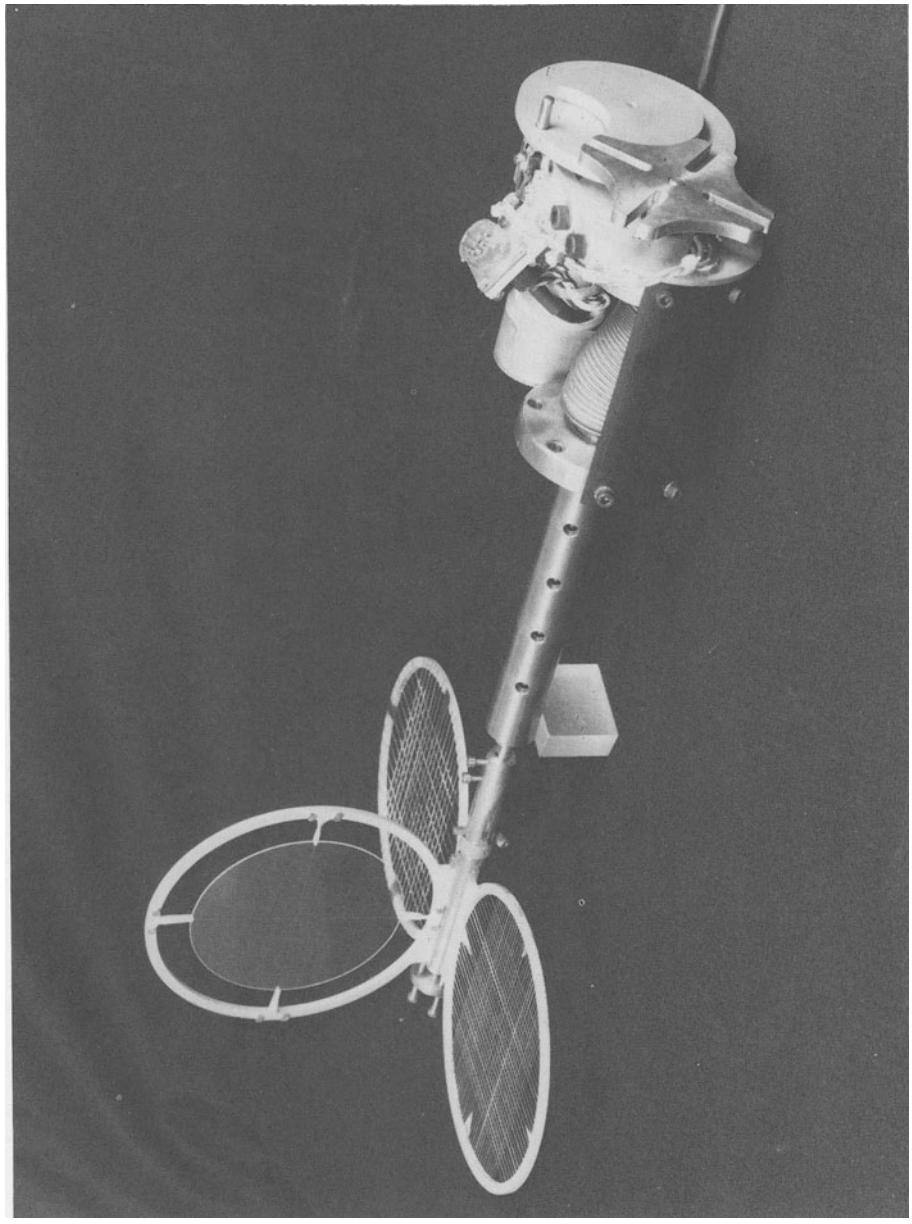

Fig. 7. Luminescent screen monitor.

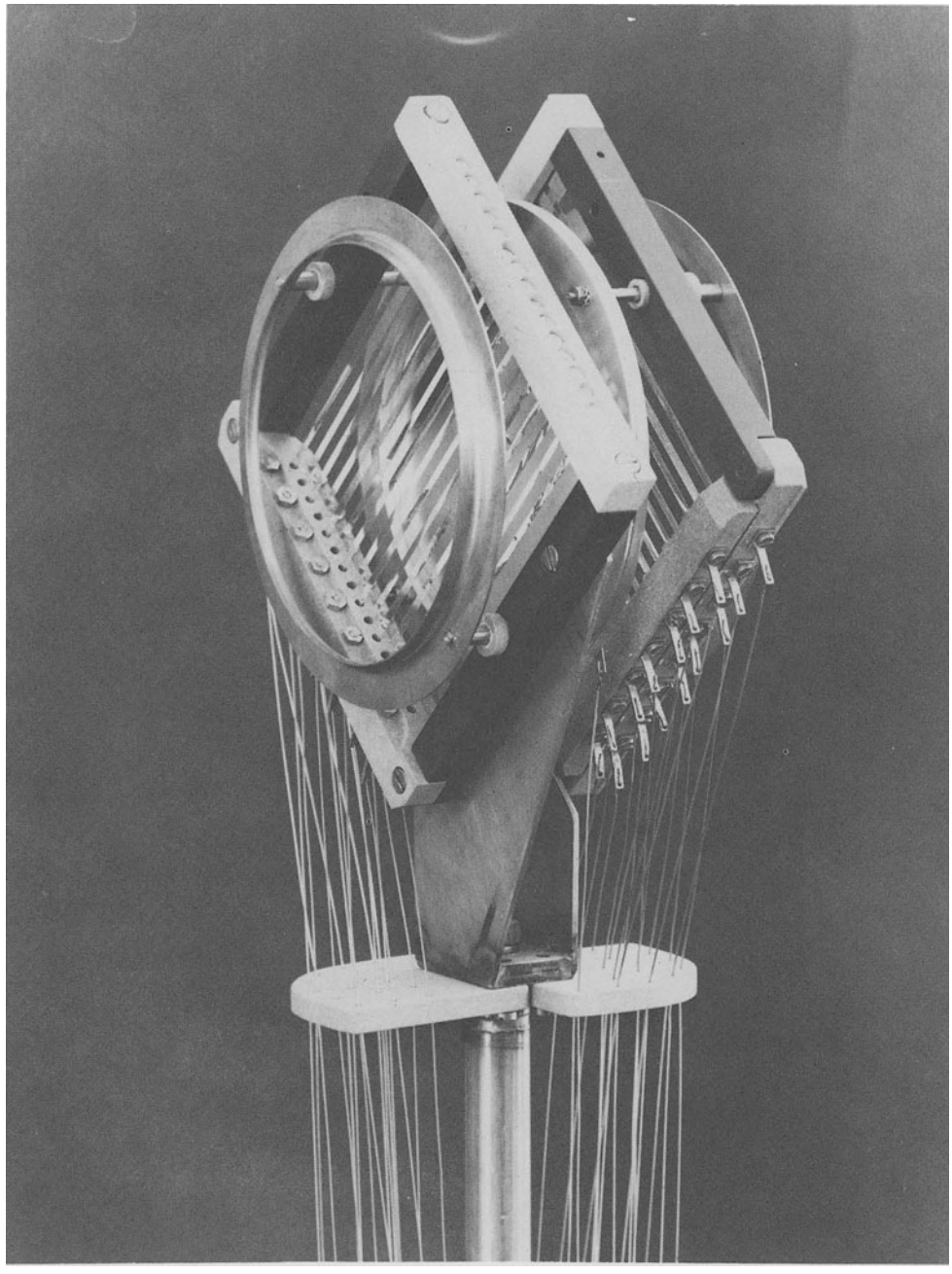

Fig. 8. Secondary emission profile monitor (S.E.M.), used to measure beam profiles in the transfer lines between PS and ISR.

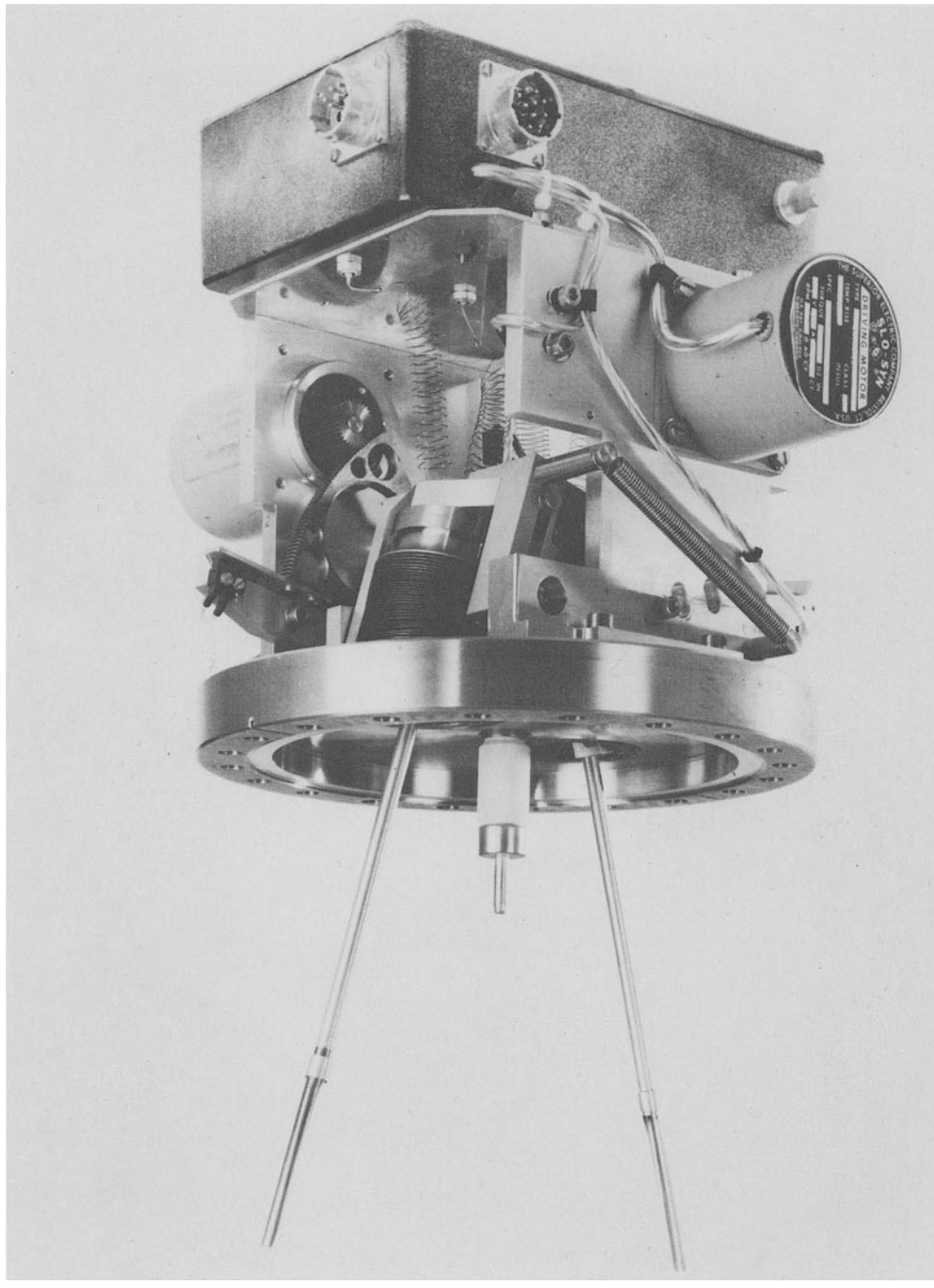

Fig. 9. Beam probe in the ISR.

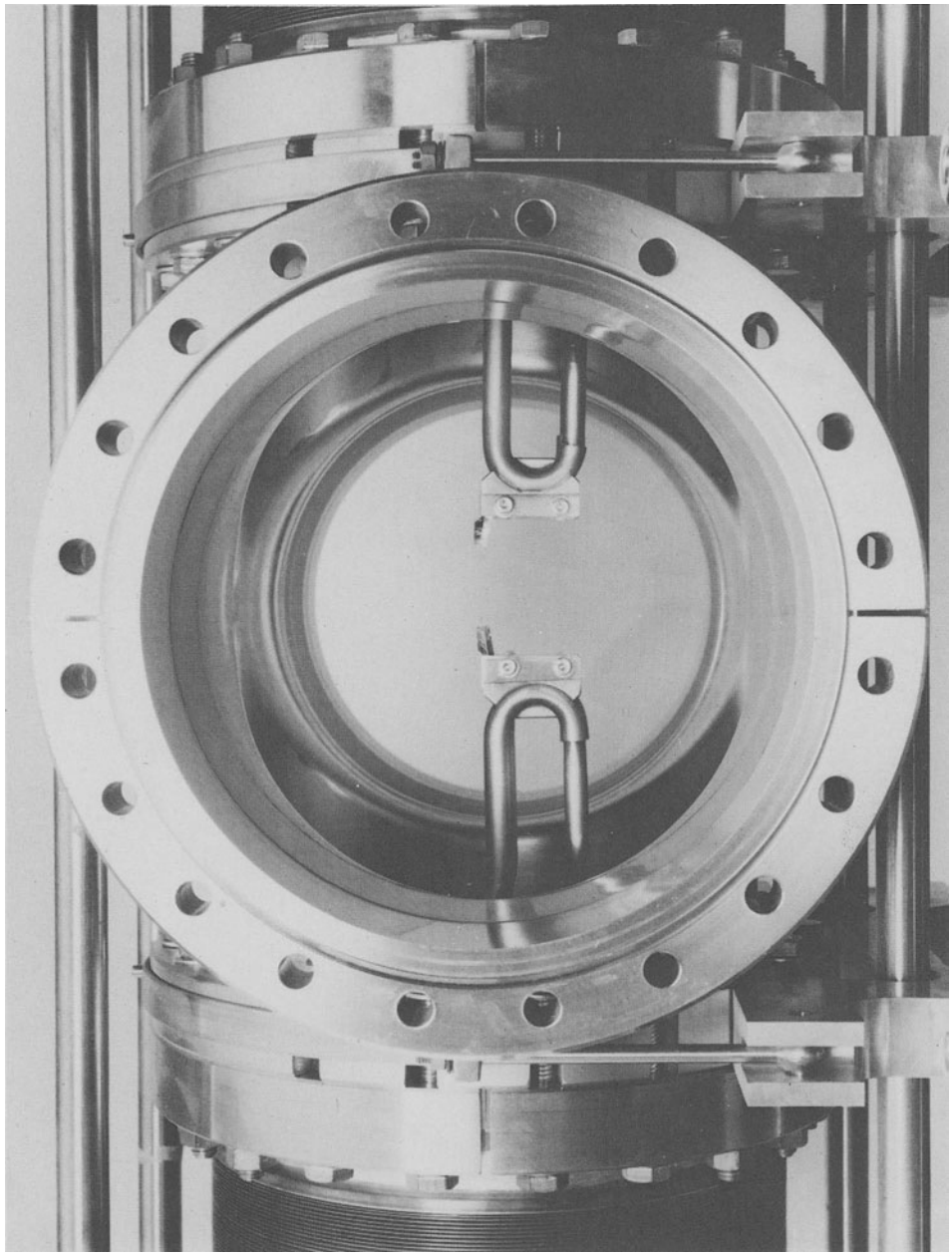

Fig. 10. Beam scraper in the ISR.

SECTION I

REFERENCES

1) L.D. Landau and E.M. Lifshitz, the classical theory of fields (12, pag. 37, revised second edition); applied to ISR e.g. in J.F. v.d. Veen, M. Sc. thesis, Un. of Utrecht (1973, unpublished).

2) E.D. Courant, H.S. Snyder, Annals of Physics 3, 1, (1958).

3) This figure and its description is taken from J.P. Gourber and K.N. Henrichsen, Proceedings of the 8th International Conference on High Energy Accelerators, CERN 1971, page 518.

4) ISR running-in reports 1971.

5) B. de Raad, Beam-gas interactions with ISR CERN 68/ISRU/IO3.

6) E. Keil, CERN 72-14 (Lectures Academic Training Programme).

II. ISR PERFORMANCE AND DEVELOPMENTS

II.1 The Luminosity and Its Measurement

The rate of collisions is given by eq. I.7

$$N_c = 2\, c \cos^2 \frac{\alpha}{2} \int n_1(x,y,z)\, n_2(x,y,z)\, dxdydz \qquad (II.1)$$

We introduce one system of coordinates per beam with z vertical, x along the beam, y perpendicular to the beam. We assume that in the region where collisions occur the density distributions are independent of x. The densities of the beams in their respective frames are then

$$n_1'(y_1,z) \quad , \quad n_2'(y_2,z) \qquad (II.2)$$

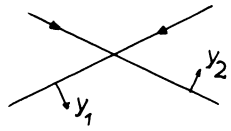

Transforming to the non-orthogonal y_1, y_2, z frame we have

$$\int n_1 n_2 dV = \int n_1'(y_1,z) n_2'(y_2,z)\, dx_1 dy_1 dz \quad \text{(beam 1 frame)} \qquad (II.3)$$

$$= \frac{1}{\sin\alpha} \int n_1'(y_1,z)\, n_1'(y_2,z)\, dy_1 dy_2 dz \quad (y_1, y_2, z \text{ frame}) \qquad (II.4)$$

Now define $S_i(z) = \int n_i'(y_i,z) dy_i \quad (i=1,2)$ (II.5)

Eq. II.1 then becomes

$$N_c = 2\sigma c \frac{\cos^2 \alpha/2}{\sin \alpha} \int S_1(z)\, S_2(z) dz$$

$$= \frac{c\sigma}{\mathrm{tg}\alpha/2} \int S_1(z)\, S_2(z)\, dz \equiv L\sigma \qquad (II.6)$$

provided the beams are uncoupled, i.e. the distributions in y_1 and y_2 are independent of each other. Note that it is not necessary that within a given beam the distributions in y and z are uncoupled, as they indeed are not in most stacks in practice.

It has been pointed out by v.d. Meer[1] that the overlap integral

$$\int S_1(z)\, S_2(z)dz \qquad \text{(II.7)}$$

can be measured by displacing the beams vertically by a distance h and measuring the collision products with a set of counters nearby. In order to keep the background from beam/gas collisions to a minimum the counters are generally put in pairs near the downstream part of the two rings, at several meters from the intersection: a coincidence between two particles emerging back to back from the intersection can kinematically not have been produced by a beam/gas collision. With distance h the counting rate is

$$R(h) = \eta \frac{c\sigma}{tg\ /2} \int S_1(z)S_2(z-h)dz \qquad \text{(II.8)}$$

where η takes accounts of geometry and efficiency factors. The rate integrated over all steps h is:

$$\int_{-\infty}^{+\infty} R(h)dh = \eta \frac{c\sigma}{tg\alpha/2} \iint S_1(z)S_2(z-h)dzdh$$

$$= \eta \frac{c\sigma}{tg\alpha/2} \int S_1(z)dz \int S_2(z-h)dh \qquad \text{(II.9)}$$

$$= \eta \frac{c\sigma}{tg\alpha/2} \int S_1(z)dz \int S_2(z)dz$$

which is proportional to (II.7). Hence by measuring R(0) and

$$\int_{-\infty}^{+\infty} R(h)dh$$

one obtains the <u>normalized</u> overlap integral:

$$\frac{R(0)}{\int_{-\infty}^{+\infty} R(h)dh} = \frac{\int S_1(z)S_2(z)dz}{\int S_1(z)dz \int S_2(z)dz} \equiv \frac{1}{h_{eff}} \qquad \text{(II.10)}$$

in a way which is independent of counter geometry and efficiencies. Eq. (II.10) defines the effective height of the system of two intersecting beams. With

$$\int S_i(z)dz = I_i/ec \qquad \text{(II.11)}$$

where I_i is the current, we have, with II.6 and II.10

$$N_c = \frac{I_1 I_2 \sigma}{e^2 \, ctg\alpha/2 \; h_{eff}} \equiv L\sigma \qquad \text{(II.12)}$$

In practice one measures only the quantity

$$\int_{-\infty}^{+\infty} R(h)dh$$

and the currents. The monitor constant $K \equiv \eta\sigma$ then follows from II.9 and II.11:

$$\int_{-\infty}^{+\infty} R(h)dh = K \frac{I_1 I_2}{e^2 c \; tg\alpha/2} \qquad \text{(II.13)}$$

Once the constant K is known, then, at any later time:

$$R_M = \text{Rate/sec in monitor} = KL \qquad \text{(II.14)}$$

and hence the counting rate in an experiment, e.g. pp → pp is related to the cross-section to be measured, e.g. σ_{EL}, by

$$N_{pp \to pp} = \frac{R_M}{K} \sigma_{pp \to pp} \qquad \text{(II.15)}$$

The conditions for validity are:

-The monitor geometry must remain unchanged between the LUM. measurement and the data taking period of the experiment.
-For each set of ISR-energies there is a different K since for counters at fixed angle the minimum visible (outside pipe) t is different for different beam energies.
-Note that the shape, height, intensity of the stack need not remain the same between the LUM. measurement and the data taking. One can dump the stack and refill the rings in between.

Some further comments:

-In practice the displacements are made by small steering magnets mounted on either side of the intersections. Some non-local effects,

~0.3 mm displacements, have been observed in "other" intersections.

-No intensity effects have been observed in the range 2/2 to 5/5 A.

-For given currents the luminosity can be increased by vertically "shaving" the beam during stacking. The best result obtained this way is

$$L = 4.4 \times 10^{30}/cm^2/sec = \text{DESIGN } L + 10\%$$

11/12A $\qquad$ h = 3.2 mm $\qquad$ $\Delta p/p = 3.8\%$

shaving down to 30%. Stacks for 4 hours.

-The steering method of v.d. Meer can be checked by measuring the profile of each beam with spark chambers and integrating to obtain the overlap integral II.7[2]. The results are

	11.8/11.8	15/15	22/22	26/26
$\frac{h_{eff}(\text{v.d.M.}) - h_{eff}(\text{profile})}{h_{eff}(\text{vdM})}$	2% -3%	-3.5%	-3.3%	+1.5% +4.0%

The current belief is that under "normal" conditions L can be measured to ~5% accuracy, while with special precautions a ~2% level can be reached.

II.2 Luminosity, Limitations and Improvements

Under present (1973) conditions the half life of the Luminosity is of order 30 hours. The main limitations are due to (we follow mainly ref. 3 in this paragraph)

A) Beam-induced deterioration of the vacuum. This effect has been described above in section I.6. Negative ions and electrons are attracted towards the beam, set up oscillations there and are shaken out. Positive ions are repelled from the beam and also strike the vacuum chamber walls. The electrostatic potential of a beam of 10A is 1.5 KV. The pressure rise, as a result of gas molecules liberated from the walls, is proportional to the number of protons and the number of gas molecules: $\Delta P \sim P.I$ (P= = pressure, I = current). Obviously there is then a critical current above which the pressure continues to rise. Note that

$$\text{nucleon density in the beam} = \frac{N}{2\pi R \pi a b}$$

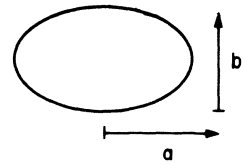

$$\text{nucleon density in gas } \frac{6 \times 10^{23}\ P.A}{22.2 \times 10^{3} \times 760} = 10^{18} P$$

(A = 28 for air, P = pressure (Torr))
For typical beam sizes the two densities are equal for P = 2 x $\times 10^{-10}$ Torr and 5 Amp. There are thus as many stationary as moving protons per cm^3 in the "beam area" of the machine.

The current remedies for this problem are:

1) Bake out of the vacuum chamber at 300°C and 24 hours every time a section is opened up. There have been 60 such bake outs in 1972.
2) Surface treatment by ions from a glow discharge from a wire in the chamber. This is done in the laboratory prior to mounting in the ISR.
3) More pumps. 500 additional Titanium sublimation pumps have been installed in 1972.
4) Beam-induced pumping. Once the walls are clear and the vacuum is good, the beam itself may act as a pump: the beam sends ions off to the walls, but the number of ions desorbed/ incident ion becomes less than one. This effect has been observed in some parts of the ISR.

B) Transverse instability due to the resistivity and inductance of the walls. This is a subject by itself and will not be discussed in details. Loosely speaking transverse instabilities are caused by coherent oscillations induced by some perturbation. The resulting local density variation is

$$\rho(z,t) = \rho_o \exp(ikz - wt). \qquad \text{(II.16)}$$

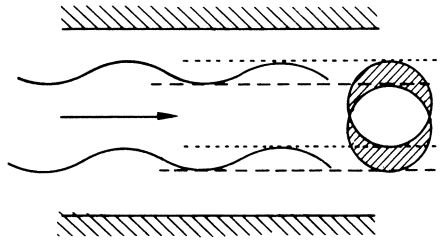

With a vacuum chamber made of metal of finite resistivity and inductance, the equations of motions resulting from this density variation will contain image charges as well. They effectively generate out of phase forces. This in turn implies an imaginary part in the frequency spectrum and an amplitude which grows with time.

The remedy lies in a judicious choice of working lines (see section I.5). A feed back system has been designed which is intended to automatically counter run-away background build-up due to these effects. This device is being tested.

The current belief is that with the presently available tools or minor additions a factor of ~2 can be gained in luminosity.

The luminosity versus time curve is shown in fig. 1.

II.3 Low β Section

Recall the expressions for the vertical and horizontal betatron amplitude (section I.3)

$$y(s) = a\sqrt{\beta}(s)\cos(\Phi\phi(s) + \delta)$$

Now since the luminosity

$$L \sim \frac{1}{h_{eff}} \sim \frac{1}{\sqrt{\beta_v}} \qquad \text{(II.17)}$$

it is of interest to consider magnet schemes in which β_v can be made as small as possible in the intersections.

The enveloppe of the betatron oscillations around 1/8 of the ISR circumference is sketched in fig. 2. The oscillating character of the curve is the result of focussing forces of the magnets, of the straight sections, etc. The enveloppe indicates the extend to which the beam is vertically compressed and expanded by the magnet lattice. (There is a corresponding curve for horizontal oscillations).

One scheme[4] to reduce β_v in an intersection is shown in fig. 3. The normal magnets are indicated by F (focussing) and D(defocussing). By placing 6 more magnets (Φ_1 -Φ_6) in each ring the enveloppe of fig. 2, dotted line, is obtained. A gain of a factor five is obtained in luminosity. The price is a narrower intersection (bad for experiments at small angle, no problem for large angle experiments) and the fact that 5 of each 6 magnets must be superconducting to reach this gain.

Design studies are also underway of an intersection in which both the betatron amplitude is reduced and the crossing angle is made equal to zero. Since the luminosity is given by

$$L_\alpha = \frac{I_1 I_2}{e^2 c\, h_{eff} \operatorname{tg}\alpha/2} \xrightarrow{\alpha \to 0} L_{\alpha=0} = \frac{I_1 I_2}{e^2 c h_{eff} w/l} \qquad \text{(II.18)}$$

(w,l = width, length of intersection) one begins to gain as soon

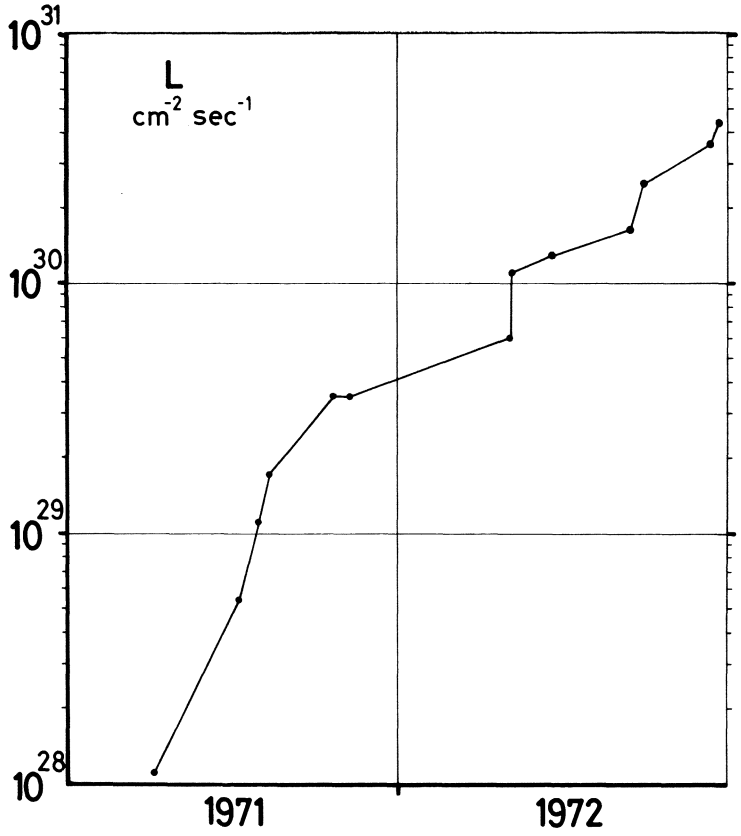

Fig. 1. The "DOW-JONES" curve of the ISR: Luminosity versus time.

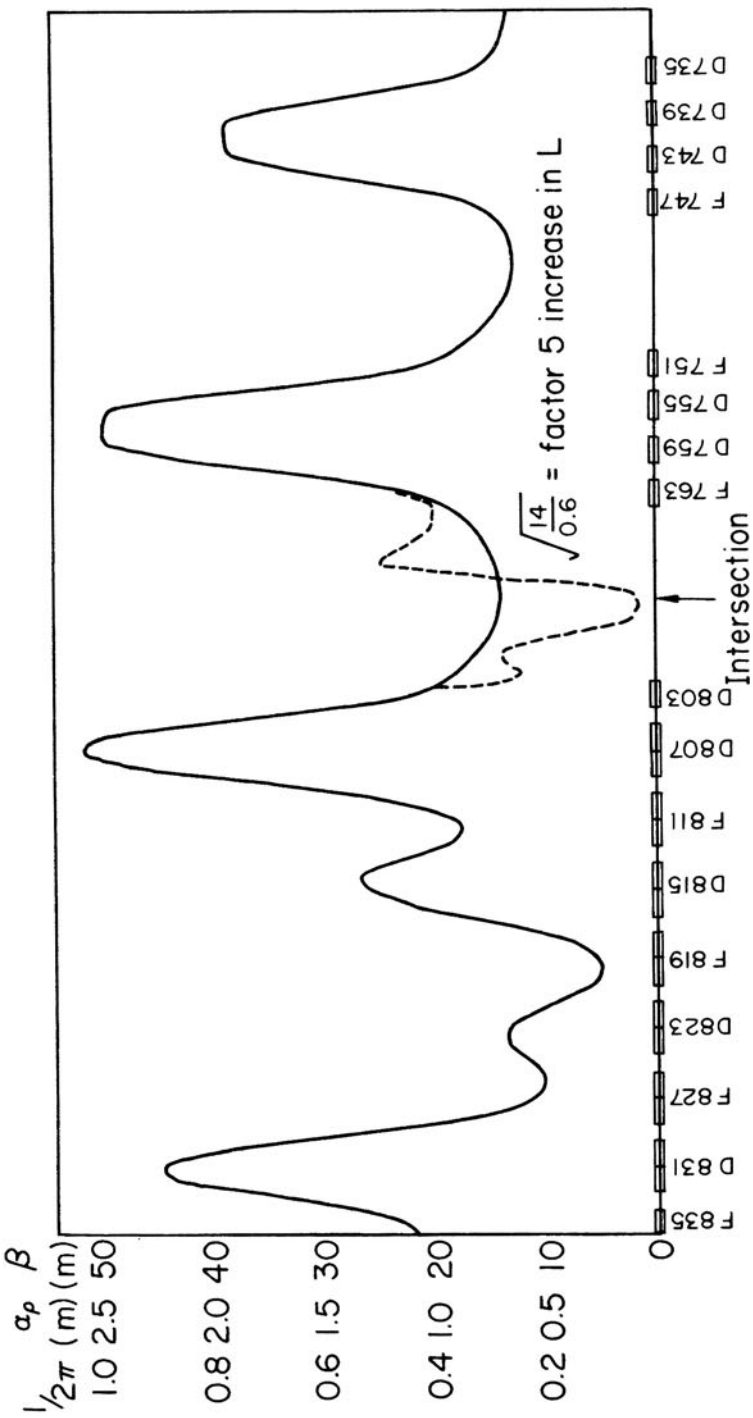

Fig. 2. Vertical betatron oscillation function versus azimuth, without and with low β section. The pattern repeats 8 times around the ISR circumference.

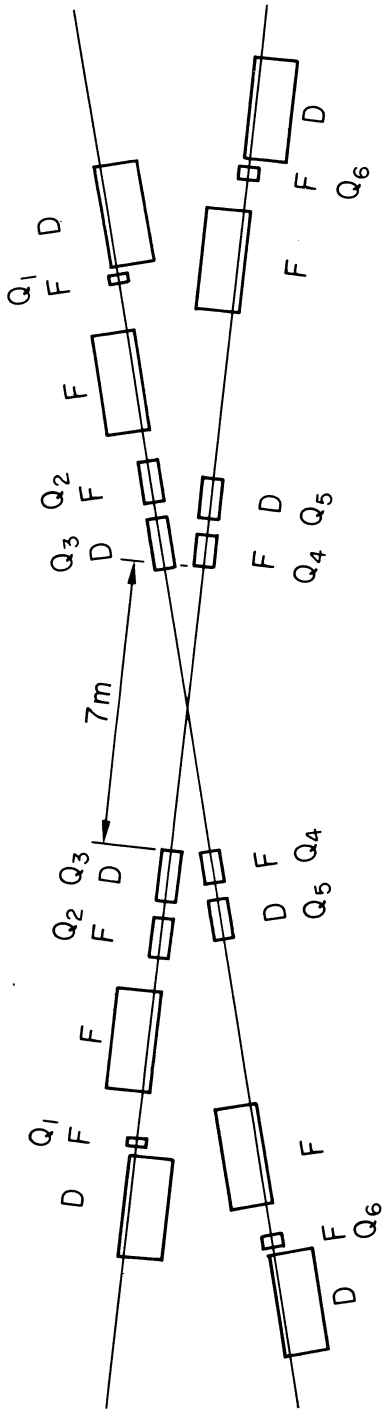

Fig. 3. Possible arrangement of magnets in a low β section. The extra magnets are $\Phi_1 \rightarrow \Phi_6$.

as $w/l < \text{tg}\ \alpha/2 = 0.13$. The luminosity then no longer depends on effective height only, but on width and length as well.

II.4 Stochastic Damping of Betatron Oscillations

An entirely different way of reducing the vertical betatron amplitude and thereby gaining in luminosity is based on the detection of the statistical fluctuations in the average position of the beam. Although the method (suggested by S.v.d. Meer) turns out not to be practical with present equipment, it represents a very interesting application of statistical mechanics to particle beams. We follow ref. 5 step by step.

Liouville's theorem implies that the density in phase space, i.e. betatron oscillations in the case at hand, cannot be influenced by magnetic fields that deflect the particles. This statement is true for an infinite number of particles and also for a finite number of particles if their positions in phase space were not known. It is manifestly not true if each particle could be located separately, since then a correction could be applied to its trajectory, resulting in a modified phase space density. Now if a beam makes coherent betatron oscillations (with all particles at a given section going up and down at the same time) it behaves to some extent as if it were one particle, and hence a correction can be applied by means of a pick-up + deflection system. But even if there are no such "explicitly" coherent betatron oscillations, for a finite number of particles some coherence would make itself felt through the statistical fluctuations in the average beam position. This is like the drunken sailor holding himself to a lamp post: due to random motion his mean square distance from the lamp post increases proportional to the number of steps, or time (up to some limit e.g. neighbouring walls). Note that if his motion were completely coherent it would be the mean distance that increases proportionally with time. Hence we have some measure of the amount of coherence in his irregular motion: it is the amount of head-way he makes compared to how much he would have made had he been sober. Now after his mean square idstance has increased for some time his arm begins to feel the strain and pulls him back to a point near the lamp post. If this pull has not sobered him up the random motions will continue and the process repeates itself. As a result of the repeated pulling of his arm the time average of the mean square distance is thus reduced.

Consider a damping system D which will react provided no less than n particles transverse it. The number n is more or less determined by the rise time of the electronics in D. The particles have oscillation amplitudes $A_1 \ldots A_n$ randomly taken from a distribution function $F(A)$ with $\int F(A)dA = 1$. The mean

square amplitude is

$$\overline{A^2} = \frac{\sum A_i^2}{n} \qquad \text{(II.19)}$$

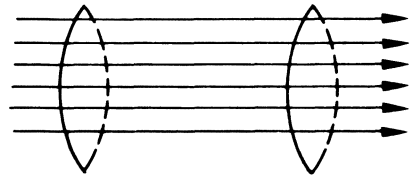

Damping system D

Each particle occupies a point in phase space characterized by

$$x_i = A_i \cos \psi_i \qquad x_i' = A_i \sin \psi_i \qquad \text{(II.20)}$$

The centre of gravity of the particles before entering D then has the coordinates

$$\bar{x} = \frac{1}{n} \sum A_i \cos\psi_i, \quad \bar{x}' = \frac{1}{n} \sum A_i \sin\psi_i \qquad \text{(II.21)}$$

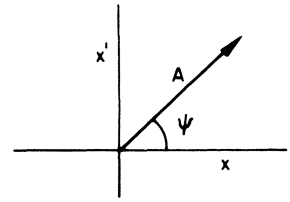

Upon entering D all particles get the same kick, such that the centre of gravity is returned to (0,0). The new position of particle i is then

$$x_{Ni} = x_i - \bar{x}, \quad x_{Ni}' = x_i' - \bar{x}'; \qquad \text{(II.22)}$$

the square of its amplitude

$$A_{Ni}^2 = x_{Ni}^2 + x_{Ni}'^2 , \qquad \text{(II.23)}$$

and the mean square amplitude

$$\overline{A_N^2} = \frac{1}{n} \sum A_{Ni}^2 \qquad \text{(II.24)}$$

$$= \frac{1}{n} \left[\sum A_i^2 - \frac{1}{n} \left\{ \left(\sum (A_i \cos\psi_i) \right)^2 + \left(\sum (A_i \sin\psi_i) \right)^2 \right\} \right]$$

The action of D thus reduces the mean square amplitude by a fraction

$$\varepsilon = \frac{\sqrt{\overline{A^2}} - \sqrt{\overline{A_N^2}}}{\sqrt{\overline{A^2}}} \simeq \frac{\overline{A^2} - \overline{A_N^2}}{2\,\overline{A^2}} = \frac{\{\sum(A_i\cos\psi_i)\}^2 + \{\sum(A_i\sin\psi_i)\}^2}{2n\,\sum A^2} \qquad \text{(II.25)}$$

for $\varepsilon \ll 1$. ε is the reduction of a given root mean square amplitude, resulting from a given distribution of amplitudes A_i. The average value of this reduction, $\bar{\varepsilon}$, is found by weighing the amplitudes by their distribution functions and integrating:

$$\bar{\varepsilon} = \int_0^\infty\!\!\cdots\int_0^{2\pi}\!\!\cdots \frac{\{\sum(A_i\cos\psi_i)\}^2 + \{\sum(A_i\sin\psi_i)\}^2}{2n\,\sum A_i^2} \cdot F(A_1)F(A_2)\cdots$$

$$\cdots F(A_n)\,\frac{1}{(2\pi)^n}\,d\psi_1 \cdots d\psi_n dA_1 \cdots dA_n \qquad \text{(II.26)}$$

Now since

$$\int_0^{2\pi}\!\!\cdots \left[\{\sum(A_i\cos\psi_i)\}^2 + \{\sum(A_i\sin\psi_i)\}^2\right] d\psi_1\cdots d\psi_n =$$

$$= (2\pi)^n\,\sum A^2$$

we have

$$\bar{\varepsilon} = \frac{1}{2n}\int\!\!\cdots F(A_1)F(A_2)\cdots F(A_n)dA_1dA_2\cdots dA_n = \frac{1}{2n} \qquad \text{(II.27)}$$

Hence on average the reduction is independent of the distribution of amplitudes. The average reduction is larger, the smaller the number of particles to which the system can react, i.e. the closer the single particle limit can be approached in the damping system D. After 2n passes through the system the r.m.s. amplitude would be reduced by a factor e, provided the sample randomizes again after each passage (i.e. provided the sailor does not sober up as a result of the pulls on his arm). The latter condition is easily met in the ISR since a package of n particles, with a momentum spread of 2%, traversing D changes its population before traversing it again, as a result of the 25 cm longer circumference for the maximum compared with the minimum momentum

particles.

Why can this method, although feasible in concept, not be realized in practice? The answer is that the number of particles "seen" within the rise time of any present day electronics is necessarily too large. Suppose the rise time of D is τ and the time for one revolution is T_R (= 3 μsec). Then

$$n = N \frac{\tau}{T_R} \qquad \text{(II.28)}$$

where N is the total number of particles in the ring. From (II.27) and (II.28) we then have for the damping time constant T_d

$$T_d = 2n\, T_R = 2n \frac{N\tau}{n} = 2\, N\tau$$

for a rise time of 0.2 nsec and $N = 4 \times 10^{14}$, $T_d \simeq 40$ hours, which is too long for damping practical stacks. Obviously, a short-armed sailor will on average stray less far from the lamp post than his long-armed friend in the same condition.

II.5 Storage of Antiprotons?

The 400 GeV CERN super proton synchrotron (SPS), presently under construction, will be equipped with a station for extracting external beams which is located at only ~200 meter from the storage rings (see fig.4). This raises hopes that one might be able to use the external SPS proton beam to produce a relatively large number of antiprotons (compared to what could be produced at the 25 GeV PS) from an external target and guide them into one one of the two storage rings, the other one being filled with protons from the 25 GeV PS as usual. The interest of having high energy (say 11 - 25 GeV) antiprotons colliding with protons lies in the possibility of measuring the total cross-section $\bar{p}p$ in a range of c.m. energies where the pp cross-section has been shown recently to rise by ~10%. A measurement of $\sigma(\bar{p}p)$ in the same energy range would put strong constraints on current "asymptotic freedom". Fig. 5 illustrates the present status of the data on $\sigma(pp)$ and $\sigma(\bar{p}p)$.

The scheme of filling one ring with antiprotons from the SPS has been considered by Hübner, ref. 6. We shall repeat here the calculation of the expected rate of collisions, with the exception that experimentally measured[7] rates at ISR energies are used instead of models to estimate the expected $\bar{p}$ yields.

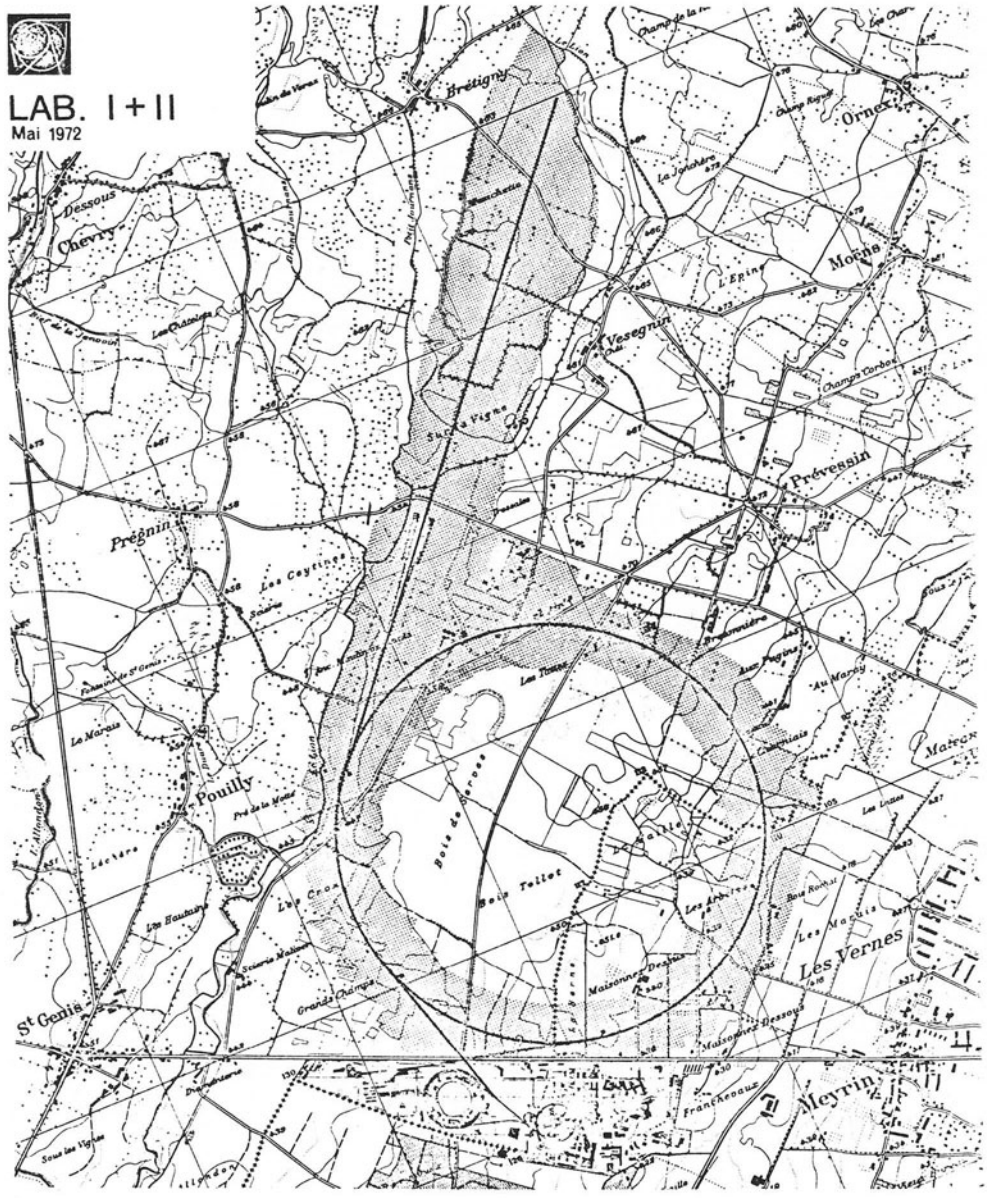

Fig. 4. Layout of the CERN SPS, ISR and PS. The extracted beam emerging from the SPS towards the left passes the ISR at ≲ 200 meter.

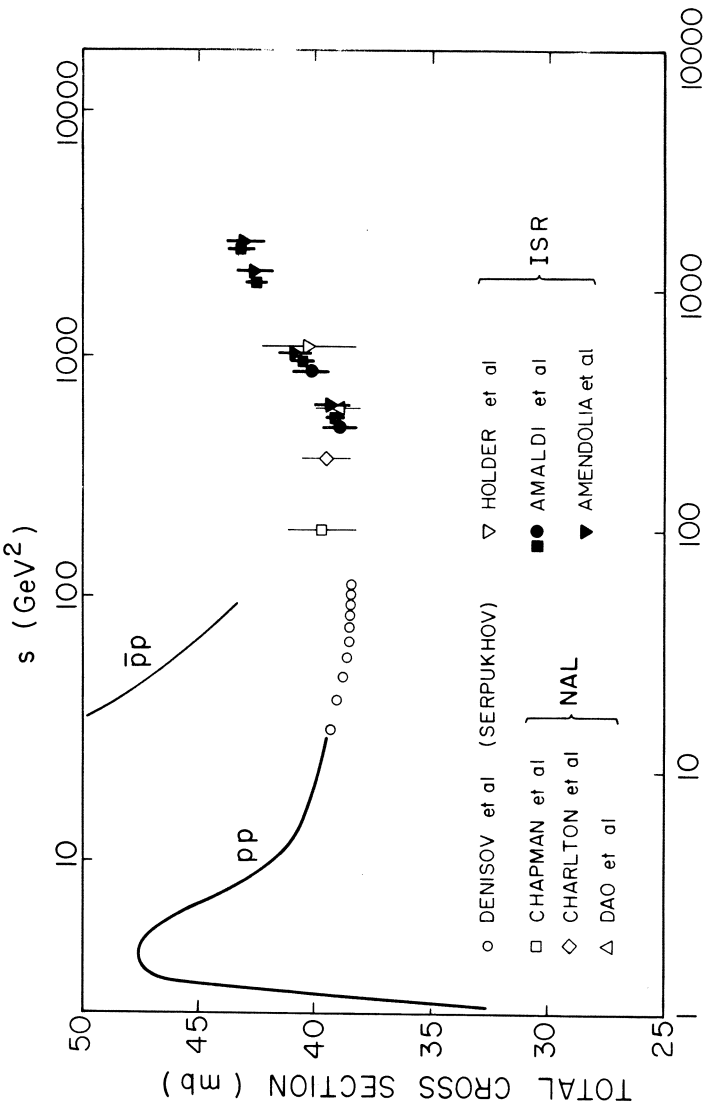

Fig. 5. Present status of total cross-section data on pp and $\bar{p}p$.

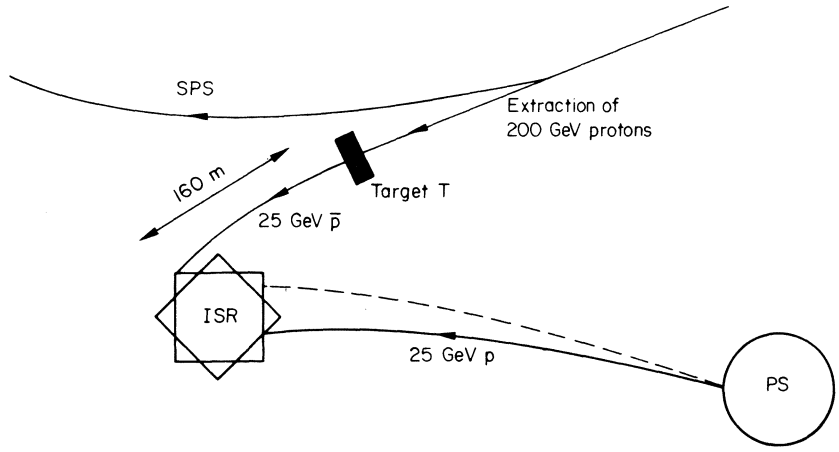

Notations:

λ_p = line density (No. of particles/cm path length) of the SPS external proton beam

$\lambda_{\bar{p}}$ = line density of the $\bar{p}$ beam produced in target T

n = number of nucleons in T/cm^3

x = thickness of T

$\frac{d^2\sigma}{dpd\Omega}$ = diff. cross-section for the production of 25 GeV p by protons; it is assumed that for reasons of shielding, bending power etc., the highest extracted proton energy is 200 GeV.

The line density of antiprotons produced is then:

$$\lambda_{\bar{p}} = \lambda_p \, n x \eta_T \frac{d^2\sigma}{dpd\Omega} \Delta p \Delta\Omega \qquad \text{(II.29)}$$

After transport from T to ISR

$$N_{\bar{p}} = 2\pi R \, \lambda_{\bar{p}} = \lambda_p \, 2\pi R \, n x \frac{d^2\sigma}{dpd\Omega} \Delta p \Delta\Omega \, \eta_t \cdot \eta_T \cdot \eta_s$$

$$= \lambda_p \left(\eta_t \frac{d^2N}{dpd\Omega} \Delta\Omega \right) \left(2\pi R \frac{\Delta p}{p} p \, \eta_t \cdot \eta_s \right) \qquad \text{(II.30)}$$

↑ ↑ ↑

SPS TARGET + TRANSFER INJECTION + RF ISR

Here

R = the radius of the ISR; $2\pi R = 10^5$ cm

η_T = the efficiency of the target in producing 25 GeV $\bar{p}$ from 200 GeV p. η_T is determined by the shape of the target, Coulomb scattering etc. Typically, for a Ø = 1 mm wire 20 - 30 cm long $\eta_T \simeq e^{-1}$.

η_t = efficiency for trapping in the ISR, determined by alignment, aberrations in the focussing lenses, the ISR inflector magnet, and mostly by the RF system. Experience with the ISR beam transfer suggests $\eta_t \simeq 0.35$.

η_s = stacking efficiency: the efficiency for accelerating the antiprotons after arrival in the ISR in order to make a stack (see section I.4). Estimate $\eta_s \simeq 0.5$.

$\frac{\Delta p}{p}$ = 2% the maximum momentum bite the ISR can hold.

$\Delta\Omega$ = solid angle seen by the $\bar{p}$ transport system from the target. For a "matched" target/beam transport system this number is typically $\simeq \pi \times 10^{-4}$sr.

In order to calculate the line density λ_p the bunch structure of both the PS, which serves as an injector to the SPS, and the SPS must be taken into account. The PS has 20 bunches/pulse. The rep. rate is ~1 pulse/2sec and each bunch is ~30 nsec long. With 10^{13} proton/pulse in the PS we have $10^{13}/20 = 5 \times 10^{11}$ protons/bunch. The RF of the SPS is arranged such that 1 SPS bunch is 5 nsec at the beginning of the acceleration cycle and has shrunk to 1 nsec after acceleration. Hence

$$1 \text{ SPS bunch} = 5 \times 10^{11} \times \frac{5 \text{ nsec}}{30 \text{ nsec}} \times \frac{1}{2} = 4 \times 10^{10} \frac{\text{proton/SPS}}{\text{bunch}}$$

allowing for an efficiency of $\frac{1}{2}$ in the transfer PS → SPS. After acceleration, when 1 SPS bunch = 1 nsec, we have

$$\frac{4 \times 10^{10}}{10^{-9}} = 4 \times 10^{19} \text{ protons/sec}$$

and

$$\lambda_p = \frac{4 \times 10^{19}}{3 \times 10^{10}} = 1.3 \times 10^9 \text{ protons/cm} \qquad \text{(II.31)}$$

in the beam line between SPS and the target T.

In order to estimate the yield of antiprotons produced by 200 GeV SPS protons, we use information recently obtained in single particle production experiments at the ISR. At $s = 2820$ GeV^2, $p_T = 0.17$, $x = 2p_L/\sqrt{s} = 0.12$, the invariant diff. cross-section has been measured to be

$$\frac{E}{p^2}\frac{d^2\sigma}{dpd\Omega} = 0.6 \text{ mb/GeV}^2$$

To translate this into the required yield we assume scaling down to $s = 378$ GeV^2, equivalent to 200 GeV p_{lab}. This is a rough approximation since there is no exact scaling for $\bar{p}$ in the ISR energy range. Furthermore we take the p_T dependence of ISR $\bar{p}$ data to extrapolate from $p_T = 0.17$ to $p_T = 0$ GeV/c:

$$\frac{E}{p^2}\frac{d^2\sigma}{dpd\Omega} = A \exp(-Bp_T^2) \text{ with } B = 2.8$$

$$\rightarrow \left.\frac{E}{p^2}\frac{d^2\sigma}{dpd\Omega}\right|_{p_T=0} = 0.65 \text{ mb/GeV}^2$$

Noting that:

$$p_{LAB} = 200 \text{ GeV} \rightarrow \gamma_{cm} = 10.3 \quad \beta_{cm} = 0.99$$

$$x = 0.12 \rightarrow p_{\bar{p}}^{*} = 1.2 \text{ GeV/c} \rightarrow p_{\bar{p}}^{LAB} = 28 \text{ GeV/c}$$

close enough to the 25 GeV/c considered above, we then evaluate the invariant cross-section at $s = 378$ GeV^2 and

$p_{\bar{p}}^{LAB} = 28$ GeV/c, $p_T = 0$ in the lab system:

$$\left(\frac{d^2\sigma}{dpd\Omega}\right)_{LAB} = 0.65 \times \frac{p^2}{E_{\bar{p}LAB}} \frac{}{p_{LAB}} = 18 \text{ mb/GeV/c/sr}$$

Hence the yield of antiprotons is

$$\frac{dN}{dpd\Omega} = \frac{1}{\sigma_{TOT}} \frac{d^2\sigma}{dpd\Omega} = 0.45 \ \bar{p}/\text{GeV/c/sr/interacting proton} \qquad \text{(II.32)}$$

Substitution into eq. (II.30) then gives for the numbers of antiprotons storable in the ISR:

$$N_{\bar{p}} = 7 \times 10^8 = 35 \ \mu A \qquad \text{(II.33)}$$

resulting in a luminosity

$$L = \frac{I_1 I_2}{e^2 \text{ctg} \frac{\alpha}{2} h_{eff}} = 0.5 \times 10^{25}/\text{cm}^2/\text{sec} \qquad \text{(II.34)}$$

assuming a 20A proton beam in the other ring. This is 6 orders of magnitude lower than the maximum luminosity for pp collision. The number of $\bar{p}p$ collisions is

$$N_{coll\bar{p}p} = 0.5 \times 10^{25} \times 40 \times 10^{-27} = 0.2 \text{ events/sec} \qquad \text{(II.35)}$$

It is estimated in ref. 6 that the time needed to store the antiprotons into the ISR is of the order of 3 hours.

It must be stressed that since this is a lecture, not a design study, the above calculation is meant to illustrate how one can go about getting the right answer, not to present a verdict as to whether storing antiprotons is feasible or not. The only definite conclusion is that the rate is very much on the edge of what one can do experiments with, even if the combined efficiency factors could be increased by an order of magnitude, as is perhaps possible in rigorous optimization of the parameters (primary energy, target dimensions, aperture of the ISR inflector etc.). On the other hand the rates obtained from estimates such as the one above do not a priori exclude the possibility of $\bar{p}p$ colliding beam experiments and hence make it of great interest to pursue this tantalizing problem in more detail.

SECTION II

REFERENCES

1) S. v.d. Meer, CERN Internal Report, ISR-PO/68-31 (1968).

2) Amendolia et al., contribution to the Int. Conf. on Instrumentation for High Energy Physics, Frascati, 8-12 May 1970.

3) W. Schnell, operating results from ISR, ISR-RF/73-7.

4) See e.g. K. Johnsen, Summary of present thinking on high luminosity insertions in the ISR, CERN/ISR-DI/73-18.

5) S. v.d. Meer, Stochastic damping of betatron oscillations in the ISR, CERN/ISR-PO/72-31 (1972).

6) K. Hübner, The storage of antiprotons in the ISR, CERN/ISR-TH/73-19.

7) M.G. Albrow et al., Nucl. Phys. B56, 333, 1973.

III. ONE PARTICLE INCLUSIVE DISTRIBUTIONS

This topic has been the subject of numerous reviews. The intention here is to write down the Mueller/Regge formulation of single particle production, to bring out some features of data taking and analysis, and to show recent results.

III.1 Three Particle Optical Theorem

The[1] two particle optical theorem states that, in order to compute the total cross-section for $a + b \to .....$ it is not necessary to evaluate

$$\sum(\text{all ampl. } a + b \to .....)$$

but, instead, it is sufficient to know the quantity

$$\text{Im (elastic ampl. } a + b \to a + b \text{ at } t = 0)$$

This is summarized in statements such as

$$\sigma_T = \frac{1}{s} \text{Im} < i \mid T \mid i > = \frac{1}{s} \text{Im } F(s,t=0) = \frac{1}{s} \text{DISC}_s \, T_{ab}(s) \qquad \text{(III.1)}$$

in obvious notations, or pictorially as:

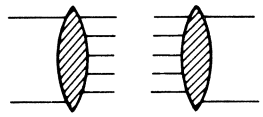

The three particle optical theorem states that, in order to compute the differential cross-section for the inclusive production of particle c for $a + b \to c + ...$ it is not necessary to evaluate

$$\sum(\text{all ampl. } a + b \to c + ...) =$$

$$\sum(\text{all ampl. } a + b + \bar{c}(p,\theta) \to .....)$$

but, instead it is sufficient to know the quantity

$$\text{Im(elastic ampl. } a + b + \bar{c} \to a + b + \bar{c} \text{ at } t = 0)$$

i.e.

$$E_c \frac{d^3\sigma}{dp_c^3} = \frac{1}{s} \mathrm{Im} \langle ab\bar{c} \mid T \mid ab\bar{c} \rangle = \frac{1}{s} \mathrm{Im} F(s_{ac}, s_{bc}, M^2) =$$

$$= \frac{1}{s} \mathrm{DISC}_{M^2} T_{ab\bar{c}}(s_{ac}, s_{bc}, M^2) \qquad \text{(III.2)}$$

pictorially:

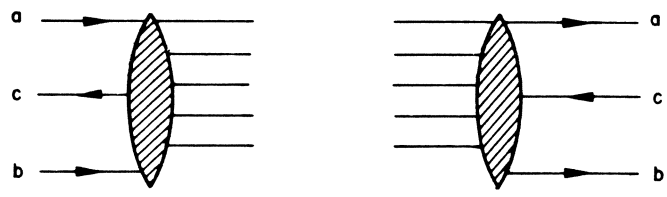

Writing $F(s,t)$ as a sum of Reggeon-exchange amplitudes we have

$$F(s,t) = \sum_i \gamma(t) \frac{1 \pm e^{-i\pi\alpha_i(t)}}{\sin\pi\alpha_i(t)} s^{\alpha_i(t)}$$

RESIDUE SIGNATURE (Im = ±1) ENERGY DEPENDENCE

This expansion is valid at high energy, hence the rule: whenever the energy (subenergy) → ∞, replace blob (sub-blob) by Reggeons.

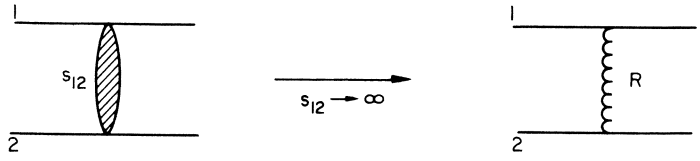

This then gives rise to two regions: the central region and the fragmentation region. In the central region (CR) both subenergies $s_{ac} \to \infty$ and $s_{bc} \to \infty$ as $s \to \infty$ and hence

$$F(s_{ac}, s_{bc}, M^2) \to \sum \gamma_{aR}\gamma_{bR'}\gamma_{RR'c} (s_{ac})^{\alpha_R}(s_{bc})^{\alpha_{R'}} \qquad \text{(III.3)}$$

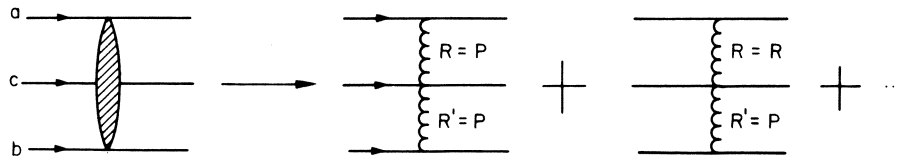

Now note that generally

$$\underline{p} = (0,0,m_T \sinh y,\ i\, m_T \cosh y)$$

$$y = \mathrm{tgh}^{-1}\,\beta \quad ; \quad m_T = (p_T^2 + m^2)^{1/2}$$

$$\vec{p} = m_T \sinh y \simeq \pm \frac{1}{2} m_T \exp(\pm y)$$

$$s_{ac} = (\underline{p_a} - \underline{p_c})^2 \simeq 4 p_a p_c \simeq m_a m_c \exp(y_a - y_c)$$

$$s_{bc} = (\underline{p_b} - \underline{p_c})^2 \simeq 4 p_b p_c \simeq m_b m_c \exp(y_c - y_b)$$

$$s = (\underline{p_a} + \underline{p_b})^2 \simeq 4 p_a p_b \simeq m_a m_b \exp(y_a - y_b)$$

Hence $s = s_{ac}\, s_{bc}/m_c^2$
Hence the first term in (III.3), with R = R', given for (III.2)

$$E_c \frac{d^3\sigma}{dp_c^3} = \frac{1}{s} \sum \gamma_{aR} \gamma_{bR} \gamma_{RRc} (s_{ac})^R (s_{bc})^R = G_{RRc}(p_{T_c}^2)\, s^{\alpha_R - 1} \qquad \text{(III.4)}$$

Hence for Pomeron exchange only, there would be neither s nor y-dependence in the invariant cross-section in the central region: the Mueller/Regge expansion results in Feynman scaling. The next term would be R = Reggeon, R' = Pomeron

$$E_c \frac{d^3\sigma}{dp_c^3} = \frac{1}{s} \left[\gamma_{aR} \gamma_{bP}\, s_{ac}^{\alpha_R}\, s_{bc}^{\alpha_P} + \gamma_{bR} \gamma_{aP}\, s_{ac}^{\alpha_P}\, s_{bc}^{\alpha_R} \right] G_{PRc}(p_{T_c}^2)$$

For $s_{ac} \simeq s_{bc}$, $\alpha_P \simeq 1$ and a = b this is

$$E_c \frac{d^2\sigma}{dp_c^3} = \gamma_{aR}\gamma_{aP} \left(\frac{1}{s^{1/2}}\right)^{\alpha_P - \alpha_R} H_{PRc}(p_{T_c}^2, y_c) \qquad \text{(III.5)}$$

Since $\alpha_R \simeq 1/2$ the approach to scaling goes approximately as $s^{1/4}$.

In the fragmentation region (FR), where particle c is considered to be a break up product of, say, particle b we have

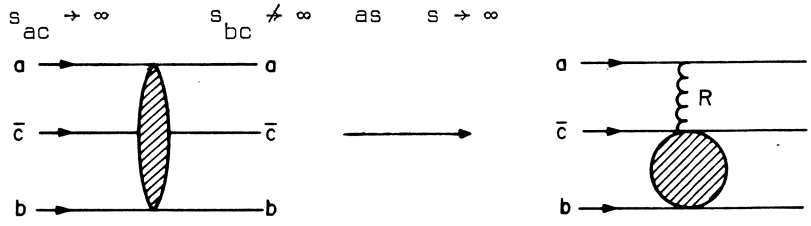

and hence only one amplitude is now Reggeized, the other exchange is still represented by a blob.

$$E_c \frac{d^3\sigma}{dp_c^3} = \frac{1}{s} \sum \gamma_{aR} s_{ac}^{\alpha_R} \phi_{bcR}(y_b - y_c, p_{T_c}^2) \qquad \text{(III.6)}$$

REGGE AMPL. — BLOB FUNCTION

Now $s = m_a m_b \exp(y_b - y_a)$

$$s_{ac} = m_a m_c \exp(y_c - y_a + y_b - y_b)$$

$$= \frac{s}{m_b} m_c \exp(y_c - y_b) \to s \exp(y_c - y_b)$$

and thus

$$E_c \frac{d^3\sigma}{dp_c^3} = \sum s^{\alpha_R - 1} G(y_b - y_c, p_{T_c}^2) \qquad \text{(III.8)}$$

In particular if R = Pomeron,

$$E_c \frac{d^3}{dp_c^3} = G(y_b - y_c, p_{T_c}^2)$$

Hence the invariant cross-section in FR is a function of $y_b - y_c$ and, to leading order, independent of s: the Mueller/Regge expansion results in limiting fragmentation (Yang) and Feynman scaling in FR.

The next term is R = Reggeon, and from (III.8) we then have that the approach to scaling in FR goes as $s^{-1/2}$.

III.2 Experiments and Results on Inclusive Single Particle Production

There is no such thing as "typical apparatus" around the ISR; different particles (π°, K° versus charged particles) and different angular or rapidity ranges require different techniques. One piece of equipment, with which some of the problems that arise in the data analysis can usefully be illustrated is a two magnet spectrometer, placed on a rotating table, with which angles between 36° and 90° can be scanned[2]. It is shown in fig. 1. There are scintillation hodoscopes $H_1H_2H_3$ forming the trigger and 6 spark chambers with magnetostrictive readout. The chambers are used to get straight line segments from the spark locations. A track is considered "good" if the appropriate segments meet in both magnets. An event is considered "good" if the track matches the hodoscope pattern. In this selection a number of real events get lost, since for example, some of the spark chambers did not fire when they should have. How is it that one does not loose normalization in this selection process?

In order to normalize data, i.e. turn numbers of tracks, characterized by a momentum $p \pm dp$ and angle of production $\theta \pm d\theta$ into mb/sr/GeV/c one requires a "monitor", a set of counters which intercepts a fixed fraction of the collisions products, which remains unchanged in geometry, momentum cut-off etc. throughout the experiment, and whose counting rate has a known relation to the luminosity:

$$R_M = \text{mon. rate/sec} = KL \qquad \text{(III.9)}$$

This relation is obtained in a luminosity measurement as discussed in section II.

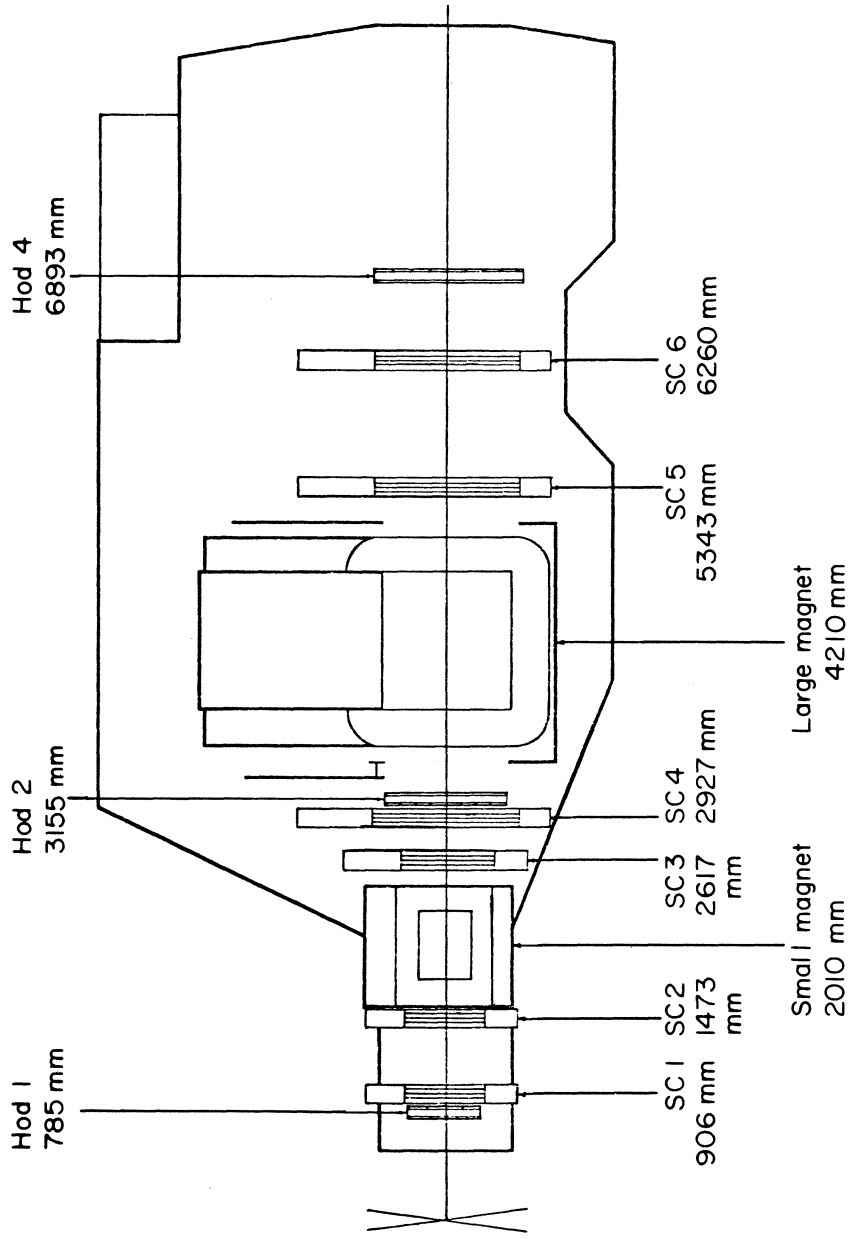

Fig. 1. Layout of a spectrometer for measuring single particle distributions at 90° w.r.t. the colliding beams.

If during the time the spectrometer is taking data, we also count the events in the monitor $\sum R_M$ we obtain, with K, the required relation between events and cross-section. Now after each trigger (e.g. an $H_1H_2H_3$ coincidence) there is a tranfer of the chamber + counter information to magnetic tape. One of the scalers whose content is transferred is the monitor scaler. It usually contains some 10 to 100 counts per event. After the transfer the scalers are reset to zero and ready to start counting again until the next transfer. Hence the pattern is:

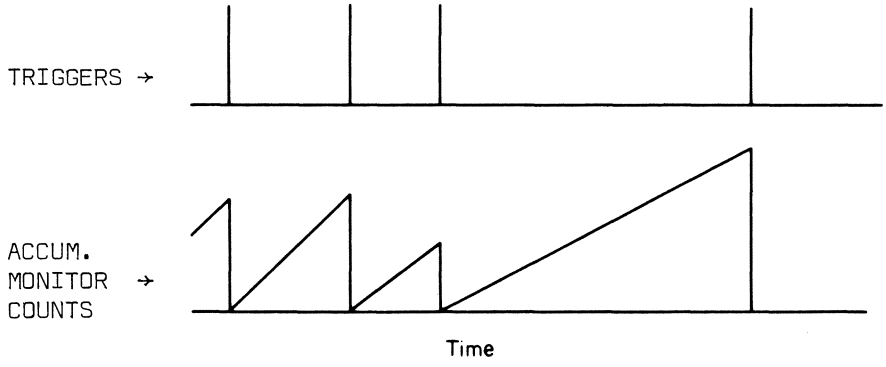

Now there are three kinds of "events":

a) Triggers + reconstructable tracks. These events are binned by momentum and angle; the content of a bin is related to the cross-section by

$$\frac{d^2\sigma}{dpd\Omega}\,\Delta p\Delta\,\cos\theta = \frac{F(p,\theta)K}{\sum R_M}\,\frac{dN(p,\theta)}{\Delta p\Delta\,\cos\theta}\,\Delta p\Delta\,\cos\theta$$

where $F(p,\theta)$ in the acceptance (see below)

b) Triggers + non-reconstructable tracks, e.g. a good event, but a failing spark chamber. In this case one rejects the event as well as the monitor counts accumulated since the previous event.

c) False triggers, e.g. a reconstructed track does not project through one of the trigger counters. In that case the trigger does not correspond to an event, one rejects the event but retains the monitor count accumulated since the previous trigger, i.e. the transfer was accidental and should not have taken place.

A fraction of the events are not due to beam-beam but to

beam-gas events. One way of correcting for this background is to run with one beam only and make a subtraction. If the background is low it is sufficient to examine the "diamond": the overlap region of the two beams. This distribution will have tails extending beyond the region of overlap, due to beam/gas events. Extrapolation of the tails into the diamond proper gives the correction. The beam/gas ratio can be as low as 4%.

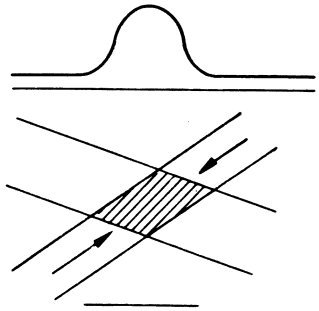

Systematic errors can arise e.g. from misalignment of the spark chambers. This is most easily checked by reconstructing tracks with the fields off and requiring the tracks to be straight lines. A further check is provided by the momentum which is measured in each magnet separately. Consistency requires that

$$\delta p = \frac{p_1 - p_2}{p_1 + p_2}$$

has a standard deviation (s.d.) which agrees with calculations based on measuring errors, multiple scattering etc. The momentum dependence of this standard deviation is sketched in the fig. Finally the acceptance function $F(p,\theta)$ is calculated by generating a number of events distributed over the diamond and tracking them through the apparatus, taking account of multiple scattering, absorption, decay, etc.

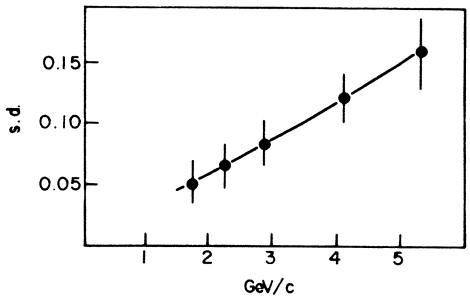

Results of single particle inclusive experiments are shown in figs 2 - 17:

a) To an accuracy of approximately ±15% there is a flat central plateau in y, in accordance with Mueller/Regge Pomeron exchange. See fig. 2, ref. 3.

b) Recent data[4] in which the accuracy is increased and on which more systematic checks (see above) have been made have revealed a slight dependence on rapidity at fixed s, and a dependence on s at fixed y. Neither PP exchange, nor RR exchange

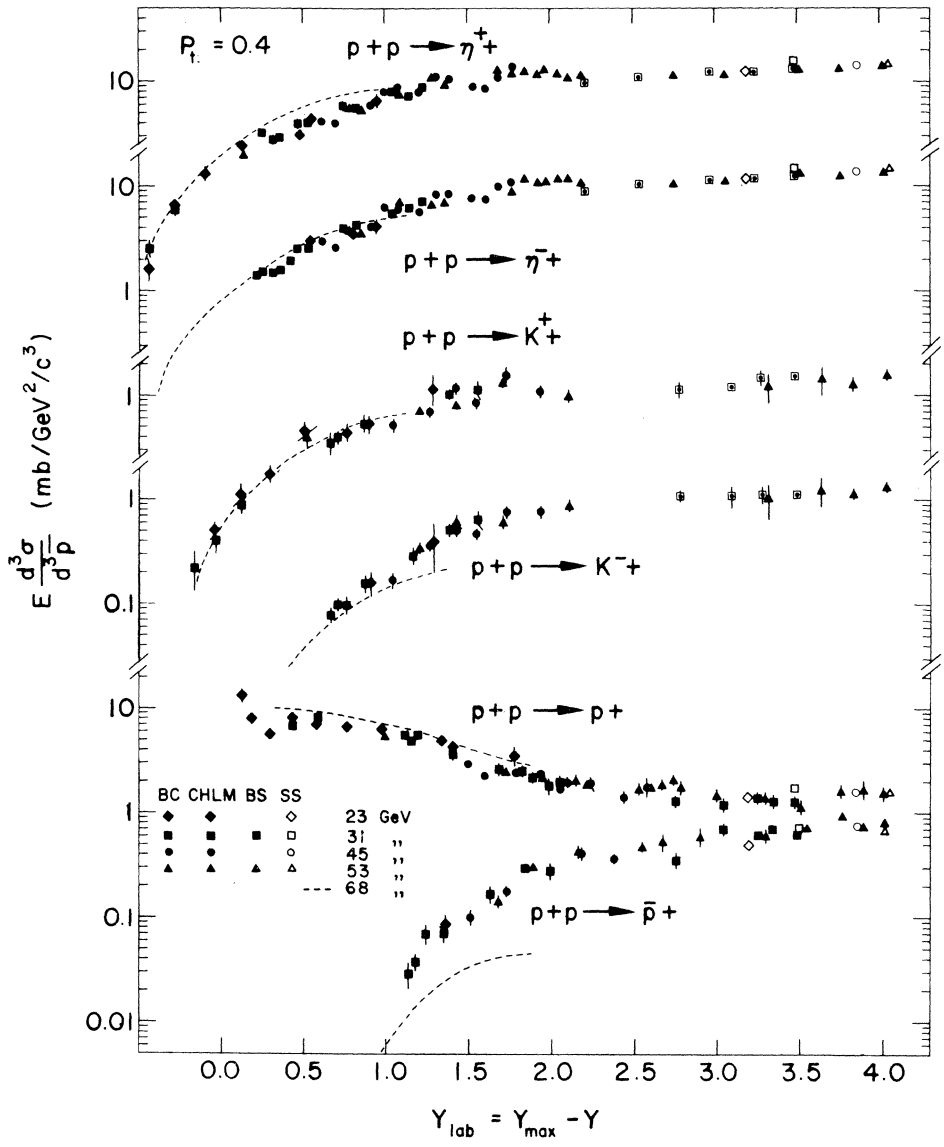

Fig. 2. Summary of single particle data at p_T = 0.4 GeV. From Ref. 3.

alone would result in a y-dependence, see eq. (III.4). The data suggest, but by no means prove, a dependence on y and s such that

$$E_c \frac{d^3\sigma}{dp^3} = f(y,p_T,s) = f(y_B - y, p_T) \sim A(p_T) \exp(-D(y_B-y))$$

with $D \simeq 0.15 \pm 0.03$. (y_B = rapidity of the beam). Such a dependence is characteristic for fragments produced with Pomeron exchange, see eq. (III.8) and thus suggests that fragments penetrate all the way down to y = 0 on the rapidity plot. See figs. 3, 4, 5, 6.

c) As to the approach to scaling, the data are consistent with various forms for the s-dependence. The form $s^{-1/4}$ is one possibility, but there are others, e.g. $s^{-1/2}$, see fig. 7.

d) Data on K^+ and p are consistent with no y-dependence, K^- is inconclusive and $\bar{p}$ data are definitely sloping. See figs. 8, 9, 10.

e) In the fragmentation region, π^- data at fixed $y_B - y = 0.36$ versus p_T show good evidence for scaling in the projectile frame, from s = 47 GeV^2 upwards and out to $p_T \simeq 1$ GeV/c, provided the low s data are represented in the variable $p_L/p_{Lmax}(o)$ or, better still, $p_L/p_{Lmax}(p_T)$ i.e. the one that takes the phase space boundary into account[5]. See fig. 11.

f) In the fragmentation region, K^- and $\bar{p}$ at $y_B - y = 0.36$ scale in the ISR energy range, but differ appreciably from data at low s, see fig. 12 and 13, ref. 6.

g) The approach to scaling in the fragmentation region is consistent with $s^{-1/2}$. This is shown in fig. 14 (ref. 6), where the K^- and $\bar{p}$ yields are expressed at ratios to the scaling (see fig. 11) π^- yields. Other forms of s-dependence are likewise possible, however.

h) For π^+ we have a behaviour similar to that of π^-. Fig. 15 shows π^+ data at fixed x = 0.38 versus p_T and fig. 16 data at fixed p_T = 0.8 versus x[7]. There is no discernable energy dependence as long as $p_T < 1$ GeV/c.

i) For protons, the approach to scaling at fixed (x,p_T) is illustrated in fig. 17, showing NAL[8] data versus s, compared with a curve $A + B/\sqrt{s}$. More about protons later.

In summary one might say that the absence of energy dependence in inclusive single particle spectra continues to hold to an impressive degree, although the so called central region is perhaps less central (at ISR energies) than was thought originally.

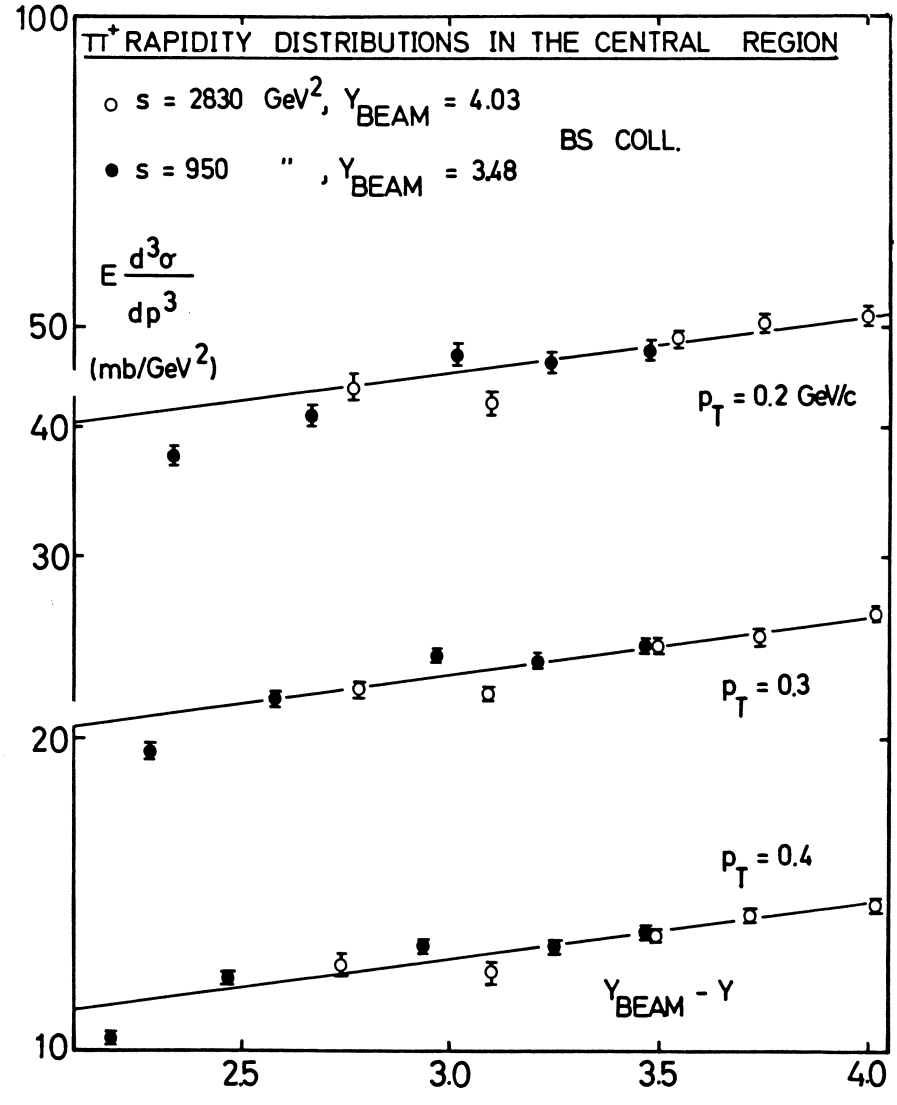

Fig. 3. Invariant diff. cross-sections for the production of π^+ versus y_{BEAM} - y at s = 2830 GeV^2 and at s = 950 GeV^2. Data at p_T = 0.2, 0.3, 0.4 GeV/c.

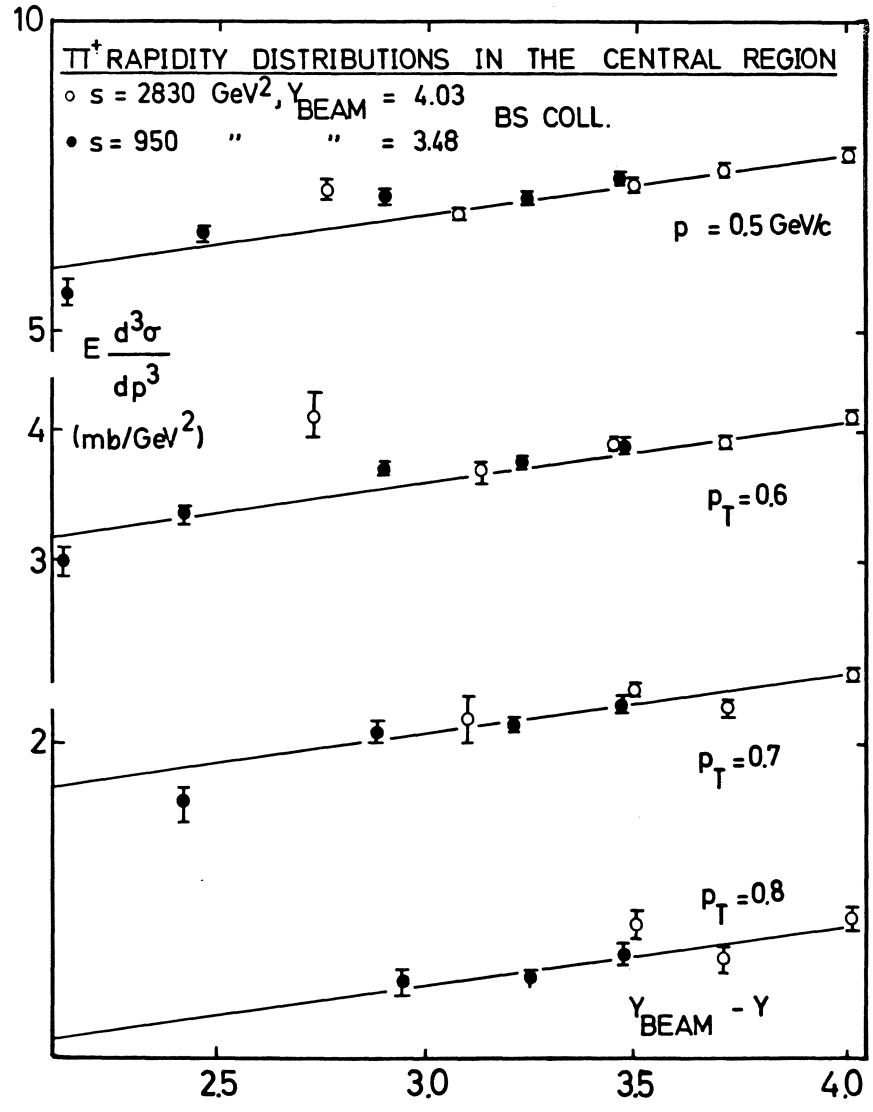

Fig. 4. Same as fig. 3 for p_T = 0.5, 0.6, 0.7, 0.8 GeV/c.

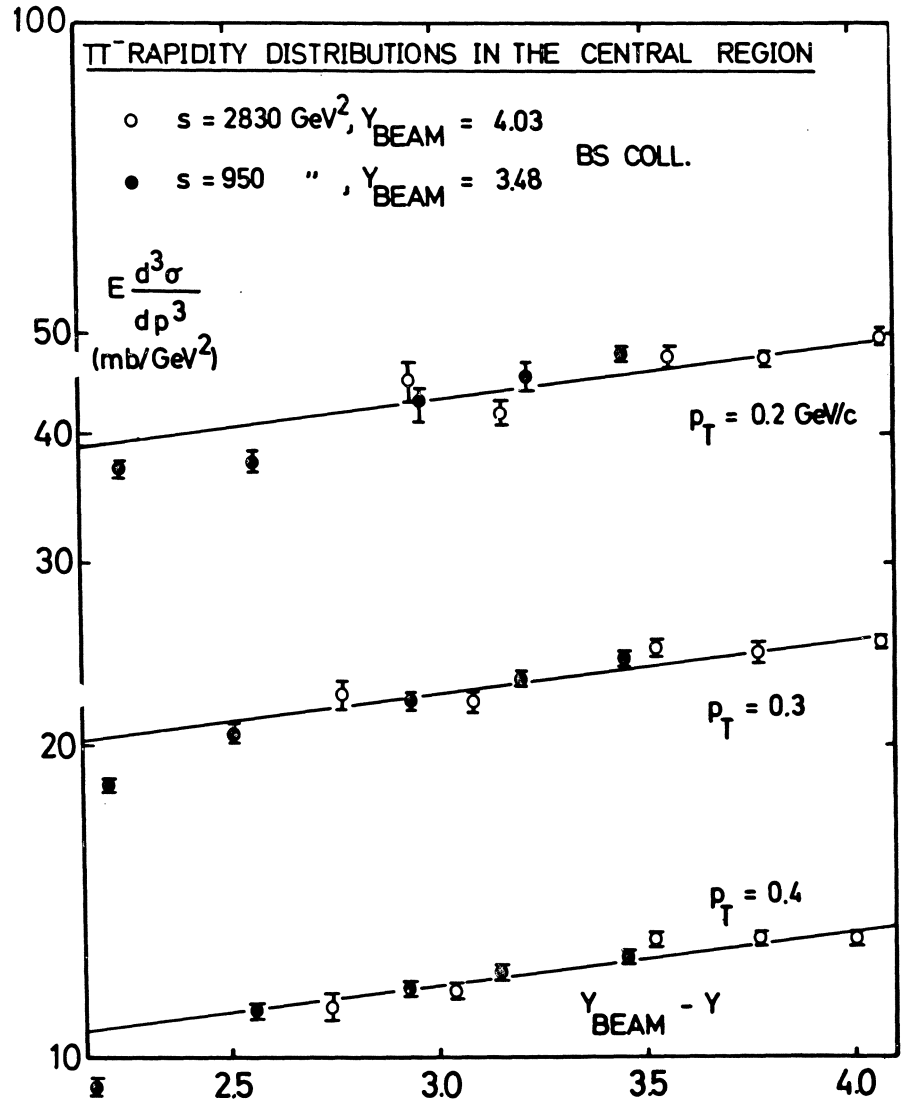

Fig. 5. Same as fig. 3, for π^-.

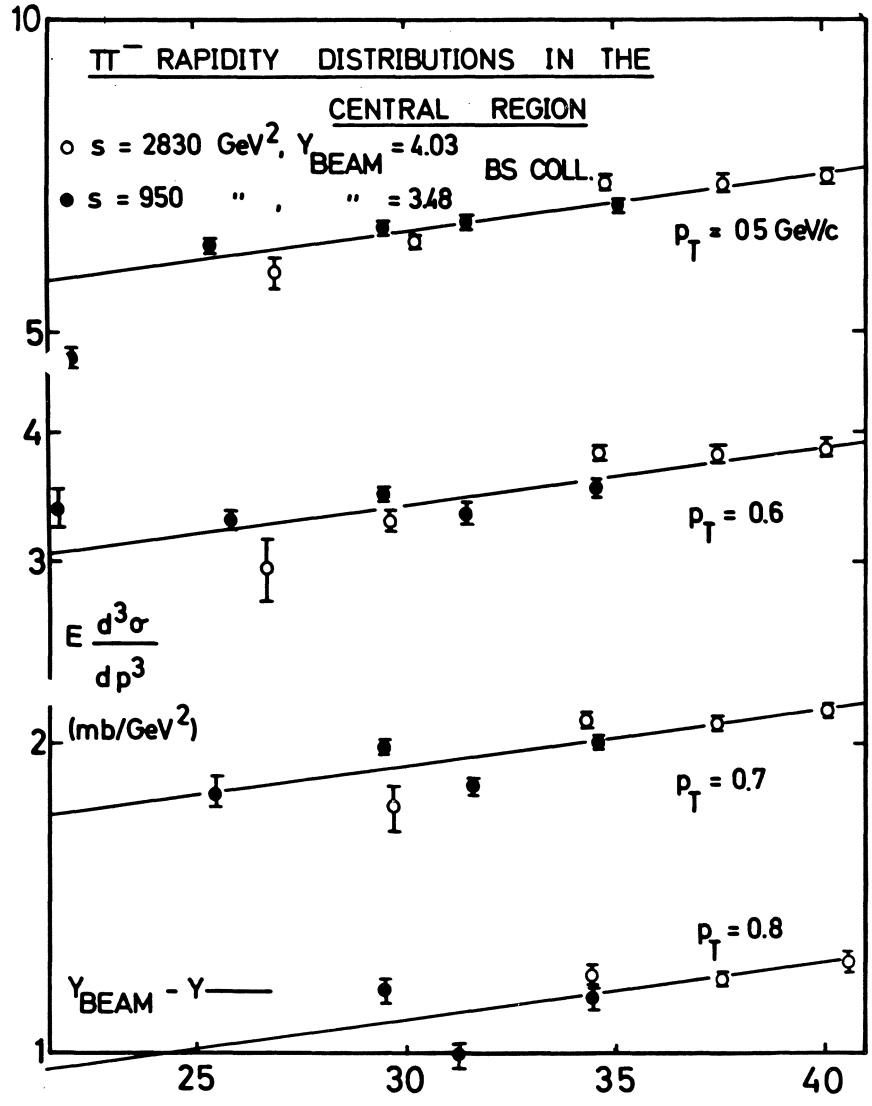

Fig. 6. Same as fig. 4, for π^-.

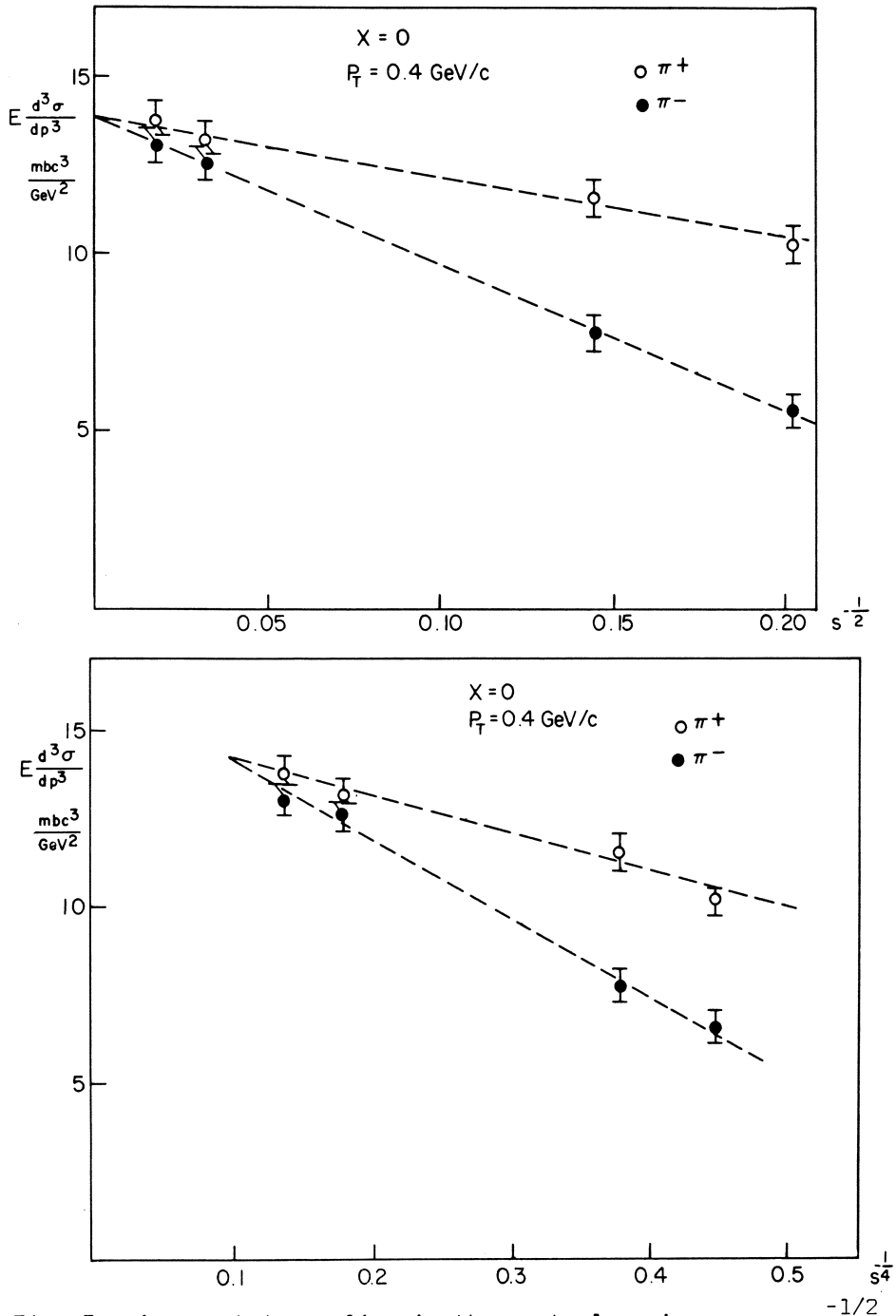

Fig. 7. Approach to scaling in the central region versus $s^{-1/2}$ (above) and $s^{-1/4}$ (below).

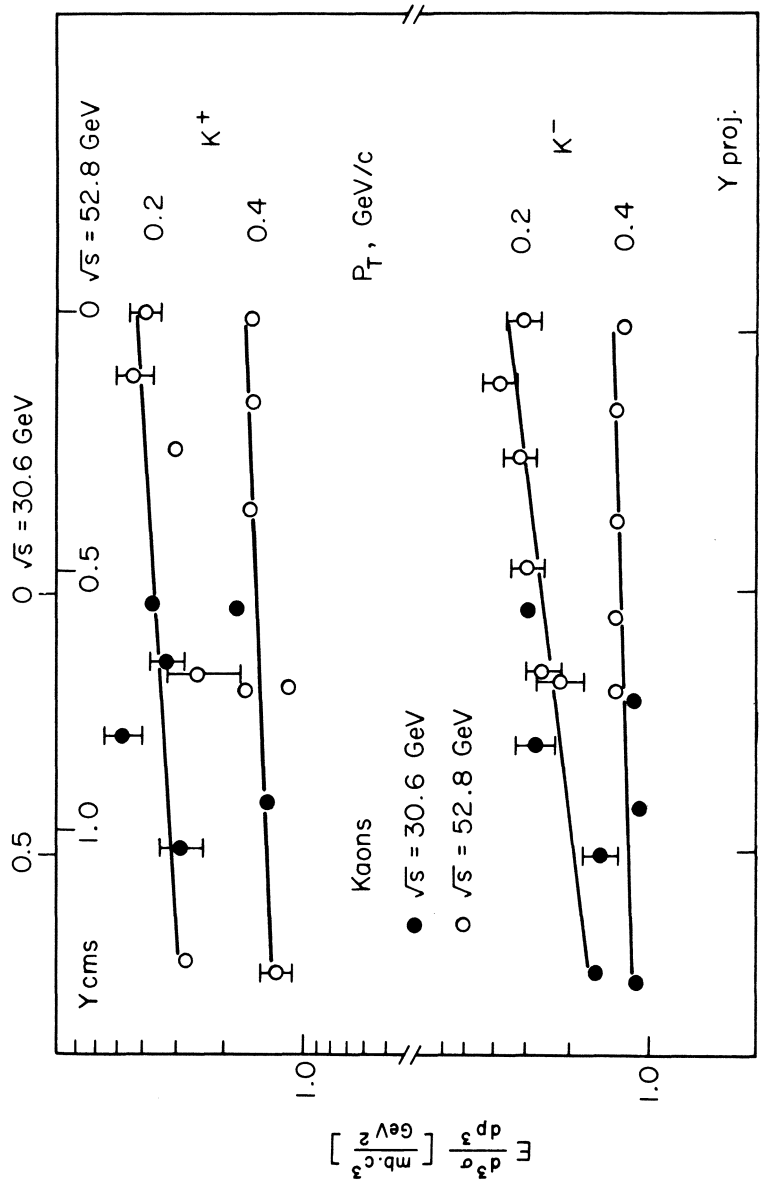

Fig. 8. Central region, K^+ and K^-.

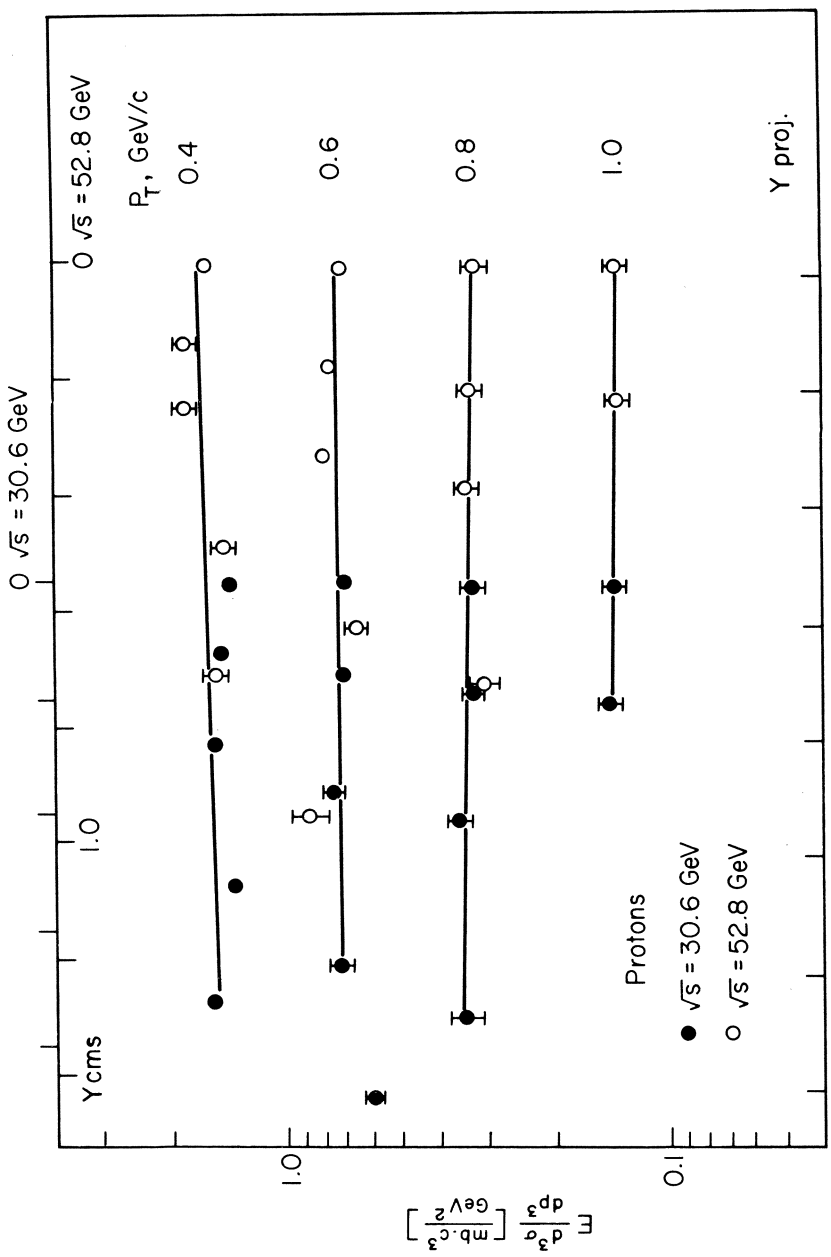

Fig. 9. Central region, protons.

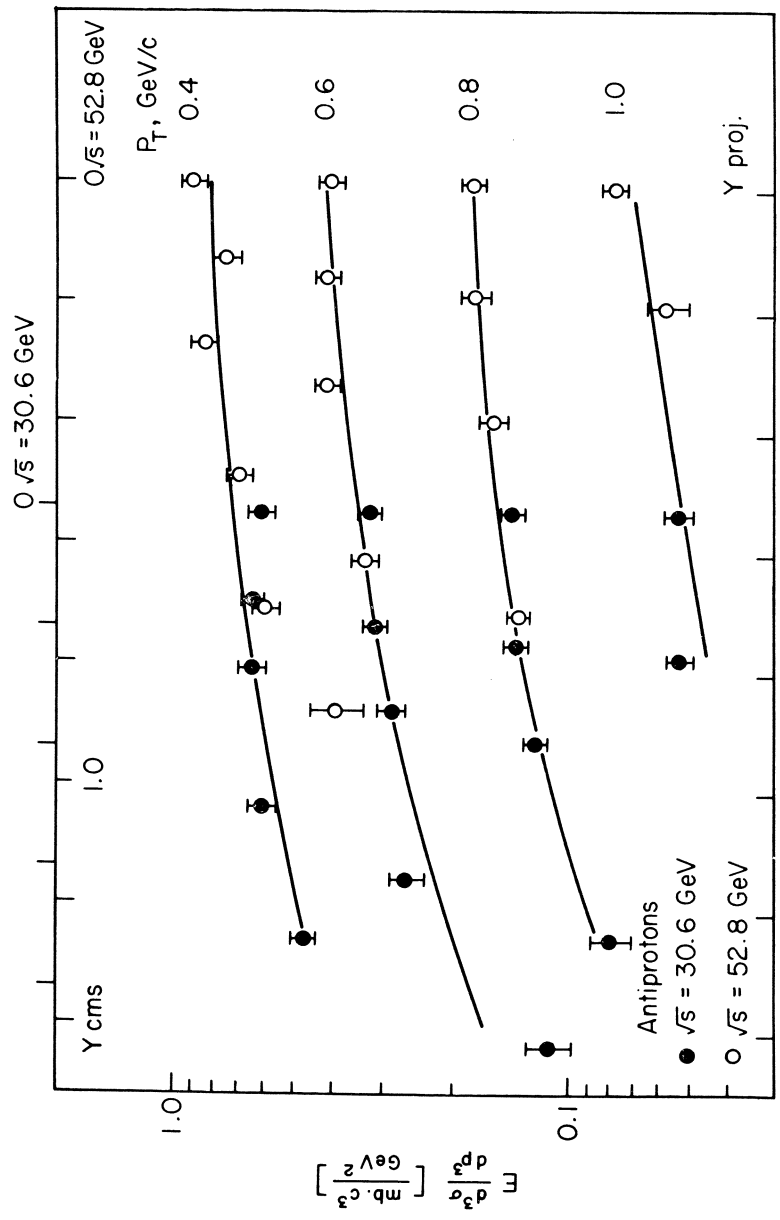

Fig. 10. Central region, antiprotons.

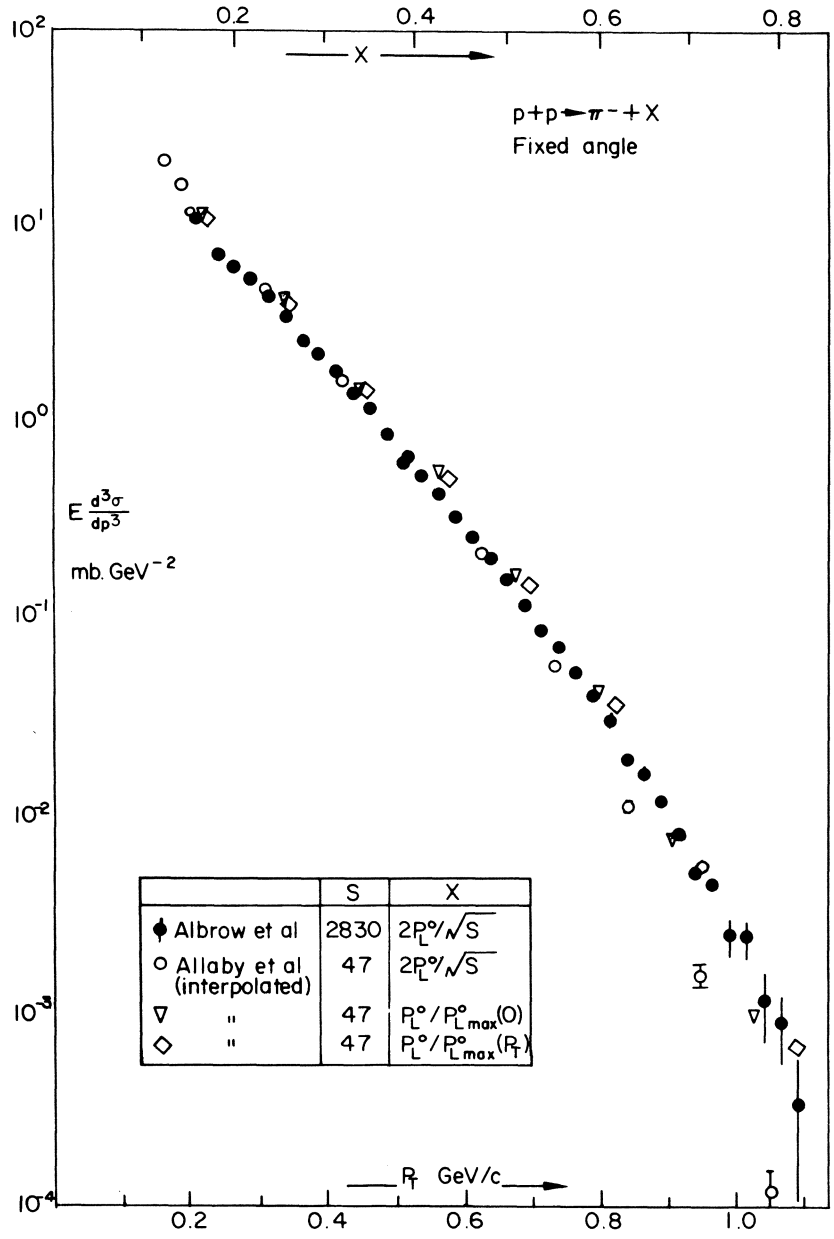

Fig. 11. Fragmentation region, data at $y_{BEAM} - y \simeq 0.36$, at $s = 47$ GeV^2 and $s = 2830$ GeV^2.

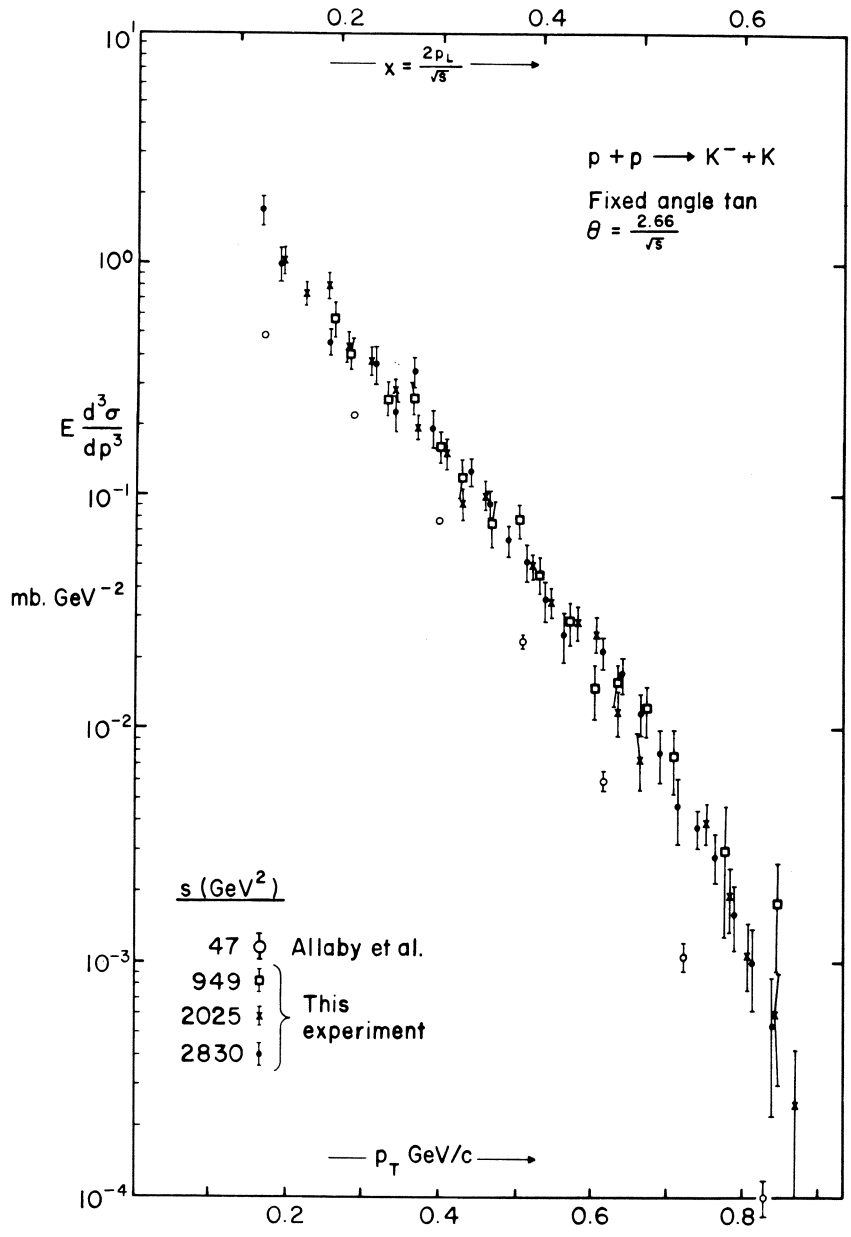

Fig. 12. Fragmentation region, data at $y_{BEAM} - y \simeq 0.36$ at various s for inclusive K^- production.

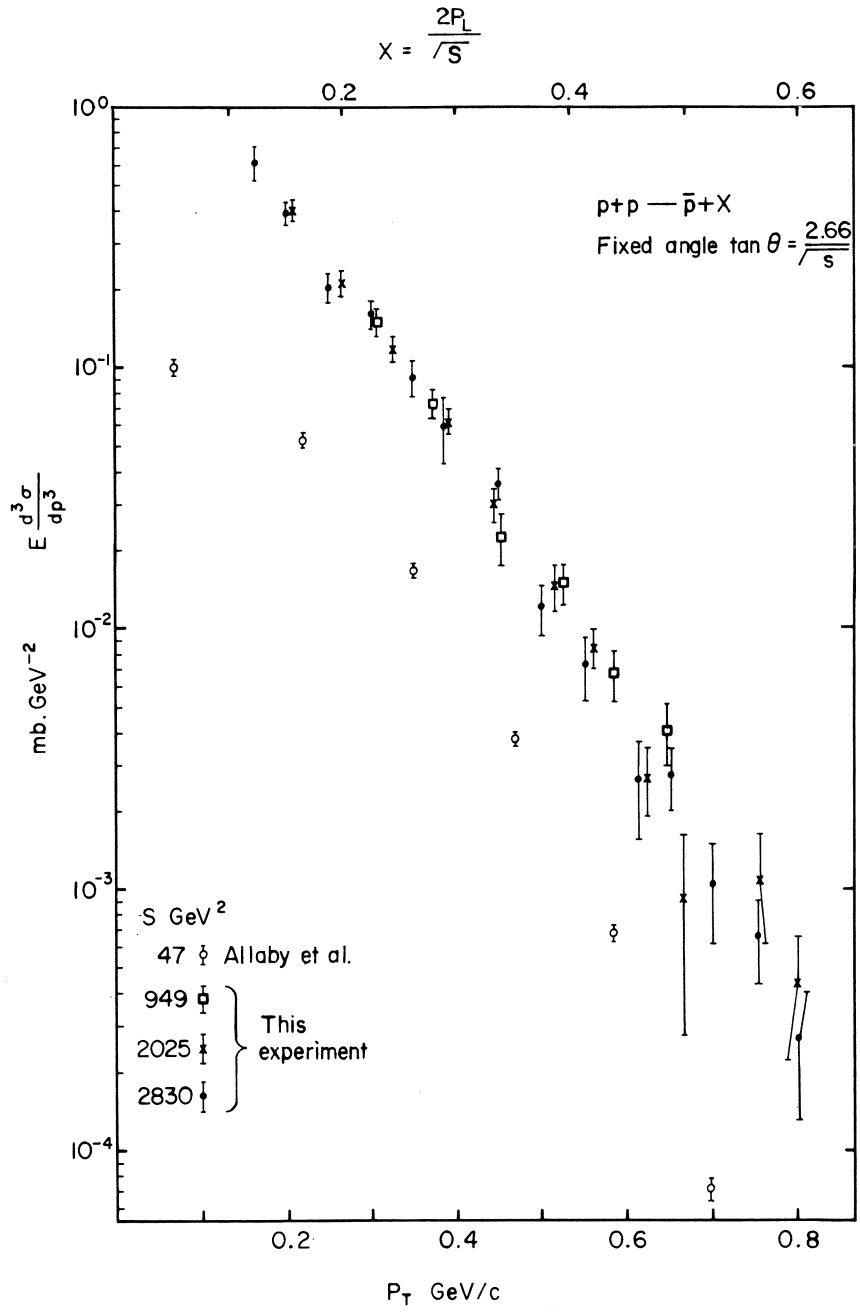

Fig. 13. Same as fig. 12, for $\bar{p}$.

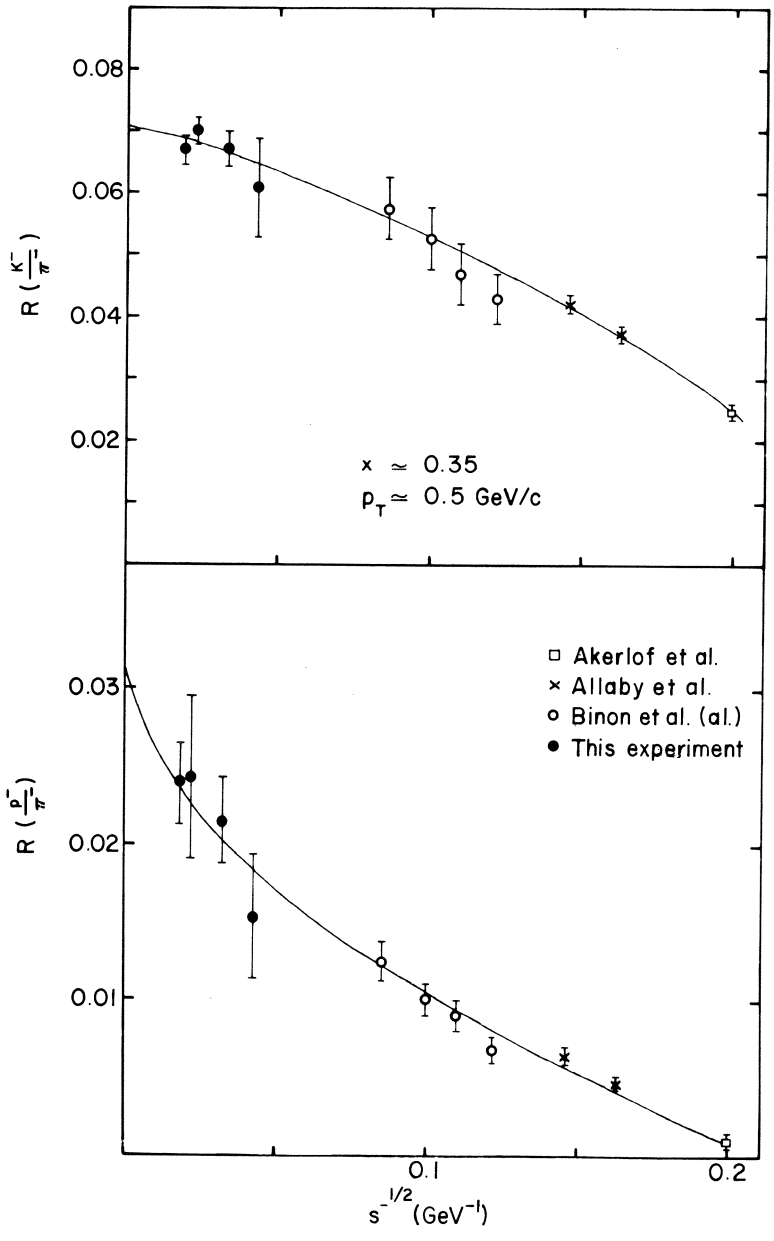

Fig. 14. s-dependence of K^-/π^- and $\bar{p}/\pi^-$ versus $s^{-1/2}$ at $p_T \simeq 0.5$ GeV/c showing the approach to scaling for K^- and $\bar{p}$ fragments.

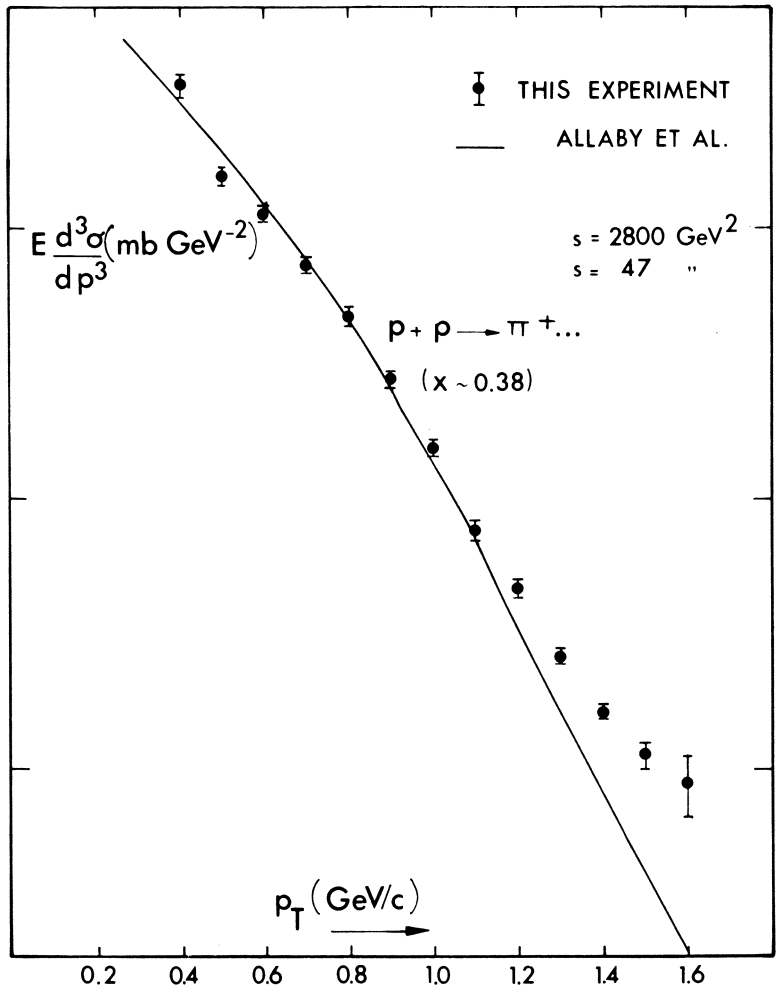

Fig. 15. p_T-dependence at s = 47 and 2800 GeV^2 for π^+ fragments, showing how fragments scale as long as $p_T \lesssim 1$ GeV/c (ref. 6).

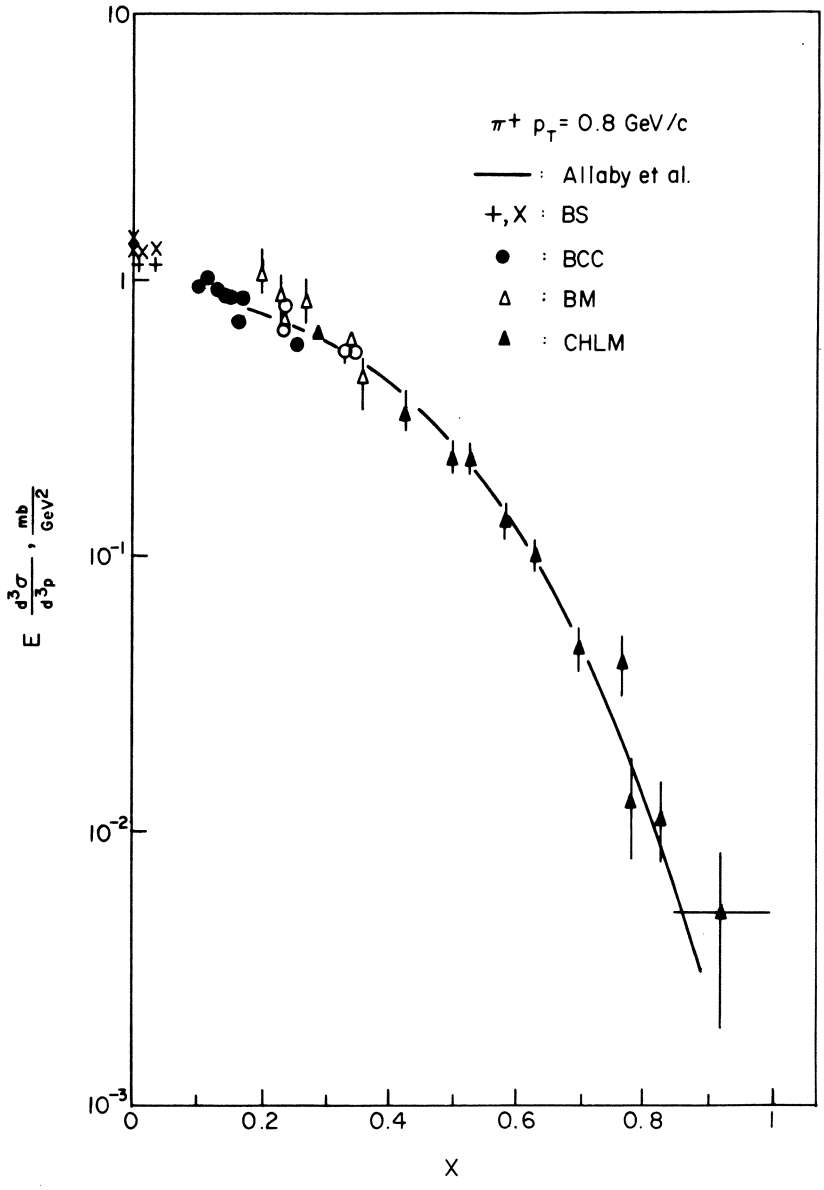

Fig. 16. x-dependence at p_T = 0.8 GeV/c and various 550 < s < < 2800 GeV^2, showing how fragments scale at all measured values of x.

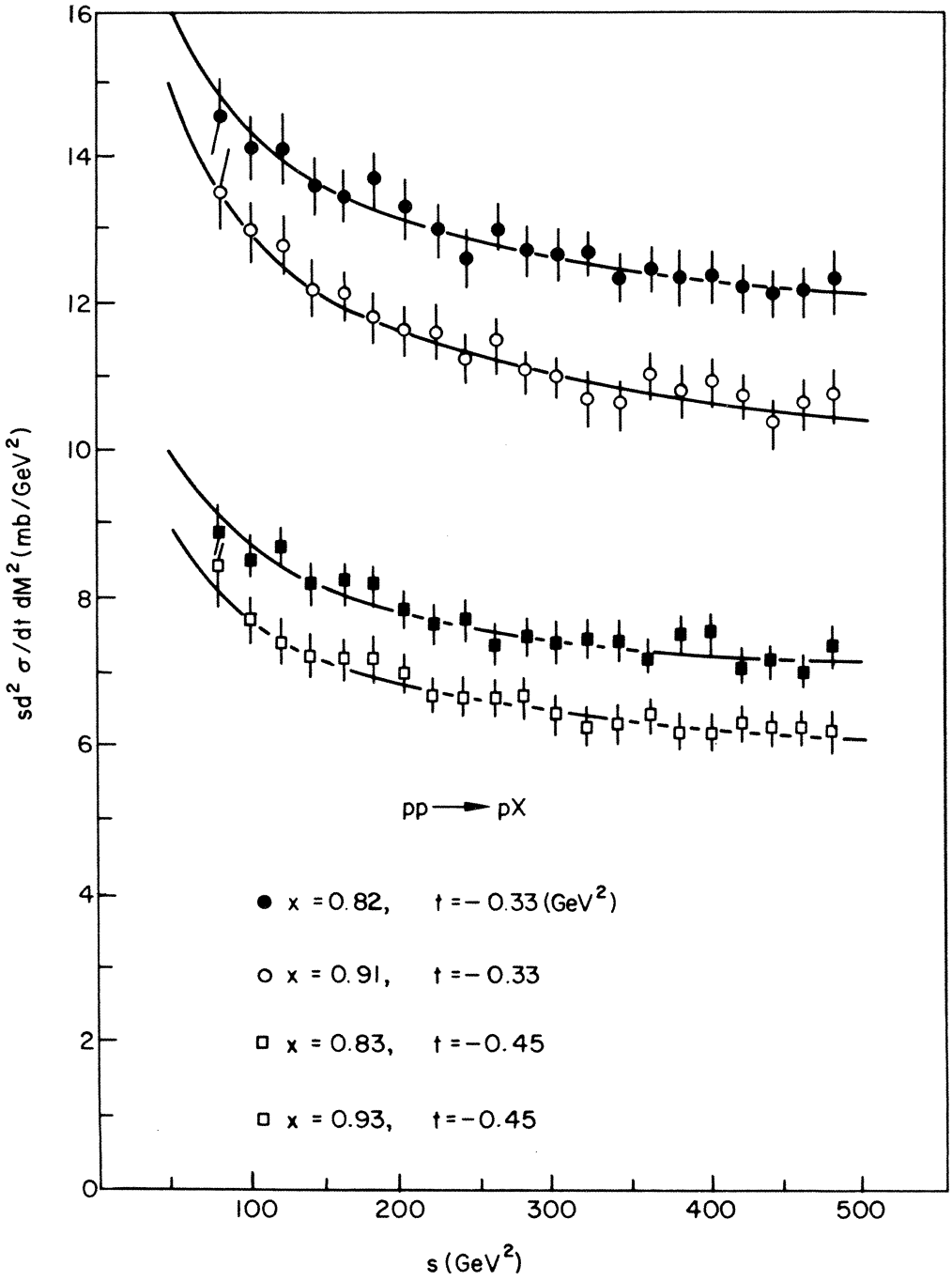

Fig. 17. NAL-data (ref. 8) on protons versus s at fixed x and t showing how scaling is approached "from above" for proton fragments.

SECTION III

REFERENCES

1) See e.g. K. Gottfried, Lectures Academic Training Program, CERN/TH 1615, for a much more detailed discussion.

2) British-Scandinavian collaboration, B. Alper et al., preprint.

3) M. Antimucci et al., Lettere al Nuovo Cimento 6, 121, 1973.

4) B. Alper et al., submitted to Phys. Letters.

5) A. Diddens, Lectures IVth Seminar on Theoretical Physics, GIFT, Barcelona, April 1973.

6) M.G. Albrow et al., Nucl. Phys. B56, 333, 1973.

7) E. Lillethun, Lectures at the XIII Cracow School of Theoretical Physics, Zacopane, June 1973.

8) F. Sannes et al., Phys. Rev. Letters 30, 766, 1973.

IV. SUMMARY OF LOW ENERGY MISSING MASS DATA

IV.1 History

Missing mass experiments in proton-proton collisions on stationary target have been performed since 1960. In summarizing the results we follow here ref. 1. A (hopefully complete) list of references follows below.

BRIEF SUMMARY OF LOW ENERGY ($s < 50\ GeV^2$) MISSING MASS EXPERIMENTS

CHADWICK	BNL	1960	PRL 4, 611	Δ(1236),N(1520)
COCCONI	CERN	1961	PRL 7, 450	N(1688),N(1470)?
CHADWICK	BNL	1962	PR 128,1823	
DIDDENS	CERN	1962	PRL 9, 111	
COCCONI	CERN	1964	PL 8, 134	
BELLETTINI	CERN	1965	PL 18, 167	CONFIRMS N(1470)21<s<50 SMALL t < 0.01
ANDERSON	BNL	1966	PRL 16,855	N(2190) 13<s<58 t<1
FOLEY	BNL	1967	PRL 19,397	t < 0.2
ANKENBRANDT	BERKELEY	1968	PR 170,1223	8 < s < 15
ALLABY	CERN	1968	PL 28B,229	s = 38 t < 6
BLAIR	NIMROD	1969	N.C.63A,529	7.3 < s < 17 SMALL t
EDELSTEIN	BNL	1972	PR D5,1073	13 < s < 58
ALLABY	CERN	1972	Nucl.Phys.B	s = 47 t < 6
.....				
ALBROW	ISR	1973	Nucl.Phys.B51,388	s = 2030
ALBROW	ISR	1973	Nucl.Phys.B54,6	s = 960
BROMBERG	NAL	1973	Preprint	s = 190
DAO	NAL	1973	PRL 30, 34	s = 560
SANNES	NAL	1973	PRL 30, 766	80 < s < 480
BARISH	NAL	1973	APS APRIL 1973	s = 380
CHILDRESS	NAL	1973	PRL (SUBMITTED)	s = 380

Note the jump in s, made with the start-up of NAL and ISR (dotted line).

IV.2 Typical Apparatus

Missing mass experiments require a precision measurement of momentum and angle of the produced proton in

$$p + p \rightarrow p + X$$

The apparatus of Allaby et al. with which the latest low s data have been obtained is described in ref. 1. We shall list the salient features of this equipment below. The lay out is shown in

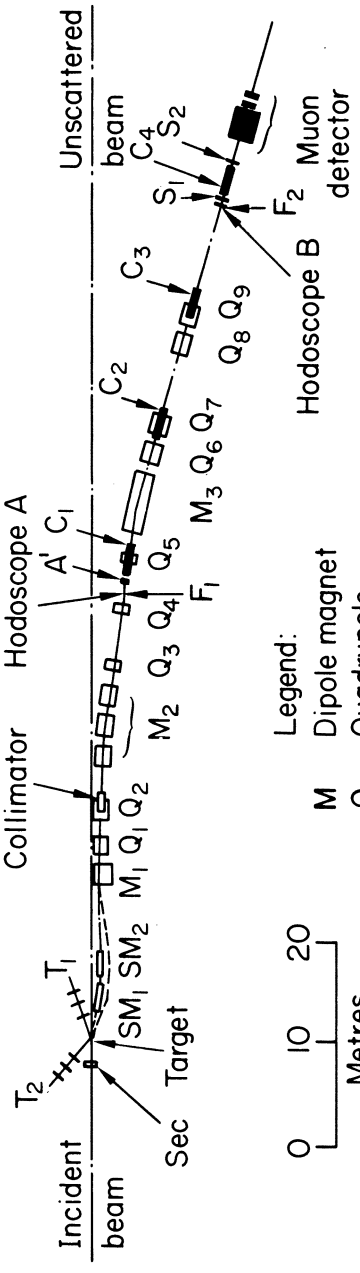

Fig. 1. Spectrometer for the measurement of pp → pX on a stationary target at energies < 25 GeV.

fig. 1.

- SLOW EXTRACTED BEAM; 350 msec SPILL; 10^{12} p/BURST.
- LIQ. H_2 TARGET; SPOTSIZE ~4 mm Ø, ±0.5 MRAD, 10-20 cm.
- SPECTROMETER WITH AXIS FIXED AT θ = 37 MRAD.
- CALIBRATION OF INC. FLUX BY Na^{24} ACTIVITY INDUCED IN AL-FOIL BY BEAM.
- Φ_1,Φ_2 IMAGE TARGET TO F1.
  M_2 BENDS 120 MRAD. AT F1 DISPERSION $\overset{\wedge}{=}$ 1.6 cm FOR $\frac{\Delta p}{p}$ = 1.0%.
  Φ_6,Φ_7 MAKE BEAM PARALLEL FOR USE OF C.M_3 BENDS 120 MRAD.
  Φ_3,Φ_4,Φ_5 PROJECT CENTRAL PLANE OF M_2 ONTO CENTRAL PLANE OF M_3
  F_2 IS FINAL FOCUS, MADE BY Φ_8,Φ_9.
- ACCEPTANCE HOR. ±1.5 MRAD, VERT. ±4.5 MRAD.
  $\Delta p/p$ = ±1.5%
  DISPL. IN TARGET ±1.5 cm.
  ACC. DEFINED BY COLLIMATOR OF Ø = 8 cm; $\Delta\Omega = 1.3 \times 10^{-5}$ sr.
- SM_1SM_2, M_1 for $\theta \neq 37$ MRAD.
  ANGULAR RANGE 12 → 152 MRAD. CONSEQUENCE $p(\theta - 37)$ = const.

- MAGNET CALIBRATION TO $\Delta p/p$ = ±0.1%
- OVERALL LENGTH 86 m.

IV.3 Features of the Results

Fig. 2 shows the data obtained with the apparatus of fig. 1: the diff. cross-section $d^2\sigma/dtdM^2$ versus M^2 at fixed lab angle (ref. 1). Note that the horizontal scale starts above the location of the elastic peak. Since the angle for each curve is fixed, $|t|$, the 4-momentum transfer, changes over the mass range covered by each curve. A valley is seen below the elastic peak, followed by a gradual rise with several bumps superimposed.

Fig. 3 shows the structure in more detail. There is evidence for several bumps. Fitting the data with a polynomial describing the continuum (dash-dotted line in fig. 3) and Breit-Wigner formulae to describe the resonances (dotted line in fig. 3) the following results were obtained:

	SLOPE (GeV^{-2})	$d\sigma/dt(t=0)$ mb/GeV^2	σ (mb)
Δ(1236)	6.4 ± 0.8	0.18 ± 0.05	0.057 ± 0.017
N(1400)	24.2 ± 2.5	11.6 ± 4.2	0.96 ± 0.35
N(1520)	4.84 ± 0.24	0.91 ± 0.19	0.37 ± 0.07
N(1688)	5.12 ± 0.08	2.35 ± 0.36	0.92 ± 0.14
N(2190)	3.01 ± 0.17	0.16 ± 0.05	0.108 ± 0.033

Some features of these data are
- At $|t| \simeq 0.1$, the N(1400), N(1520), N(1688) are excited with

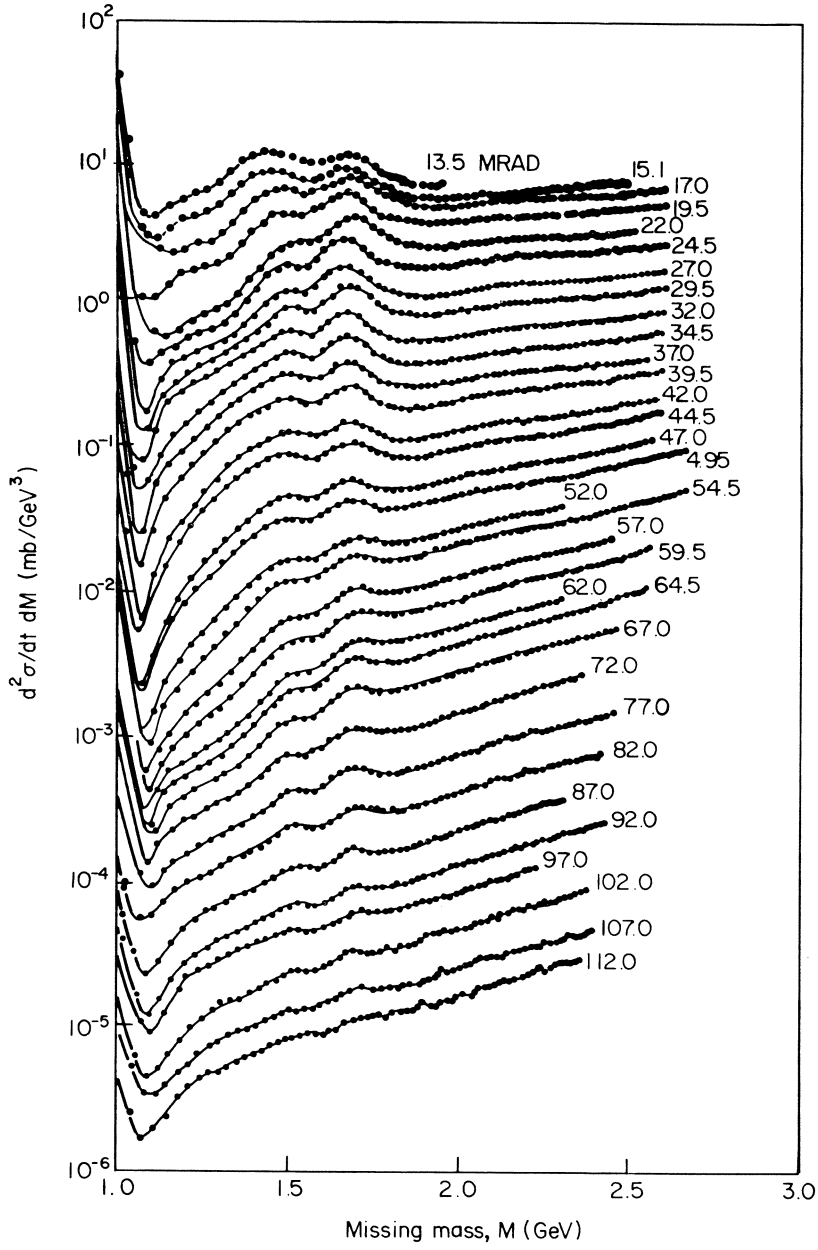

Fig. 2. Missing mass spectra taken at 24 GeV/c incident momentum. The elastic peaks are off the scale to the left.

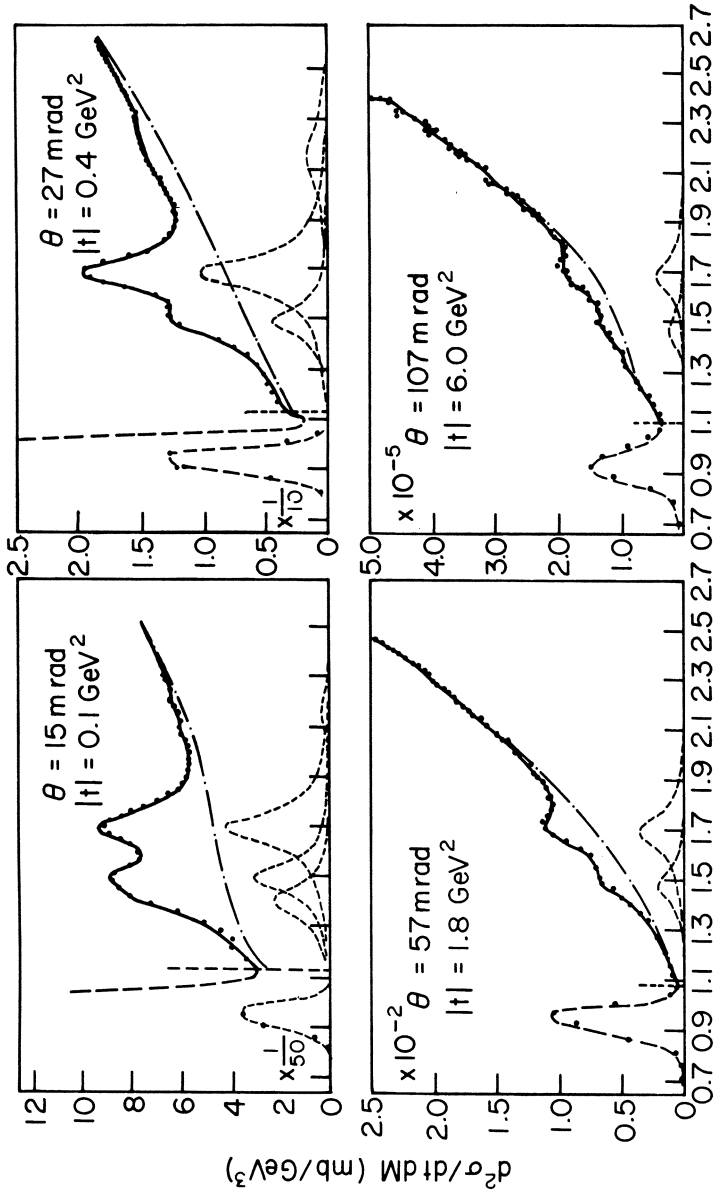

Fig. 3. pp → pX at 24 GeV/c, details. The lines are fits to the background + resonances.

comparable cross-section. The N(2190) and Δ(1236) are excited with 1/10 the strength.
- The isolation of the Δ(1236) is complicated by the fact that it is located in the valley between the elastic peak and the rising inelastic continuum. Its cross-section decreases strongly with energy, $\sim s^{-2.5}$. Its dependence on t and s is shown in fig. 4.
- The N(1400) has a steep dependence on t and possibly an (elastic-like) diffraction minimum + secondary maximum, see fig. 5.
- The N(1520) and N(1688) have a t-dependence similar to that of elastic scattering, at $t > 2$ GeV^2. No dip is seen in the N(1500) and N(1688) t-distributions, neither at $t \simeq 1.4$ GeV^2 nor anywhere else. See fig. 6.
- The N(1520) and N(1688) are weakly dependent on s at small t, strongly at large t. See figs. 7,8.
- For completness the t-distr. of the N(2190) is shown in fig. 9.
- The integrated cross-sections for N(1450), N(1520), N(1688), N(2190) are independent of s.
- Comparing the production of N(1688) by pions and protons one finds factorization:

$$\frac{\pi p \to \pi\, N(1688)}{\pi p \to \pi p} = \frac{pp \to pN(1688)}{pp \to pp}$$

The main conclusions to be drawn from low s missing mass data are thus:

1) Dominance of minimal exchange, pointing to diffraction dissociation.
   $\sigma(I = 1/2)$ is constant with increasing s (P-exchange)
   $\sigma(I = 3/2)$ falls with increasing s (π → exchange)
2) The data support the Morrison/Gribov rule stating that for diffractively produced states the exchange of spin and parity are limited by the constraint $\Delta P = (-1)^{\Delta J}$:

N(1520)	N(1688)	N(2190)
$J^P = 3/2^-$	$5/2^+$	$7/2^-$

3) There seem to be important "multiple scattering" effects at large t.
4) The N(1688) cross-section in πp and pp is consistent with a factorizable Pomeron.

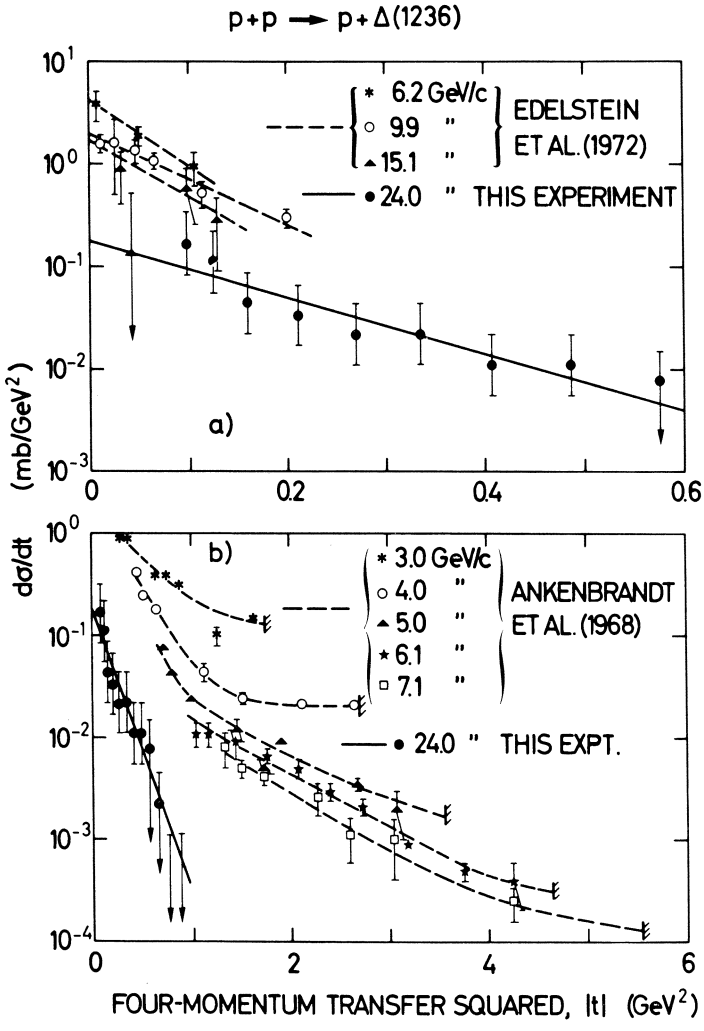

Fig. 4. Differential cross-section for the production of Δ(1236) at 24 GeV/c. Lower energy data are also shown.

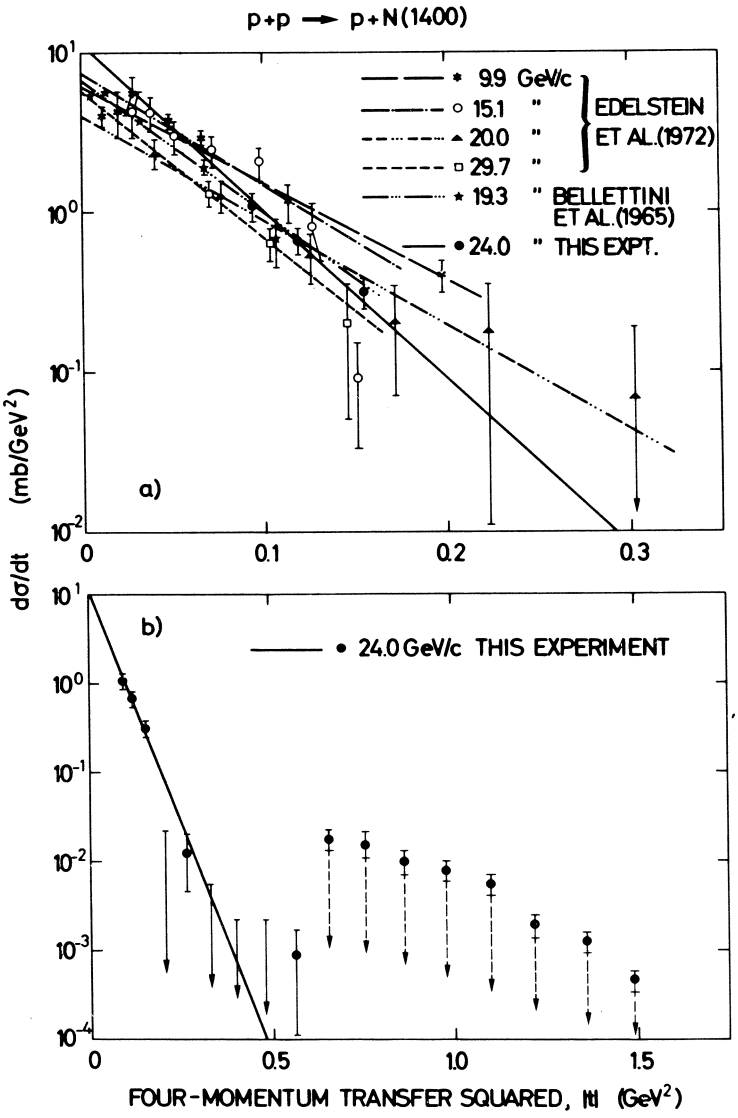

Fig. 5. Diff. cross-section for the production of N(1400). The broken lines represent the uncertainty, additional to the statistical errors, due to the fitting procedure.

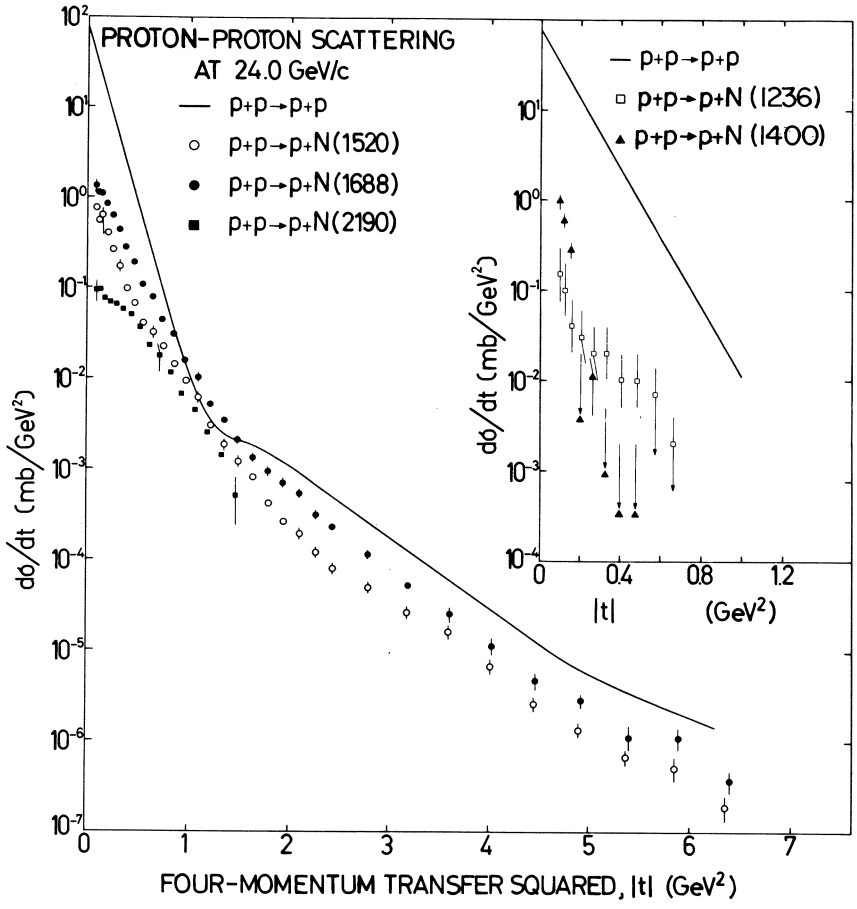

Fig. 6. Diff. cross-section for the production of N(1520) and N(1688) at 24 GeV/c.

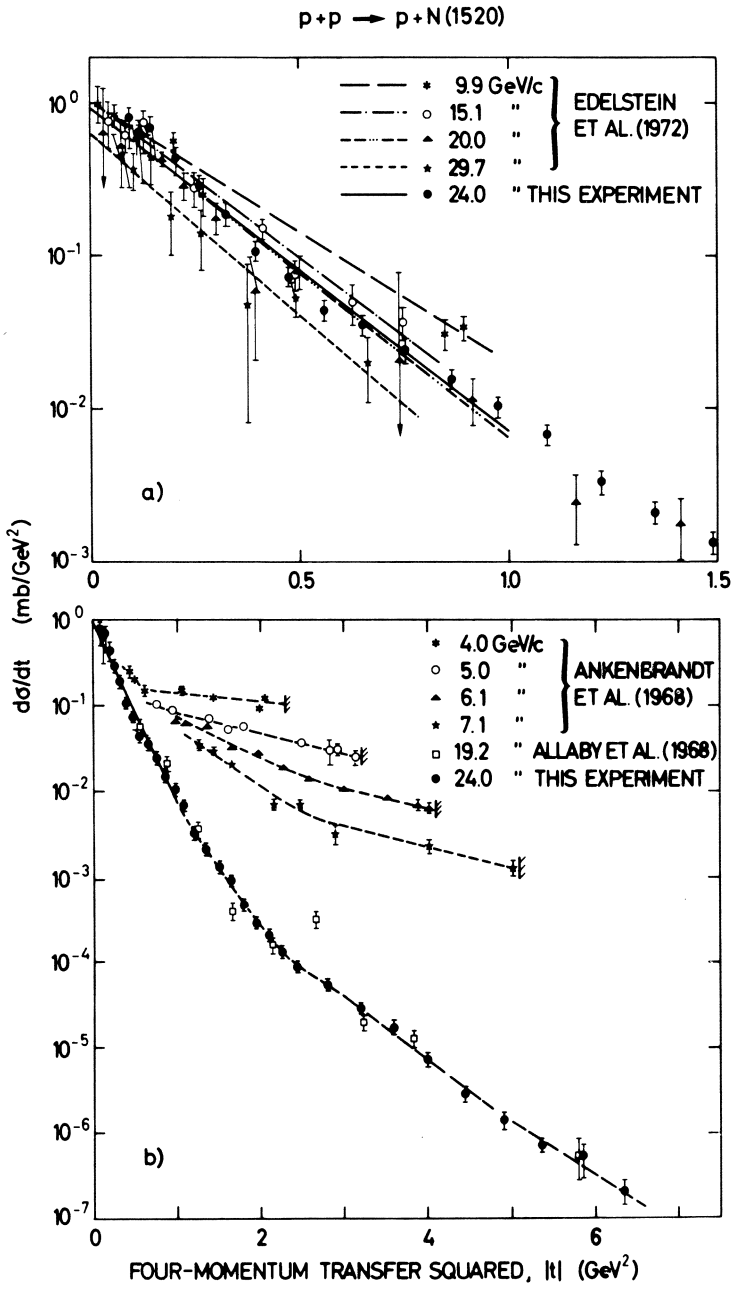

Fig. 7. N(1520) production at various s.

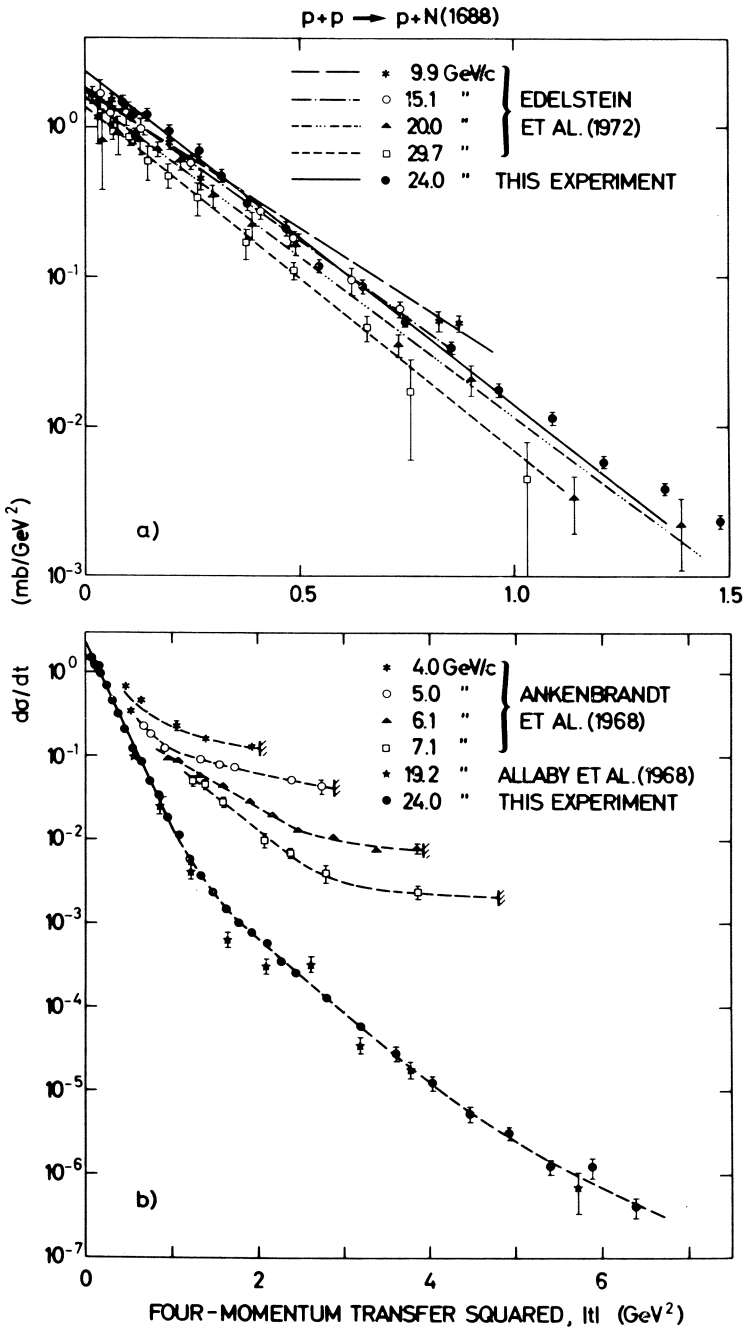

Fig. 8. N(1688) production at various s.

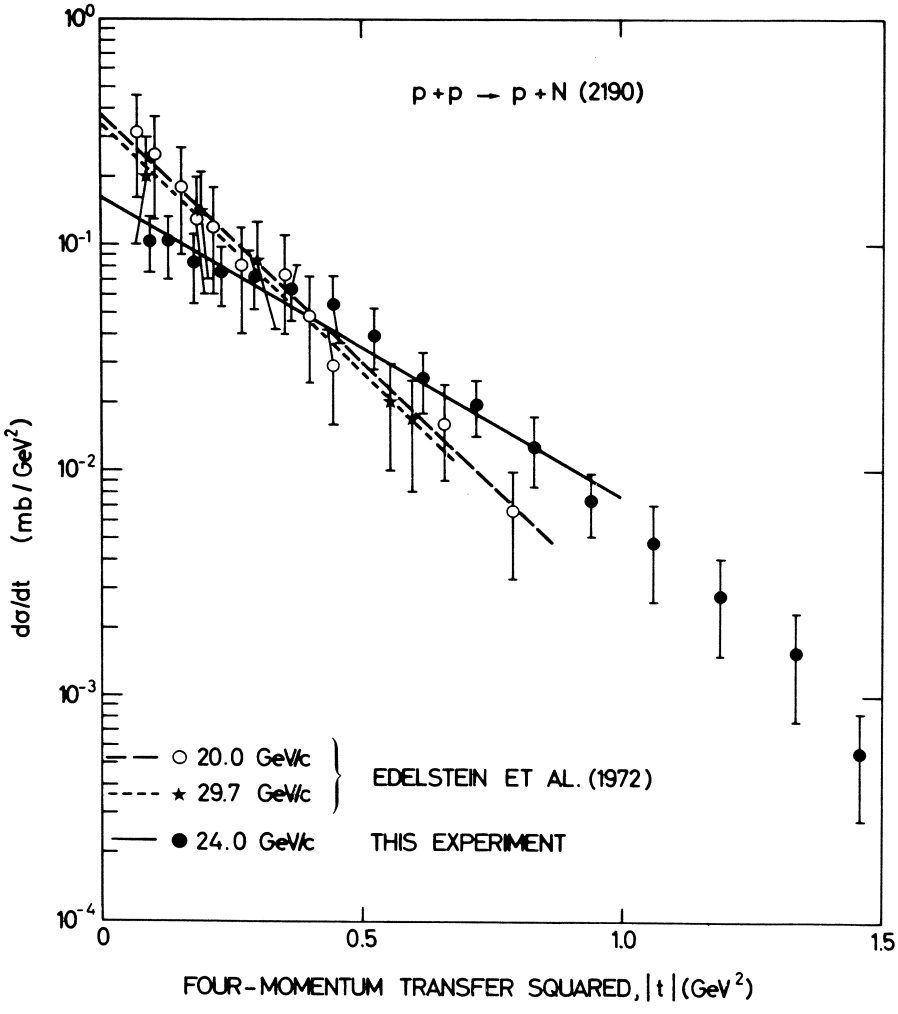

Fig. 9. N(2190) production.

SECTION IV

REFERENCES

1) Allaby et al., Nucl. Phys., B52, 316 (1973).

V. HIGH ENERGY ($s > 100$ GeV^2) MISSING MASS EXPERIMENTS

This section, and the next, deals with missing mass experiments at NAL and ISR. First, some kinematical relations relevant to MM experiments with stationary targets and with colliding beams will be listed. This is followed by a discussion of three experiments and of some results. More complete summaries of results can be found in various recent review articles[1].

V.I Kinematics

Consider $p + p \to p + X$ (m = proton mass) (V.1)

$1 + 2 \to 3 + 4$

where 3 is the particle observed and 4 stands for all the other particles combined. Then ($\underline{p} = p, iE/c$)

$$-s = (p_1 + p_2)^2 \qquad -t = (p_1 - p_3)^2$$

$$-M^2 = (p_1 + p_2 - p_3)^2 = (p_1 + p_2)^2 - m^2 - 2p_3(p_1 + p_2) \tag{V.2}$$

In the c.m.:

$$\vec{p}_1 + \vec{p}_2 = 0$$

hence

$$M^2 = s + m^2 - 2\sqrt{s}\,E_3^* \qquad (E_3^* = \text{energy of 3 in c.m. system})$$

and

$$M^2 = s + m^2 - 2\sqrt{s}\sqrt{\frac{x^2 s}{4} + p_T^2 + m^2} \simeq s(1-x) \tag{V.3}$$

where $x \equiv 2p_{3L}^*/\sqrt{s}$. The maximum value of x is attained when $M^2 = m^2$:

$$x_{max} = \left[1 - \frac{4(p_T^2 + m^2)}{s}\right]^{1/2} \tag{V.4}$$

Note that x_{max} depends on s. For example, for $p_{LAB} = 100$ GeV/c and $p_T = 1$ GeV/c $x_{max} = 0.98$.

The dependence of M^2 on the momenta involved (p_1, p_2, p_3) is obtained from:

$$M^2 = (\underline{p_1} + \underline{p_2} - \underline{p_3})^2 =$$

$$= 3m^2 - 2\vec{p}_1\vec{p}_2 + 2E_1E_2 + 2\vec{p}_1\vec{p}_3 - 2E_1E_3 + 2\vec{p}_2\vec{p}_3 - 2E_2E_3 \qquad (V.5)$$

Putting $\delta p_1/p_1 \simeq \delta E_1/E_1 = \varepsilon$ one gets by differentiating

$$\delta M^2 = \varepsilon\,(-2\vec{p}_1\vec{p}_2 + 2E_1E_2 + 2\vec{p}_1\vec{p}_3 - 2E_1E_3)$$

$$= \varepsilon\,(M^2 - 3m^2 - 2\vec{p}_2\vec{p}_3 + 2E_2E_3) \qquad (V.6)$$

At this point we note that in missing mass experiments the momentum of 3 is close to its maximum value and the angle is small. We take 3 to emerge near to the direction of 1;

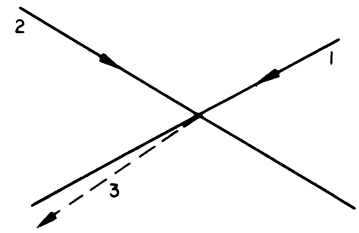

Then (V.6) becomes:

$$\delta M^2 \simeq \varepsilon\,(M^2 - 3m^2 + 4E_2E_3)$$

with

$$s = (\underline{p_1} + \underline{p_2})^2 \simeq 4E_1E_2 \simeq 4E_2E_3$$

we then have

$$\delta M^2 \simeq \varepsilon\,(M^2 - 3m^2 + s) \simeq \varepsilon\, s$$

or

$$\delta M^2_{p_1} = s\,\frac{\Delta p_1}{p_1} \qquad (V.7)$$

For example, for $s = 200$ GeV^2 and $\Delta p/p = 1\%$ $\delta M^2 = 2$ GeV^2.

The dependence in M^2 on the uncertainty in p_2 can be calculated by putting $\delta p_L/p_L \simeq \delta E_2/E_2 = \varepsilon$ and differentiating (V.5) with

respect to p_2:

$$\delta M^2 \simeq \varepsilon \, (M^2 - 3m^2)$$

and thus

$$\delta M^2_{p_2} \simeq M^2 \frac{\Delta p_2}{p_2} \qquad (V.8)$$

Likewise, for the dependence of the resolution in M^2 on the accuracy with which the produced proton is measured we have

$$\delta M^2 = \varepsilon \, (M^2 - 3m^2 - s)$$

$$\delta M^2_{p_3} \simeq - s \frac{\Delta p_3}{p_3} \qquad (V.9)$$

Note that we work with invariants, hence for missing mass experiments on stationary target we have

$$\delta M^2_{p_1} = s \frac{\Delta p_1}{p_1} \qquad \delta M^2_{p_2} = 0 \qquad \delta M^2_{p_3} = -s \frac{\Delta p_3}{p_3} \qquad (V.10)$$

Hence in either case, colliding beams or stat. target, there is a strong dependence on the knowledge of the momentum of one of the incident protons, resp. the incident protons, and of the produced proton; there is little or no sensitivity to the momentum of the "target" proton.

Next, we consider the energy loss. For stationary targets we have from (V.5)

$$p_2 = 0 \qquad M^2 = (E_1 + m - E_3)^2 - (\vec{p}_1 - \vec{p}_3)^2$$

$$= t + m^2 + 2m \, (E_1 - E_3)$$

Hence for small t

$$\Delta E = E_1 - E_3 = \frac{M^2 - m^2}{2m} \qquad \text{STAT. TARGET} \qquad (V.11)$$

e.g. E_1 = 300 GeV M = 1.5 GeV ΔE = 730 MeV or 0.25%

For colliding beams we get

$$M^2 = ((E_1 - E_3) + E_2)^2 - ((\vec{p}_1 - \vec{p}_3) + \vec{p}_2)^2$$

$$\simeq t + m^2 + 4\,E_2(E_1 - E_3)$$

for small crossing angle and (as always) high momenta. Thus

$$\Delta E = E_1 - E_3 = \frac{M^2 - m^2}{2m}\,\frac{m}{2E_1} \qquad \text{COLL. BEAMS} \qquad \text{(V.12)}$$

e.g. 11/8/11.8 GeV M = 1.5 GeV ΔE = 31 MeV or 0.25%.
Hence in colliding beam experiments we have a very much smaller energy loss for given s, than in stat. target experiments, although the percentage loss is the same.

Let us look a little closer at the differences between colliding beam and stat. target experiments on diffraction dissociation. There is single diffraction dissociation in which either the beam or the target proton breaks up or double diffraction dissociation. So far we have compared single diffraction dissociation of either beam in colliding beam experiments with target diffraction dissociation in the case of stat. targets.

STATIONARY TARGET COLLIDING BEAMS

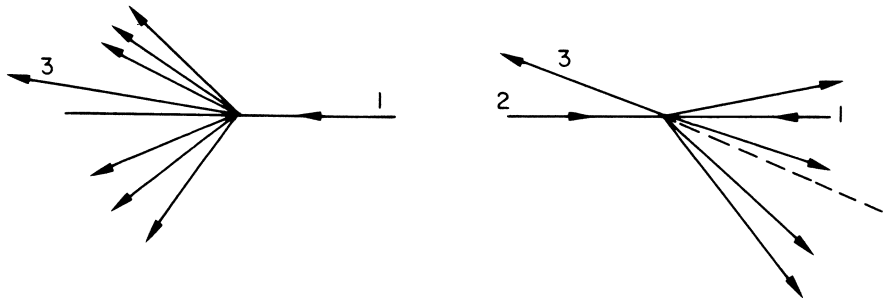

TARGET DISSOCIATION BEAM 2 DISSOCIATION

$$1 + 2 \rightarrow 3 + X_4$$

STATIONARY TARGET

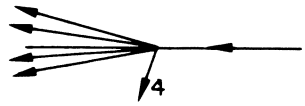

COLLIDING BEAMS

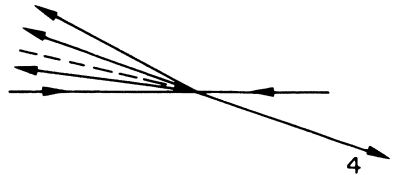

BEAM DISSOCIATION

BEAM 1 DISSOCIATION

$$1 + 2 \rightarrow X_3 + 4$$

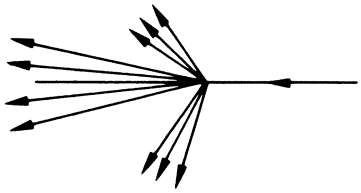

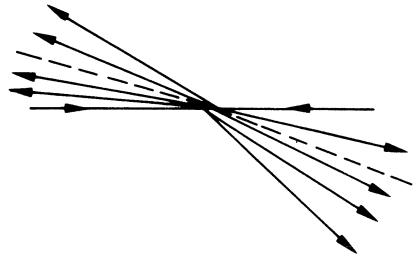

BEAM + TARGET DISSOCIATION

BEAM 1 + BEAM 2 DISSOCIATION

$$1 + 2 \rightarrow X_3 + X_4$$

Obviously in the latter case there is the other, non-symmetric, possibility of beam dissociation, with a single recoil proton coming off the target. In that case

$$-t = (\underline{p}_1 - \underline{p}_3)^2 = (\underline{p}_2 - \underline{p}_4)^2 = 2mT_4 \qquad (V.13)$$

where T_4 is the kinematic energy of the recoil proton, and

$$M^2 = m^2 + 2p_1p_4 \cos\theta_{14} - 2(m + E_1)T_4 \qquad (V.14)$$

In recoil detection the sensitivity of M^2 to the momentum of the incident beam is

$$\delta M^2_{p_1} \simeq M^2 \frac{\Delta p_1}{p_1} \qquad (V.15)$$

RECOIL OF STAT. TARGET

Comparing this with (V.10) one sees a reduction in sensitivity by a factor S/M^2, i.e. typically 20. The sensitivity to angle and kinematic energy of the recoil proton is sketched in fig. 1. For example, at $M^2 \simeq 20$ GeV^2 and $t \simeq 0.15$ GeV/c^2, a ±5% measurement of the kinetic energy results in $\delta M^2 \simeq \pm 0.6$ GeV^2. The sensitivity to angle is $\delta M^2 \simeq \pm 1$ GeV^2 per ±0.25°. Comparing this with colliding beam experiments at the same s: a ±0.5% measurement of the momentum of the produced proton results in (see (V.9)) $\delta M^2 \simeq \pm 3$ GeV^2, i.e. a factor of 5 worse although the accuracy of the energy measurement is a factor 10 higher. Hence missing mass experiments with colliding beams have intrinsically (i.e. independent of the quality of the detectors) a worse mass resolution than experiments on stationary targets in which angle and momentum of the recoil proton is measured.

Finally there is the question of minimum t. We have (considering protons only)

$$-t = (\underline{p}_1 - \underline{p}_3)^2 = 2m^2 - 2E_1E_3 + 2p_1p_3 - 4p_1p_3 \sin^2\theta/2$$

$$= 2m^2 - 2\frac{(E_1E_3 - p_1p_3)(E_1E_3 + p_1p_3)}{E_1E_3 + p_1p_3} - 4p_1p_3 \sin^2\theta/2$$

$$= m^2(2 - x - 1/x) - 4p_1p_3 \sin^2\theta/2 \simeq p_1p_3\,\theta^2 \qquad \text{(V.16)}$$

Note that (V.16) does not depend on p_2. In colliding beam machines the minimum angle at which positively charged particles can be detected is not zero, and is in fact rather large, due to the dimensions of the primary beams and the vacuum chamber in which they move. Typically $\theta_{LAB} = 35$ mrad. Example: ($p_3 \simeq p_1$) $p_1 = 15.5$ GeV/c $p_2 = 15.5$ GeV/c $s = 960$ GeV^2 $t_{min} = p_1p_3\theta^2 = 15^2 \times (35 \times 10^{-3})^2 = 0.28$. But since t_{min} does not depend on p_2 we can reach a smaller t_{min} by running with unequal energies: $p_1 = 11$ GeV/c, $p_2 = 22$ GeV/c, $s \simeq 960$ GeV^2, $t_{min} = 11^2 \times (35 \times 10^{-3})^2 = 0.15$ GeV/c^2.

For stationary targets and observing the fast proton (target dissociation), assuming $\theta_{min} = 1.5$ mrad and $p_1 = 300$ GeV/c we have $t_{min} = 0.20$ GeV/c^2. On the other hand, by measuring recoils one has (see (V.13)) $t = 2mT$. Using solid state devices or proportional counters one can measure down to (for example) 100 KeV. Thus $t = 0.0002$ GeV^2. This is another advantage of recoil detection on stat. targets.

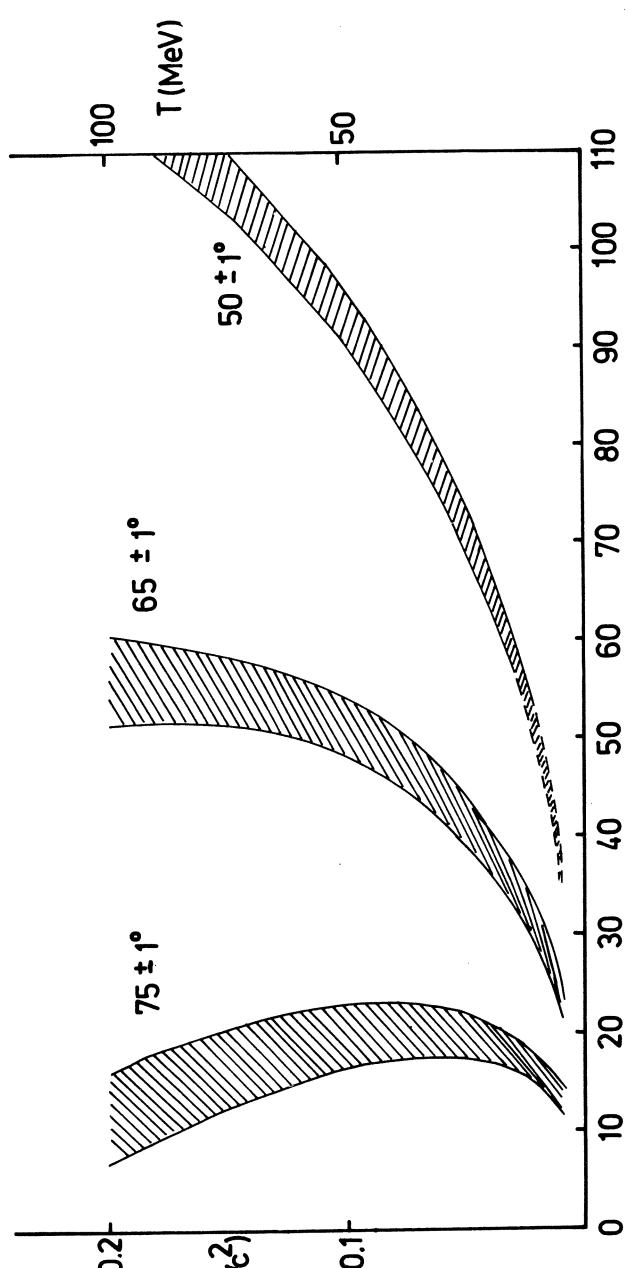

Fig. 1. Recoil detection in missing mass experiments on stationary targets. Dependence of t and M^2 on angle and kinetic T of the recoil proton. Data for p_{LAB} = 300 GeV.

V.2 Missing Mass Experiments at NAL and ISR

Two counter experiments have recently been performed at NAL in which angle and momentum of the target recoil in

$$p + p \rightarrow X + p$$

is detected, from which the diff. cross-section for excitation of mass X is then deduced.

The experiment of Sannes et al.[2] has been done by letting the circulating beam in NAL run through a hydrogen jet which is turned on twice at precisely defined times during the acceleration cycle, once at a fixed instant near the beginning of each cycle, the other at some chosen later time; the incident energy is varied by varying the latter switch-on time, while the relative normalization is obtained from the ratio of the yields during the two intervals. The acceleration ramp lasts ~2.5 sec, the jet is pulsed for 2 x 250 msec. The proton density in the jet is 2×10^{-7} g/cm^3. The beam profile is ~2 x 3 mm. The target x beam intensity in each burst is monitored by detecting elastically scattered events, at 86° and with T = 11.6 MeV, in a suitable placed solid state detector. Since the differential elastic cross-section is independent of s (apart from a 2.2% correction for shrinkage) this detector provides the absolute normalization (up to a geometrical factor) through:

$$\left(\frac{dN}{dt}\right)_{\text{finite t}} \rightarrow \left(\frac{dN}{dt}\right)_{t=0} = L \left(\frac{d\sigma}{dt}\right)_{t=0} = L \frac{\sigma_T^2}{16\pi}$$

USING SERPUKHOV DATA

USING SERPUKHOV + ISR DATA (±2.5%)

The target recoil is detected by range, see fig. 2. A coincidence $C_1C_2C_3C_4C_5C_6$ signals a proton stopping in absorber No. 2, with a momentum $560 < p_4 < 660$ MeV/c; a coincidence $C_1C_2C_3C_4C_5C_6C_7$ signals a stop in absorber No. 3, with $660 < p_4 < 780$ MeV/c.

The experiment is run in one of two ways

a) keep p_4, θ_4 fixed and vary p_1 in the range $40 < p_1 < 260$ GeV/c. Since

$$s = 2mE_1, \quad -t = 2mT_4, \quad M^2 = s\,(1 - (E_4 - p_4 \cos\theta_{14})/m)$$

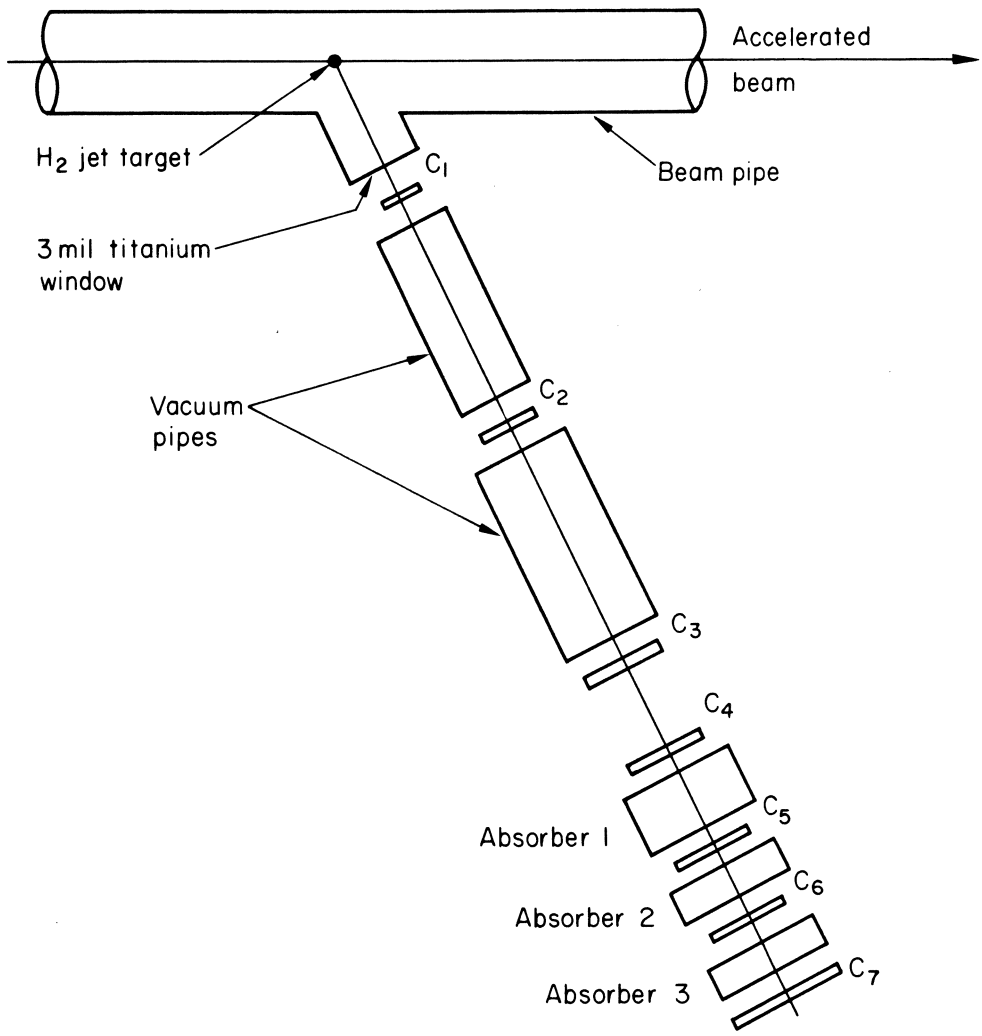

Fig. 2. Missing mass experiment of Sannes et al., at NAL. The missing mass is determined by angle and range of the recoil proton.

t and M^2/s are determined by p_4 and θ_4. For example:

p_4	θ_4	t	$M^2/s = 1 - x$	Proton stops in:
0.6	55.6°	- 0.33	0.18	absorber 2
0.7	55.6	- 0.45	0.17	absorber 3

b) keep s and p_4 (i.e.t) fixed and vary θ_4 by rotating the whole set up. In this way a range $0.06 < M^2/s < 0.21$ is covered at fixed t.

The final normalization is made by extrapolating down to $s = 56$ and 47 GeV^2 (BNL and CERN data).

The data show an inclusive differential invariant cross-section whose s-dependence is in good agreement with the form $A + B/\sqrt{s}$ at several pairs (x,t), see fig. 17 of section III. Furthermore the invariant cross-section at fixed t and s shows a minimum at $x \simeq 0.9$ followed by a rise up to the highest measured $x \simeq 0.93$. The shape does not depend much on s.

A second counter experiment[3], also detecting recoil protons has been done using an array of solid state detectors. 18 pairs of detectors are placed on a circle of ~1 m radius around a CH_2 or C target in an extracted proton beam at NAL (see fig.3). They are uniformly spaced between 48° and 89° with respect to the beam, each counter pair subtending ~0.4°. Each pair consists of two detectors, the first 1/2 mm thick, the second 5 mm thick, both 1 cm^2 in area. The first measures dE/dx, the second the total energy, if the kinetic energy T is less than 30 MeV, or otherwise the energy loss.

In the latter case T can be deduced from dE_1/dx and dE_2/dx up to T = 100 MeV. The relative calibration of the different pairs is monitored by means of elastic scattering: at each angle elastically scattered protons have a definite kinetic energy (see eq. (V.14) for M = m) and t, e.g. at $\theta = 75°$ T = 143 MeV, t = 0.28 GeV^2 (see fig. 1). The diff. cross-section versus M^2 for fixed t is obtained by taking the rates at fixed T, i.e. t, in the various pairs, hence the importance of relative normalization.

The data on protons are obtained by subtracting the data on C from those on CH_2. The normalization necessary for this procedure is obtained from deuteron and triton production which is the same in both targets. In the region of elastic events the C-background is small, but in the inelastic region the pp-spectrum is obtained by subtracting 90% of the data. Dead time corrections are relatively large since solid state detectors are inherently slow and the experiment is mounted very near to an intense primary beam. The

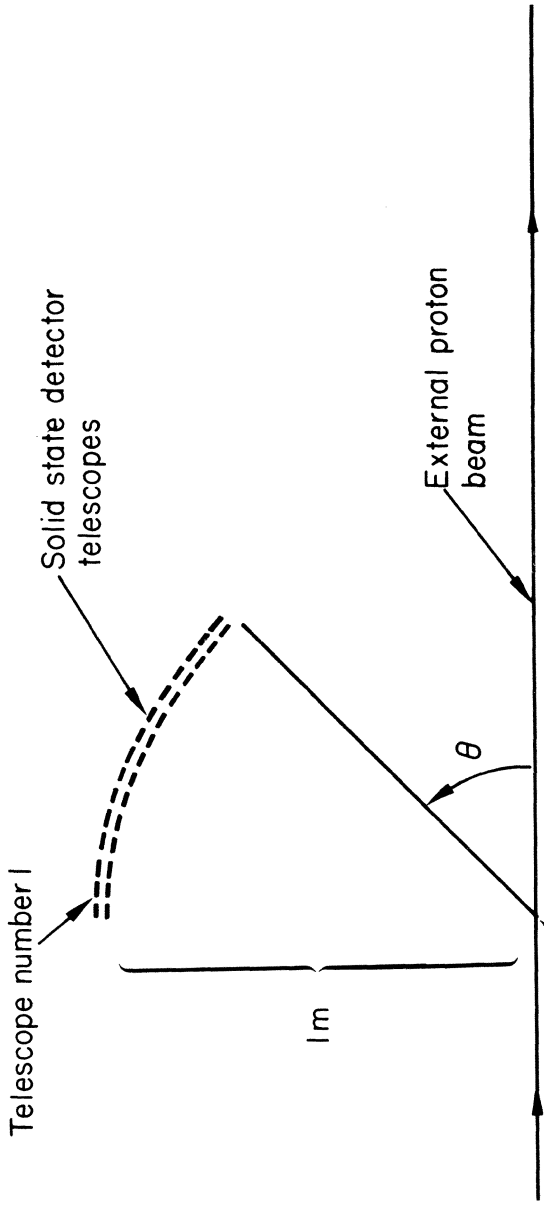

Fig. 3. Missing mass experiment of Childress et al., at NAL. The missing mass is determined by angle and kinetic energy of the recoil proton.

absolute normalization is by scaling the integrated elastic peaks to bubble chamber results on $d\sigma/dt$ at the same energy. This is expected to be accurate to $\lesssim$ 30%. The missing mass revolution, obtained from the slope of the elastic peaks is δM^2 = 1 GeV^2 (FWHM) at $|t| \simeq$ 0.03, 2 GeV^2 at t = 0.11 and 4 GeV^2 at t = 0.17 GeV/c^2. This is thus the measured resolution and includes the effects of finite resolution in θ and T.

At ISR missing mass experiments are being done with the set up shown in fig. 4[4,5]. The spectrometer consists of 5 magnets, 3 Cerenkov counters and a number of spark chambers and scintillators placed between the magnets. The axis of the spectrometer is at 85 mrad in the vertical plane through the intersecting beams, but other angles can be reached by moving the two first magnets and Cerenkov counters up and down. In this way particles produced at angles other than 85 mrad are guided towards the fixed part of the spectrometer. This feature is similar to that of the spectrometer mentioned in section IV (see fig. 1 of that section). In order to reach the smallest possible angle the first magnets are placed very close to the primary beams. Current-carrying septa cancel the strong stray field which would otherwise perturb the beams. The minimum angle is then determined by the available "free" space along the downstream beams and the thickness of the septa. In practice at ISR 35 < θ < 180 mrad. At a given setting the spectrometer accepts $\Delta\Omega = 10^{-4}$ sr, $\Delta p/p \simeq \pm 15\%$. The momentum resolution is $\delta p/p \simeq 0.8\%$ (FWHM), related to δM^2 as in eq. (V.9). Particles are identified by the Cerenkov counters and by time of flight.

Aspects of the data analysis have been discussed in section III. The normalization is obtained by means of monitor counters after calibration with the v.d. Meer beam steering method (section II).

A point particular to colliding beam experiments is the very broad range of momenta in the primary beams. This is because in filling the rings the successive pulses are put side by side by means of slight acceleration with an RF cavity. (see section I). The result is a ~5 cm wide ribbon (~3 mm high) in which the momentum varies from inside to outside by ~2%. Locating the point of origin in the diamond then gives the primary momenta of the event in question. The data can then all be scaled to, say, the central values of the primary momenta, by use of the relation:

$$\Delta x = \alpha \, \Delta p/p$$

where s is the coordinate "across" the beam and α is the known momentum compaction function. In this way the lack of knowledge of the primary momentum is reduced from, say, 500 MeV/c at 26 GeV/

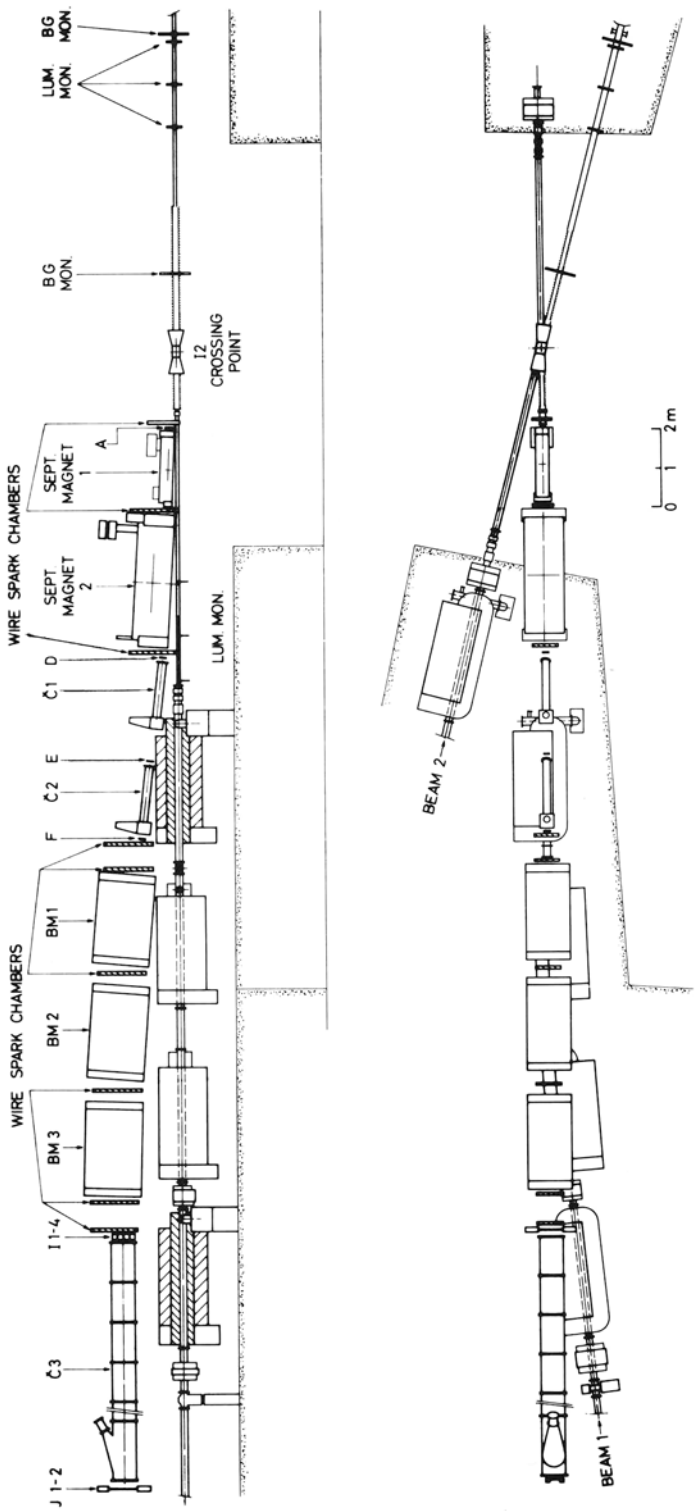

Fig. 4. Missing mass experiment of Albrow et al., at ISR. The missing mass is determined by angle and momentum of the proton in the spectrometer. $BM_{1,2,3}$ = bending magnets.

26 GeV to ~60 - 100 MeV/c and, with eq. (V.7), $\delta M^2 \simeq 50\ GeV^2 \rightarrow$ $\rightarrow$ 7-10 GeV^2. The remaining spread is due to the smearing out of the momentum/position relation by the betatron amplitudes. The spread can be further reduced by stacking discontinuously: in that case the only remaining uncertainty in momentum is that of the original bunch as it came from the accelerator which feeds the storage rings. This spread is of the order of 5 - 10 MeV/c. Hence by running with discontinuous stacks the effect of the spread in primary momentum on δM^2 is reduced to a level below that contributed by the error in the momentum measurement of the secondary proton. Fig. 5 shows data obtained with a stack consisting of three separate bunches. The top histogram shows the distribution of points of interaction across the vacuum chamber, as reconstructed from spark chamber tracks in the spectrometer of ref. 4. The histograms below show the distribution in momentum of events in the spectrometer, originating from each of the 3 bunches. A loose collinearity requirement on a particle going off in opposite direction has been applied in order to enrich the fraction of elastic events in the samples. The FWHM thus obtained is then a measure for the resolution of the spectrometer itself.

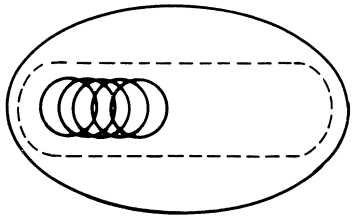

CONTINUOUS STACK

$\Delta x \rightarrow \Delta p \simeq 60 - 100$ GeV/c

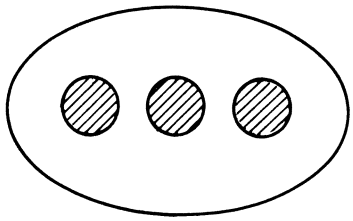

DISCONTINUOUS STACK

V.3 A Few Results

The data on $pp \rightarrow pX$ show the following features:

1) At fixed medium x and p_T or t the data approach a scaling limit from above in the range $100 < s < 360\ GeV^2$ and do not vary appreciably with energy for $s > 550\ GeV^2$, see fig. 6 and section III, fig. 17.
2) At high x a peak develops indicative for single diffraction dissociation in which the observed proton remains intact while the other one breaks up into a mass $M^2 \simeq s\,(1-x)$.
3) The shape and magnitude of the forward peak varies little with energy. Fig. 7.

These features will be analyzed in the next lecture.

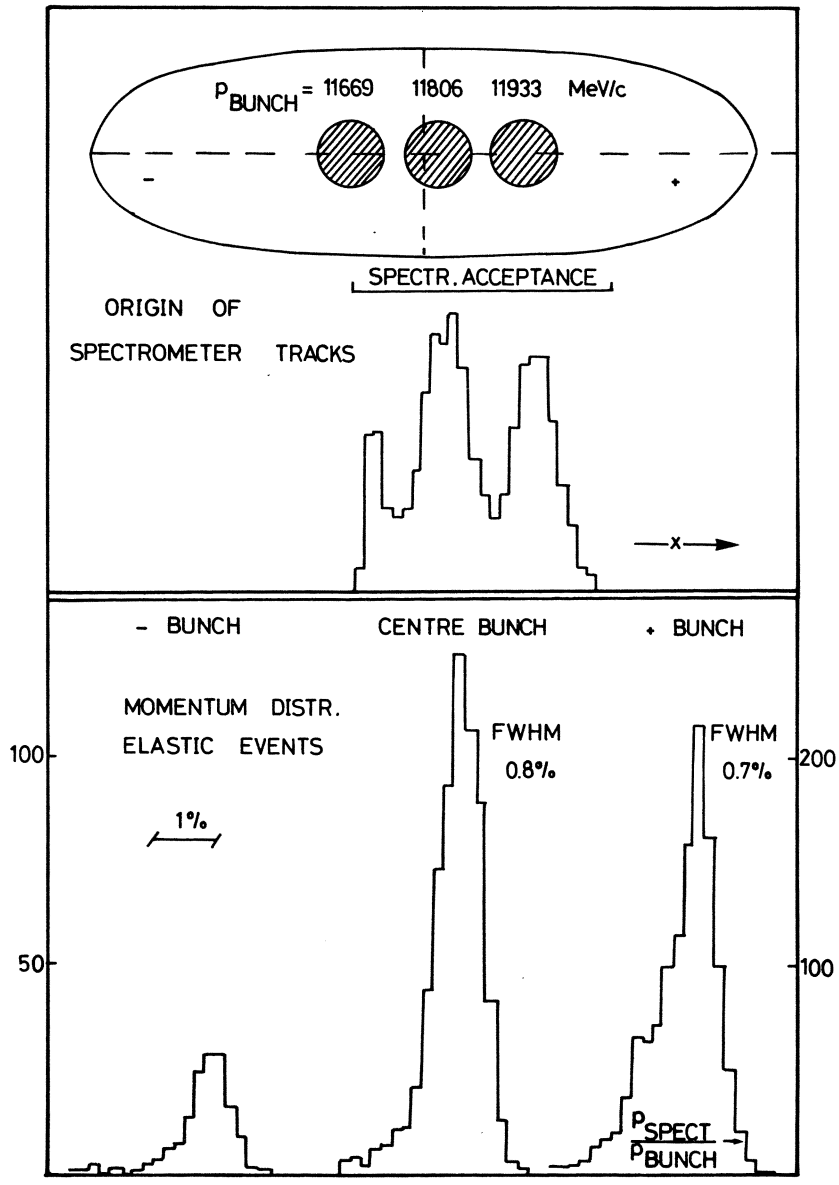

Fig. 5. Data on (quasi)-elastic scattering obtained with a discontinuous stack at ISR. Top histogram: distribution of origins of tracks in the spectrometer of ref. 5. Bottom histograms: momentum distribution of (quasi)-elastic events originating from each of the three bunches. The left bunch is at the edge of the spectrometer acceptance and hence contains less events than the others.

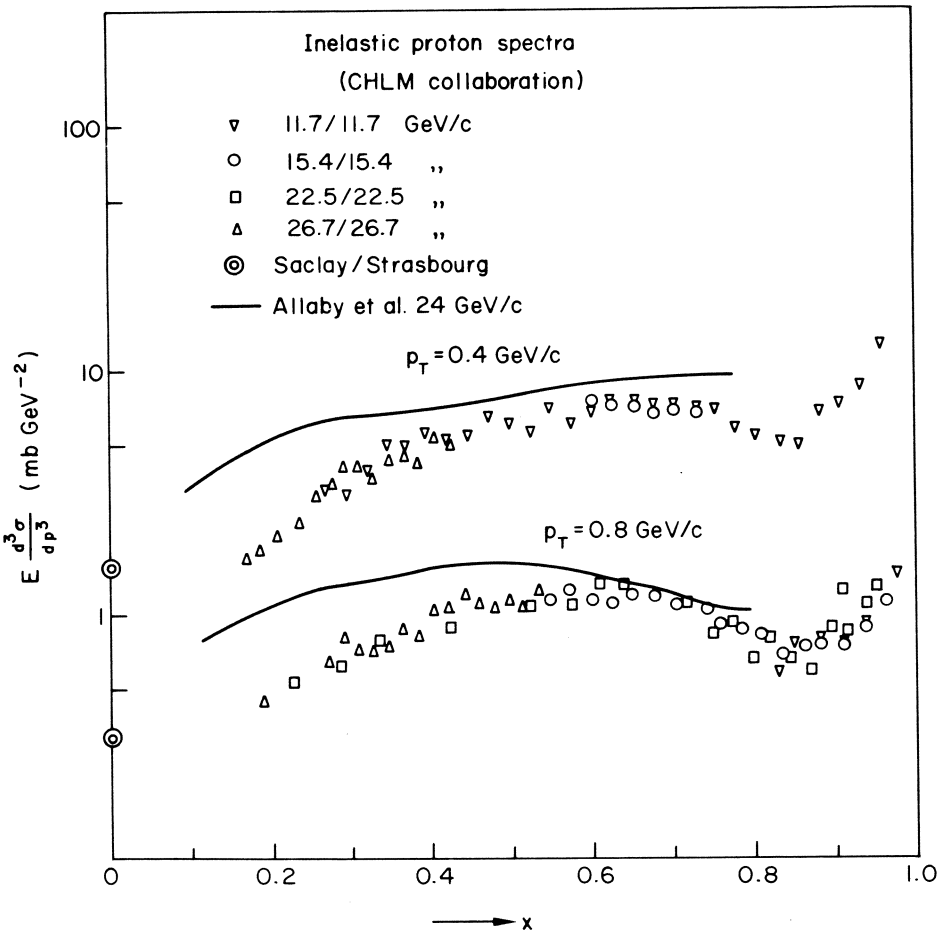

Fig. 6. Proton spectra at various ISR energies and fixed p_T, versus x.

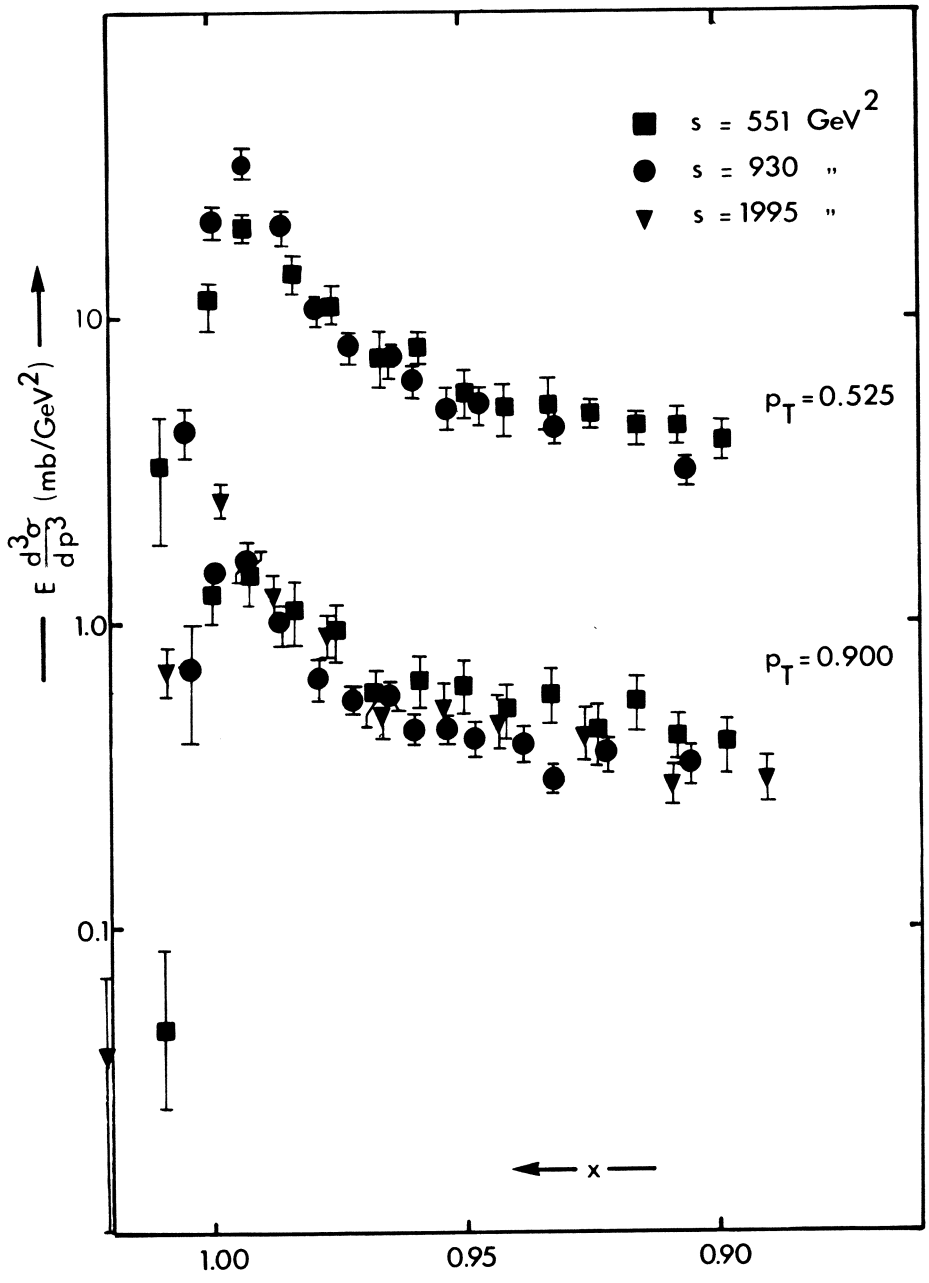

Fig. 7. Inelastic proton spectra at various ISR energies and fixed p_T, at high x.

SECTION V

REFERENCES

1) L. Foa, invited paper Aix-en-Provence Conference 1973;
M. Jacob, Lectures Louvain 1973;
E. Berger, Lectures 1973.
J.C. Sens, invited paper, Conf. Recent advances in Particle Physics, N.Y., 1973.

2) F. Sannes et al., Phys. Rev. Letters 30, 766, 1973.

3) S. Childress et al., NAL preprint.

4) M.G. Albrow et al., Nucl. Phys. B51, 388, 1972, Nucl. Phys. B54, 6, 1973.

5) M.G. Albrow et al., to be published in Nucl. Phys.

VI. HIGH ENERGY MISSING MASS DATA AND THE TRIPLE-REGGE LIMIT

In this section the ISR high energy missing mass data will be considered in the light of Reggeon-exchange.

VI.I The Triple-Regge Limit

Let us recall the Mueller-Regge picture of section III. Using the 3 particle optical theorem and Reggeizing the exchange if the appropriate (sub) energy $\to \infty$ as $s \to \infty$ we have obtained the central and fragmentation regions. We now go to the extreme end of the fragmentation region, i.e. there where one of the incident protons does not break up in the interaction with the other proton but retains its identity, just changing slightly its angle and momentum. This is the triple-Regge limit. Pictorially:

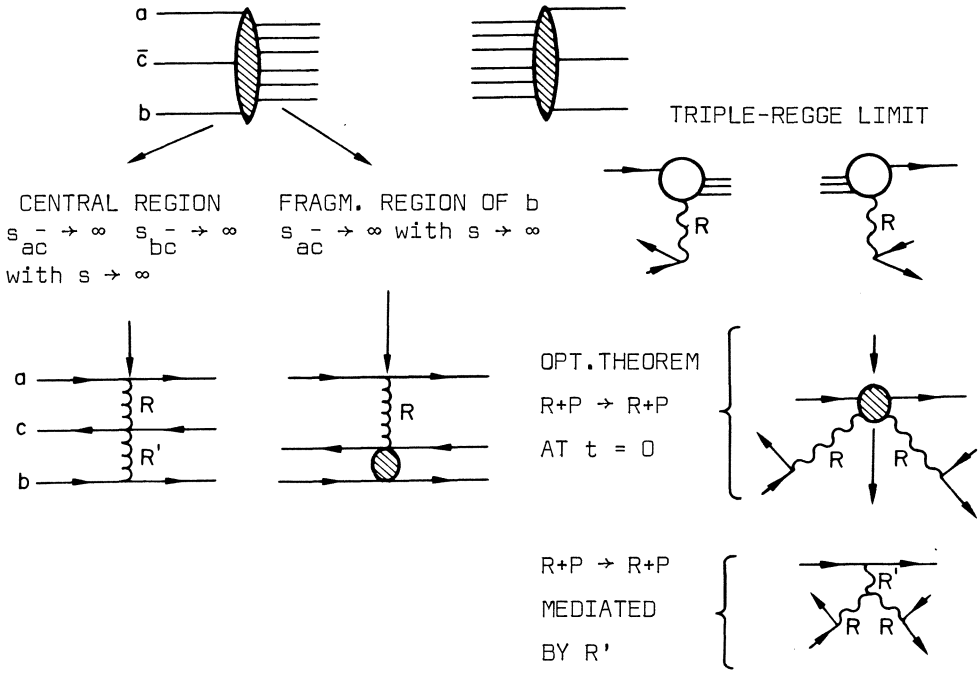

Putting the contributions of each vertex together into

$$E_c \frac{d^3\sigma}{dp_c^3} = \frac{1}{s} \text{DISC } T_{abc}^{-}(s_{ac}^{-}, s_{bc}^{-}, M^2)$$

one obtains

$$E_c \frac{d^3\sigma}{dp_c^3} = \frac{m_o^2}{16\pi^2 s} \sum_{iij} G_{iij}(t) \left(\frac{s}{M^2}\right)^{2\alpha_i(t)} \left(\frac{M^2}{m_o^2}\right)^{\alpha_i(0)} \qquad \text{(VI.1)}$$

To first order there are 4 terms: PPP, RRP, PPR and RRR. Their contributions are sketched in fig. 1. The invariant cross-section at t = 0 depends on x as listed below. Also indicated are the dependence on s of the integrated cross-section at t = 0.

	$\sigma_{inv}(t = 0)$	$\int_0^{X_{max}} d\sigma$
PPP	$(1-x)^{-1}$	$\sim \ln s/2m^2$
RRP	const.	$\sim 1 - 2m^2/s \to$ const. $s \to \infty$
PPR	$\frac{1}{\sqrt{s}}(1-x)^{-3/2}$	$\sim$ const.
RRR	$\frac{1}{\sqrt{s}}(1-x)^{-1/2}$	$\sim \frac{c}{s} + \frac{c'}{\sqrt{s}} \to 0$ $s \to \infty$

Fig. 1 and the table above show the trend of the various terms there are two scaling, two non-scaling terms. Only PPP has both a peak at large x and, after integration, rises with increasing s, as a result of the s-dependence of the limit of integration $X_{max} \simeq 1 - 2m^2/s$.

VI.2 Parametrization of the ISR Missing Mass Data

The observations on inclusive protonspectra, both at NAL and ISR, and in particular the occurrence of a pronounced peak in the inelastic data have met with great interest. Most simply stated the reason is that in observing the lone, unexcited proton in one c.m. hemisphere one measures the probability of raising the proton in the other hemisphere to an energy M, at a momentum transfer $\sqrt{t}$, directly; this in contrast to e.g. the

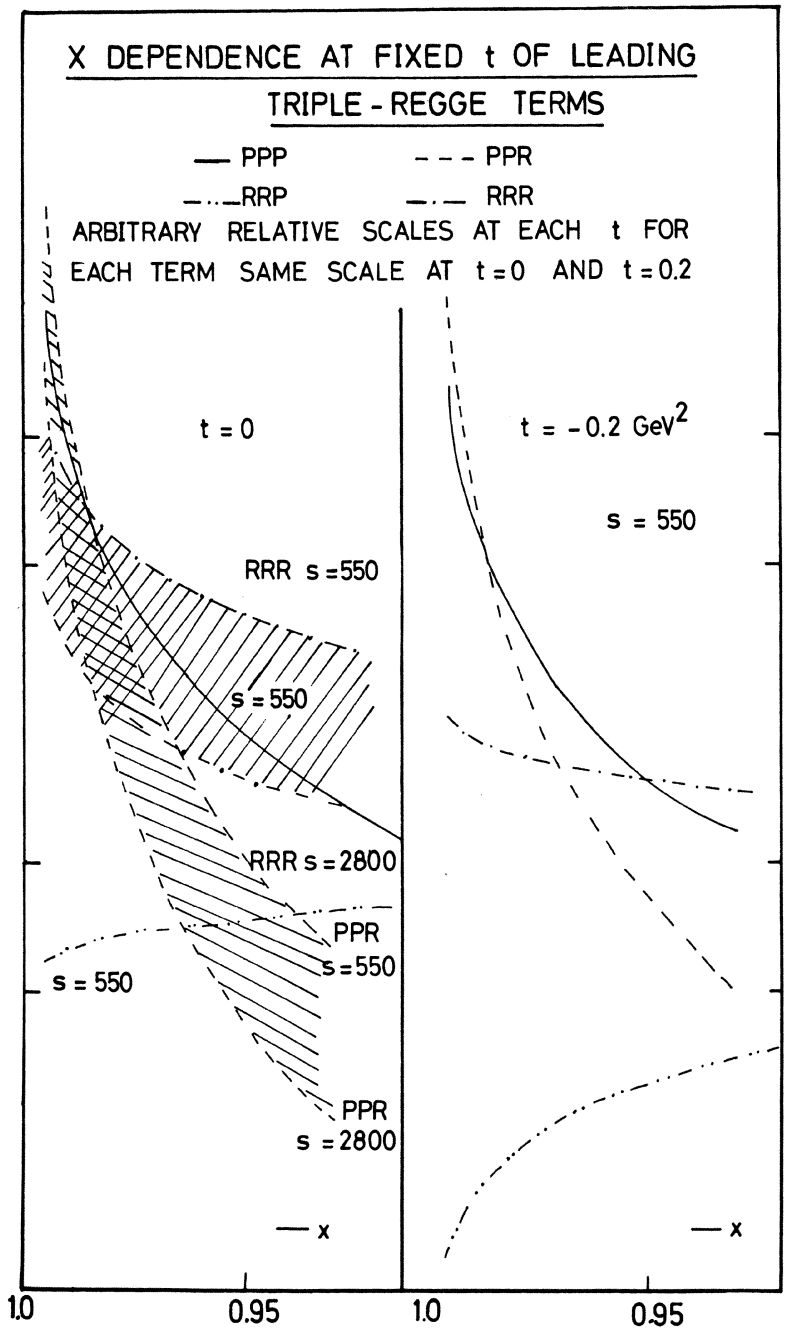

Fig. 1. Leading terms in the triple-Regge expansion.

observation of inclusively produced pions whose relation to the basic exchange of forces is "second hand", i.e. requires either an additional decay mechanism or information on the correlations with other particles produced simultaneously. Diffraction dissociation, of which the asymmetrically shaped inelastic peak is a manifestation, is responsible for approximately half of the average multiplicity of the secondaries. For this half it provides a qualitative understanding of the population distribution on the rapidity plot. The M^2, t and s-dependence of its cross-section has direct bearing on the nature of the Pomeron.

Triple-Regge fits to ISR missing mass data have been made by several authors[1]. The following is a summary of a recent, unpublished, analysis, and of some older results, by Albrow et al.[2]. The fits were made on the following data:

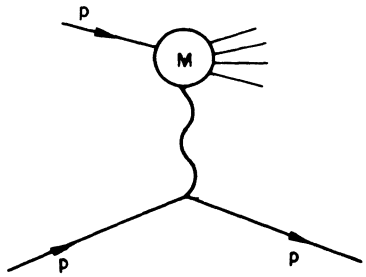

$s = 1995\ GeV^2$	$0.5 < x < 0.82^5$	$0.7 < p_T < 1.2$ GeV/c
$s = 551\ GeV^2$	$5 < M^2 < 30\ GeV^2$	$0.15 < t < 1.25$ GeV/c
$s = 930\ GeV^2$	$7 < M^2 < 50\ GeV^2$	$0.45 < t < 1.65$ GeV/c

The data at $s = 1995\ GeV^2$ are shown in fig. 2, a sample of the data at $s = 930\ GeV^2$ is shown in fig. 3.

In fitting the medium x data ($x < 0.82^5$) at $s = 1995\ GeV^2$ it has been assumed that the cross-section there is dominated by just one term in VI.1, the scaling RRP term. In view of the energy independence of the data (see section V, fig. 6) non scaling terms such as RRR or interference terms may be expected not to contribute more than, say, 20% to the cross-section. For the RRP term, with R = f = effective meson trajectory, we have

$$E\frac{d^3\sigma}{dp^3} = \frac{m_o^2}{16\pi^2 s} G_{ffP}(t) \left(\frac{s}{M^2}\right)^{2\alpha_f(t)} \left(\frac{M^2}{m_o^2}\right)^{\alpha_P(0)} \qquad \text{(VI.2)}$$

with $m_o^2 = 1$ and $\alpha_P(0) = 1$

$$E\frac{d^3\sigma}{dp^3} = \frac{G_{ffP}(t)}{16\pi^2} \left(\frac{M^2}{s}\right)^{1-2\alpha_f(t)} \qquad \text{(VI.3)}$$

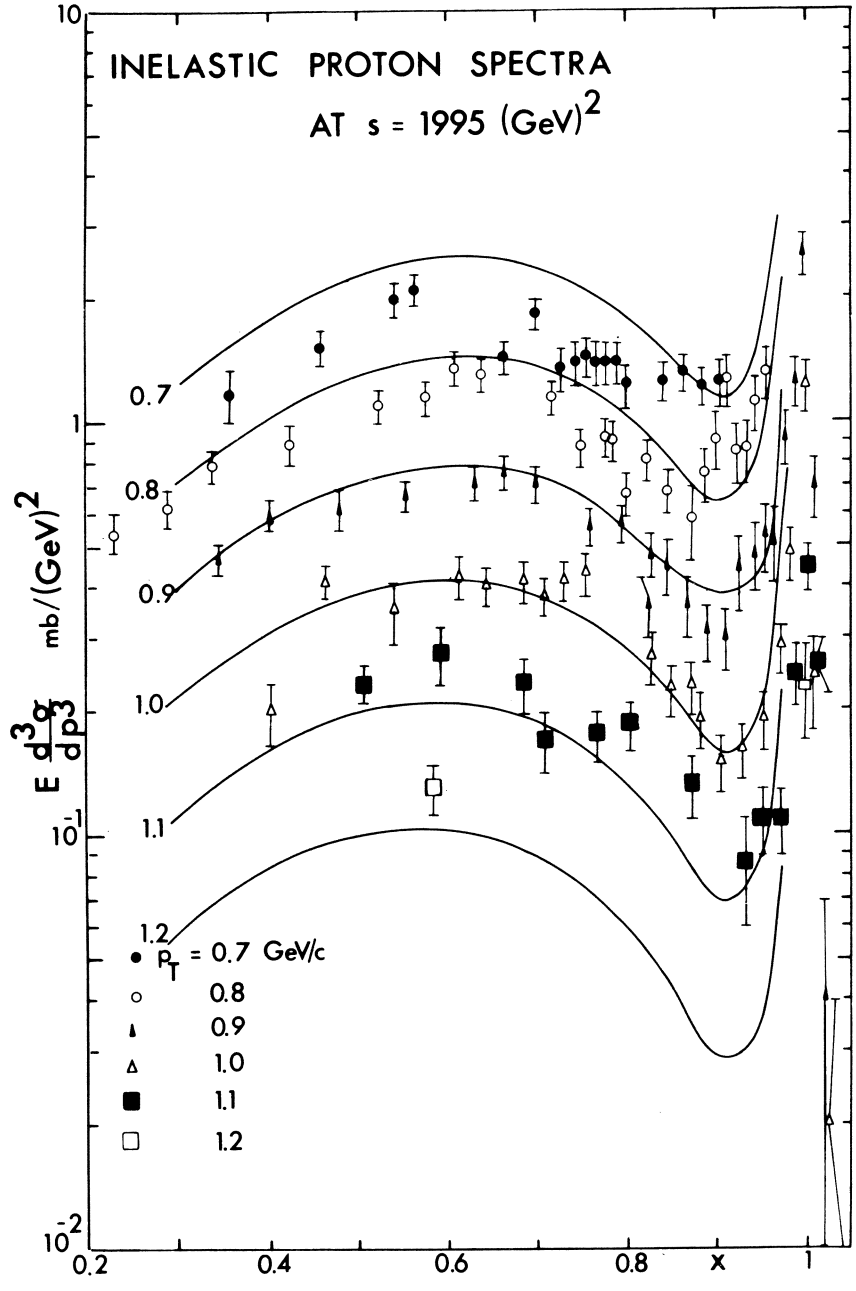

Fig. 2. Data on pp → pX at s = 1995 GeV^2. The points at $0.5 < x < 0.82^5$ were used to obtain the RRP triple-Regge cross-section.

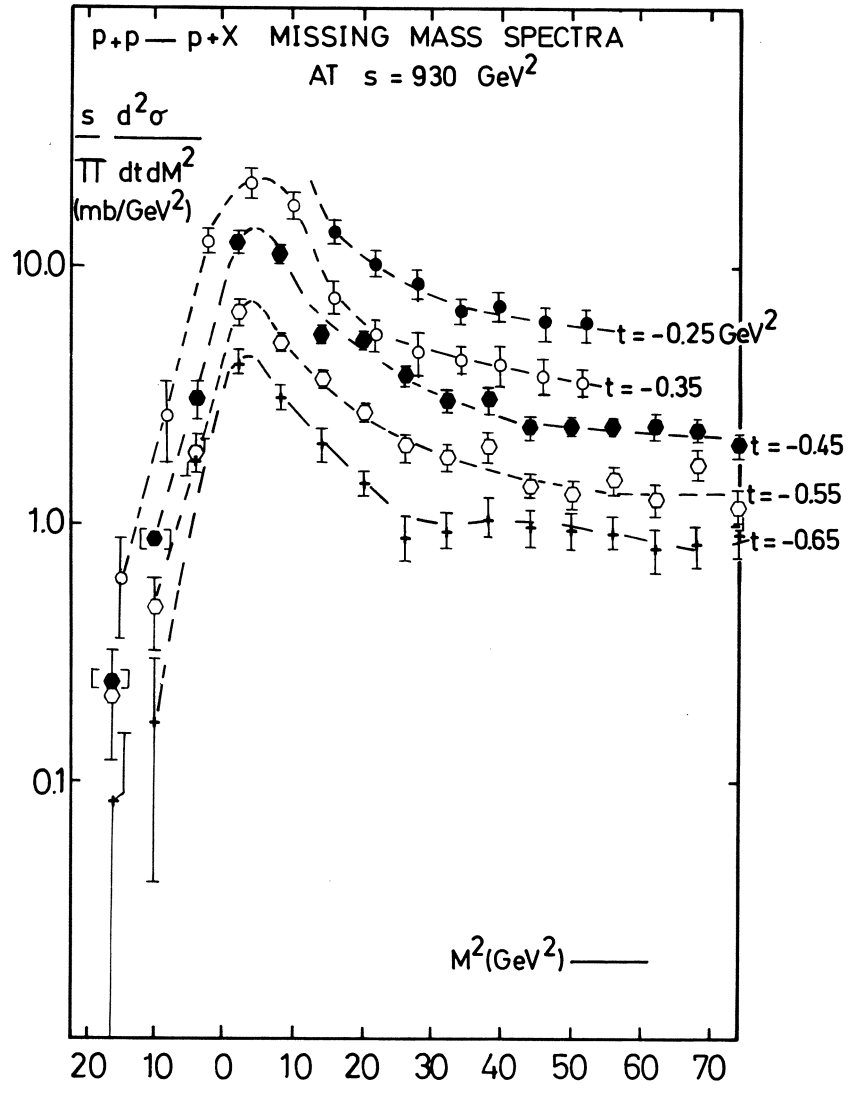

Fig. 3. Data on pp → pX at s = 930 GeV^2. The points at $7 < M^2 < 50$ at $0.45 < t < 1.65$ were used to obtain the PPP triple-Regge cross-section. Elastically scattered protons have been removed.

Data at $s = 1995\ GeV^2$ are consistent with

$$\alpha_f = 0.45 + 0.75\ t \qquad \text{(VI.4)}$$

for an effective meson trajectory. The trajectory is shown in fig. 4, the dotted line there indicates the sensitivity to a change of slope. Note that this result is independent of the absolute normalization. Substituting (VI.4) into (VI.2) one obtains for $G_{ffP}(t)$

$$G_{ffP}(t) \simeq 1100\ mb/GeV^2 \qquad \text{(VI.5)}$$

independent of t. The latter result is dependent on normalization.

The analysis of the forward peaks at $s = 551$ and $930\ GeV^2$ is less straight forward:

a) A substantial fraction of the raw data in the peak is due to elastic scattering. They are separated from the inelastics by requiring a second particle to emerge collinearly in the opposite hemishpere. The effect of applying a collinearity cut is shown in fig. 5. The elastic peak thus obtained is used to check the momentum scale. The t-dependence of the elastic data is checked to be in agreement with published results.

b) The momentum spread in the primary beams and the measuring errors on the secondary proton momentum (see section V.1) modify the shape of the peak. The elastic scattering data in a) show a peak whose width is a measure for the overall resolution of the equipment. The result, expressed as δx, δM^2 and standard deviation of the momentum curve for elastic events:

s_1	δM^2	δx (FWHM)	St.dev.in p
$551\ GeV^2$	$11\ GeV^2$	2%	0.85%
$930\ GeV^2$	$9.6\ GeV^2$	1%	0.42%

These data are used to fold resolution functions of the specified withs (corresponding to Gaussian with standard deviations of 4.7 and $3.9\ GeV^2$ resp.) into the triple-Regge formula (VI.2).

c) At high x the spectrum is composed partly of diffractively scattered protons, partly of high momentum fragmentation protons. The latter contribution can be subtracted by

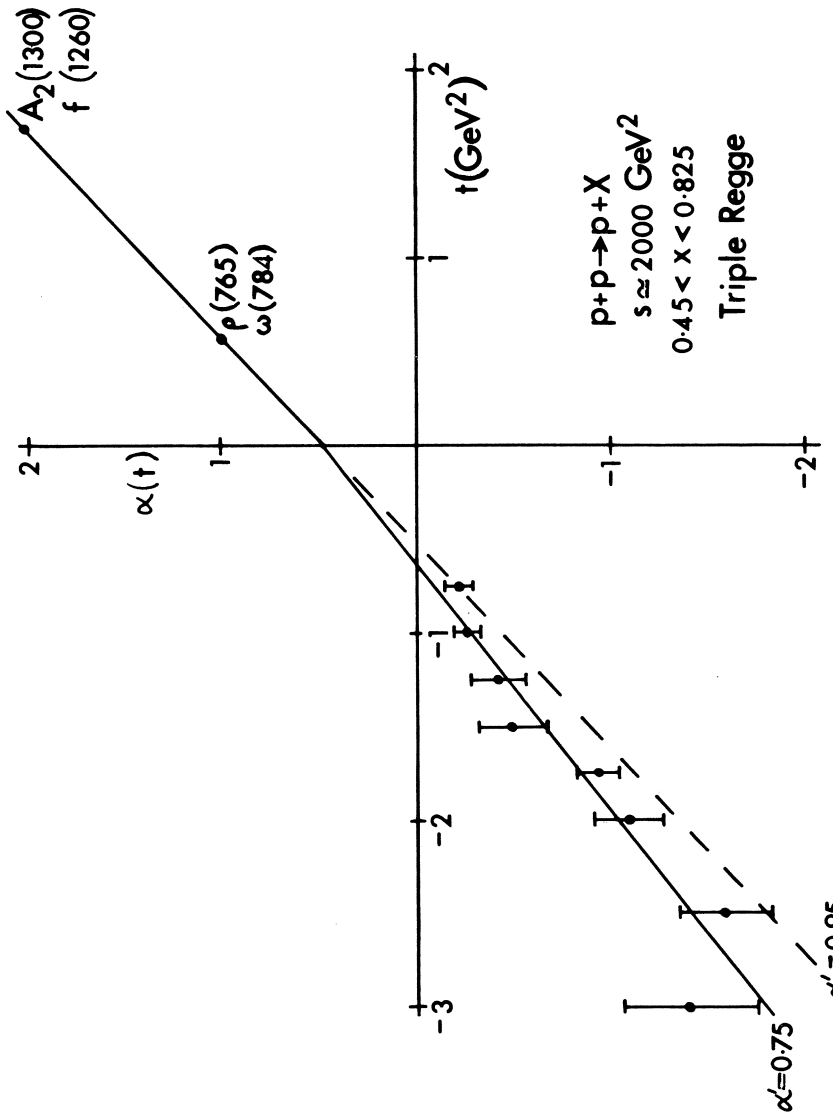

Fig. 4. Effective meson trajectory obtained from the data of fig. 2.

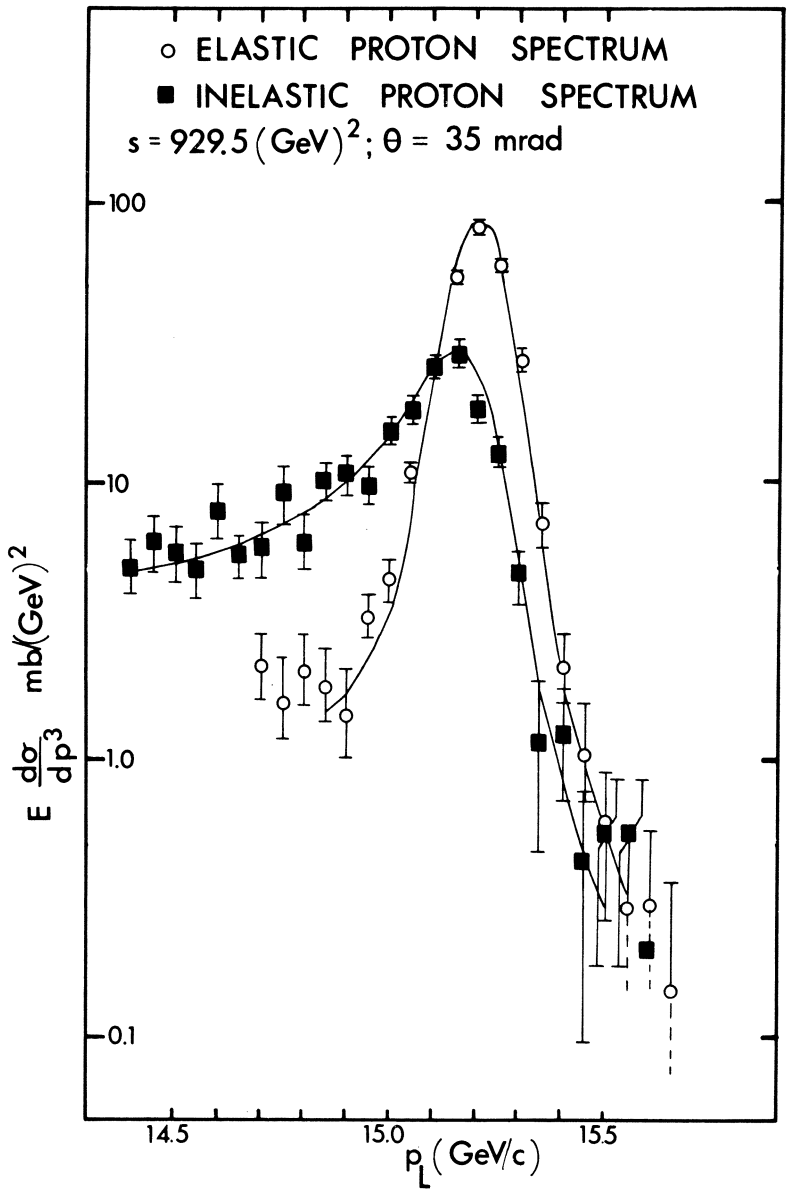

Fig. 5. Separation of elastic from inelastic events by means of applying a cut on the angle between the proton in the spectrometer and one other particle going into the opposite hemisphere.

assuming its x-dependence to be specified by the scaling RRP triple-Regge term, as suggested by the data at s = 1995 GeV^2 above. The effect of subtracting a "background" of the form of eq. (VI.2) with trajectory (VI.4) is shown in fig. 6.

With these problems out of the way we now look at the data and note that 1) there is little if any dependence on s; 2) at the lowest t measured the slope of the M^2 distribution is $B(t = 0.15) = 0.98 \pm 0.06$. This suggests dominance of the PPP term, since, at t = 0:

$$\text{PPP} \qquad \sigma_{inv} \sim \frac{1}{1-x} \sim \left(\frac{M^2}{s}\right)^{-1}$$

$$\text{PPR} \qquad \sigma_{inv} \sim \frac{1}{\sqrt{s}} \sim \frac{1}{(1-x)^{3/2}} \sim \frac{1}{\sqrt{s}} \left(\frac{M^2}{s}\right)^{-1.5}$$

$$\text{RRR} \qquad \sigma_{inv} \sim \frac{1}{\sqrt{s}} \sim \frac{1}{(1-x)^{1/2}} \sim \frac{1}{\sqrt{s}} \left(\frac{M^2}{s}\right)^{-0.5}$$

while interference terms such as PRP would have $B(0) \sim 0.5$ (although this term would scale). If we then assume PPP to be the only important term we have

$$E \frac{d^3\sigma}{dp^3} = \frac{G_{PPP}(t)}{16\pi^2} \left(\frac{M^2}{s}\right)^{1-2\alpha_P(t)} \qquad \text{(VI.6)}$$

Fitting this to the data, and taking into account points a, b, c above, gives the result:

$$\alpha_P(t) = 1.0 + 0.2t \qquad \text{(VI.7)}$$

as the effective Pomeron trajectory, see fig. 7. Note again that this result is independent of the normalization. The data at both energies, s = 551 and 930 GeV^2, are consistent with the same trajectory.

Encouraged by the results we now look for confirmation or denial in other processes. If elastic scattering were dominated by Pomeron exchange we would parametrize the differential cross-section with the expression

$$\frac{d\sigma}{dt} = f(t)\, s^{2\alpha_P(t)-2} \qquad \text{(VI.8)}$$

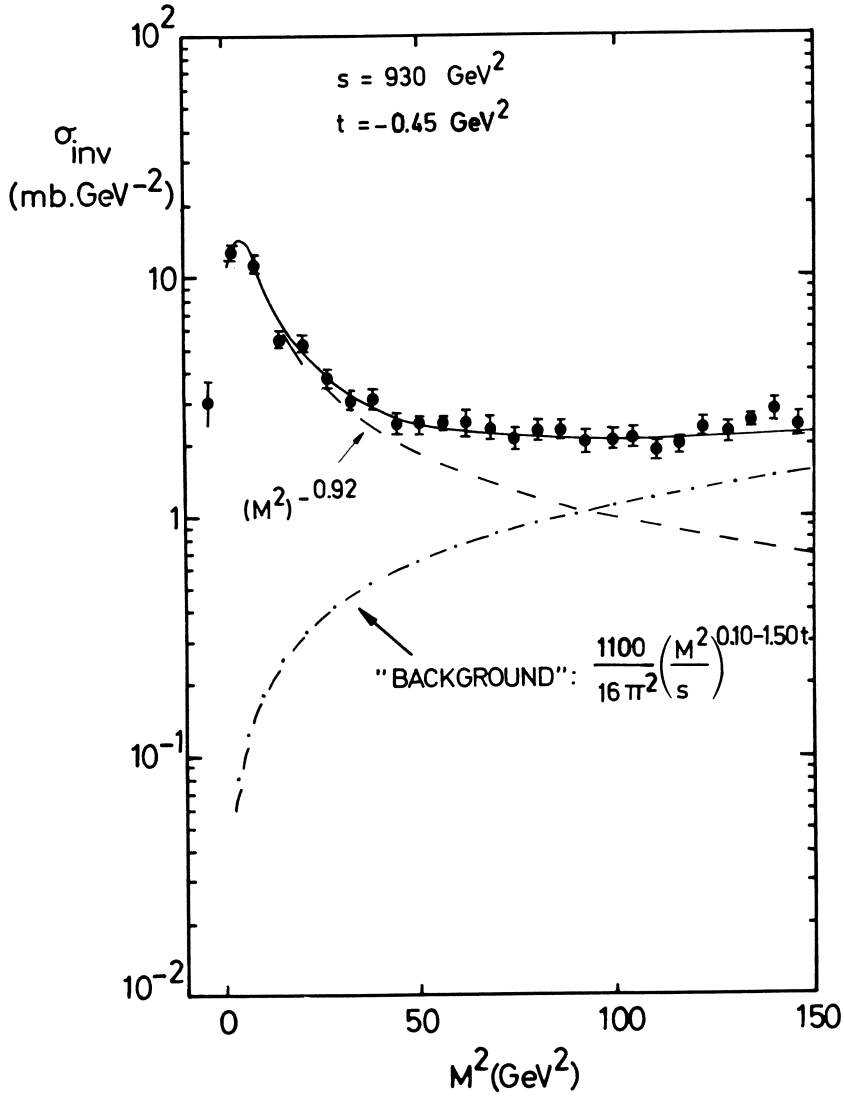

Fig. 6. Decomposition of the forward peak in pp → pX into contribution arising from leading protons and from fragmentation protons ("background").

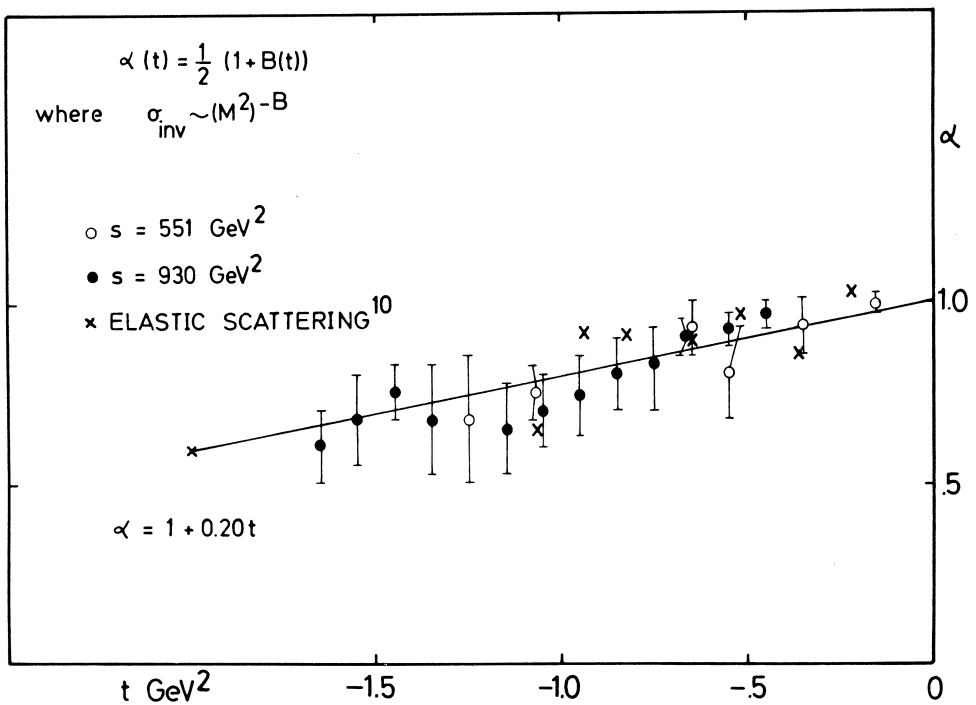

Fig. 7. Effective Pomeron trajectory obtained by fitting the PPP triple-Regge term to the pp → pX at s = 551 and 930 GeV^2 after correction for elastic events, effects of finite resolution, and contributions by fragmentation protons, Ref. 3.

Using recent data at the same energies, s = 551 and s = 930 GeV^2, we then find the crosses in fig. 7, also suggesting that the Pomeron trajectory has a small, but non-zero slope.

It is of interest to check the whole triple-Regge idea in reactions where quantum number exchange restricts the possible exchanges. One case is pp → π^+X. The only possible terms are now RRP and RRR with R = nucleon trajectory. Since RRP → const. and RRR → $1/\sqrt{s}$ (see table above) we expect the scaling limit to be approached as A + B $\sqrt{s}$, in accord with data (see section III, fig. 17) A fit[3] to data (see fig. 8) at fixed p_T = 0.8 GeV/c versus x at s = 2000 GeV^2 results in

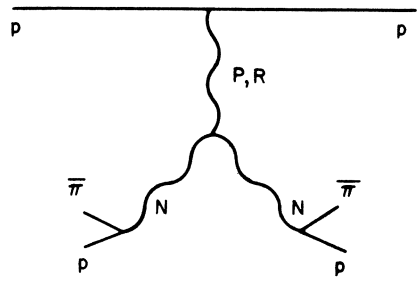

$$\alpha_N = -0.35 + 1.0\ t \quad \text{(VI.9)}$$

a not unreasonable value for the nucleon trajectory. Note that experimentally such data are difficult to obtain due to the very steep drop in cross-section with increasing x in the absence of PPP and PPR contributions.

Recently[4], data on pp → nX at s = 530, 930, 2025 and 2800 GeV^2 in limited regions of x and p_T have been analyzed with a single RRP term dominating the spectrum at all x. As expected the data show no forward peak. The data, shown in fig. 9, are not complete enough to map out a full trajectory but they are consistent with an effective meson trajectory given by

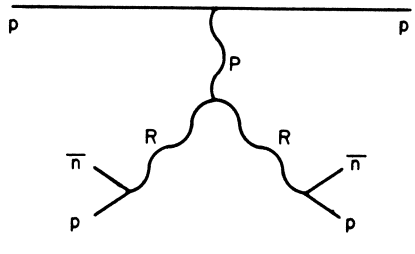

$$\alpha_R = 0 + 1.5\ t \quad \text{(VI.10)}$$

This is suggestive of the π-dominance at the $\bar{n}$p vertex. Note that this is in contrast, but not in contradiction, to the effective meson trajectory (VI.4) which is dominated by ρ exchange.

In conclusion one might say that in spite of the many assumptions and the very incomplete data, the classical Regge-exchange picture of strong interactions, carried as close to its

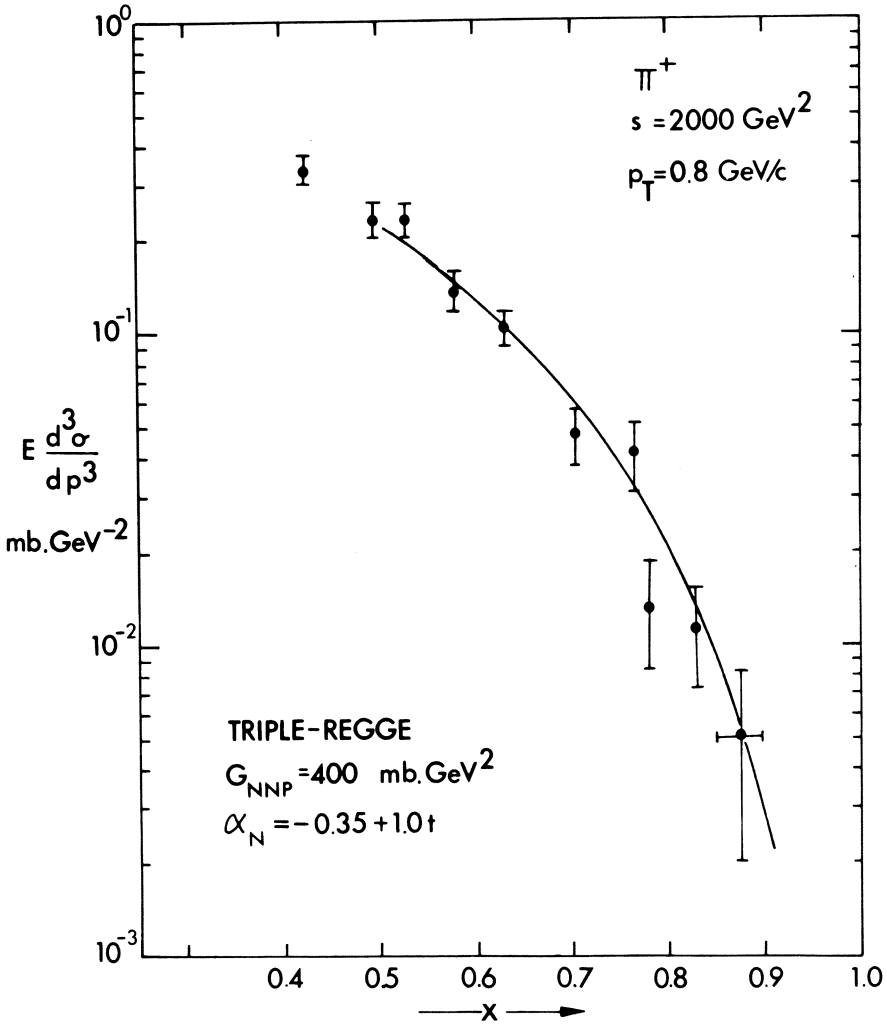

Fig. 8. Inclusive π^+ production versus x at p_T = 0.8, compared with a fit to the R(=N) R(=N) P triple-Regge term. (M.G. Albrow et al., unpublished).

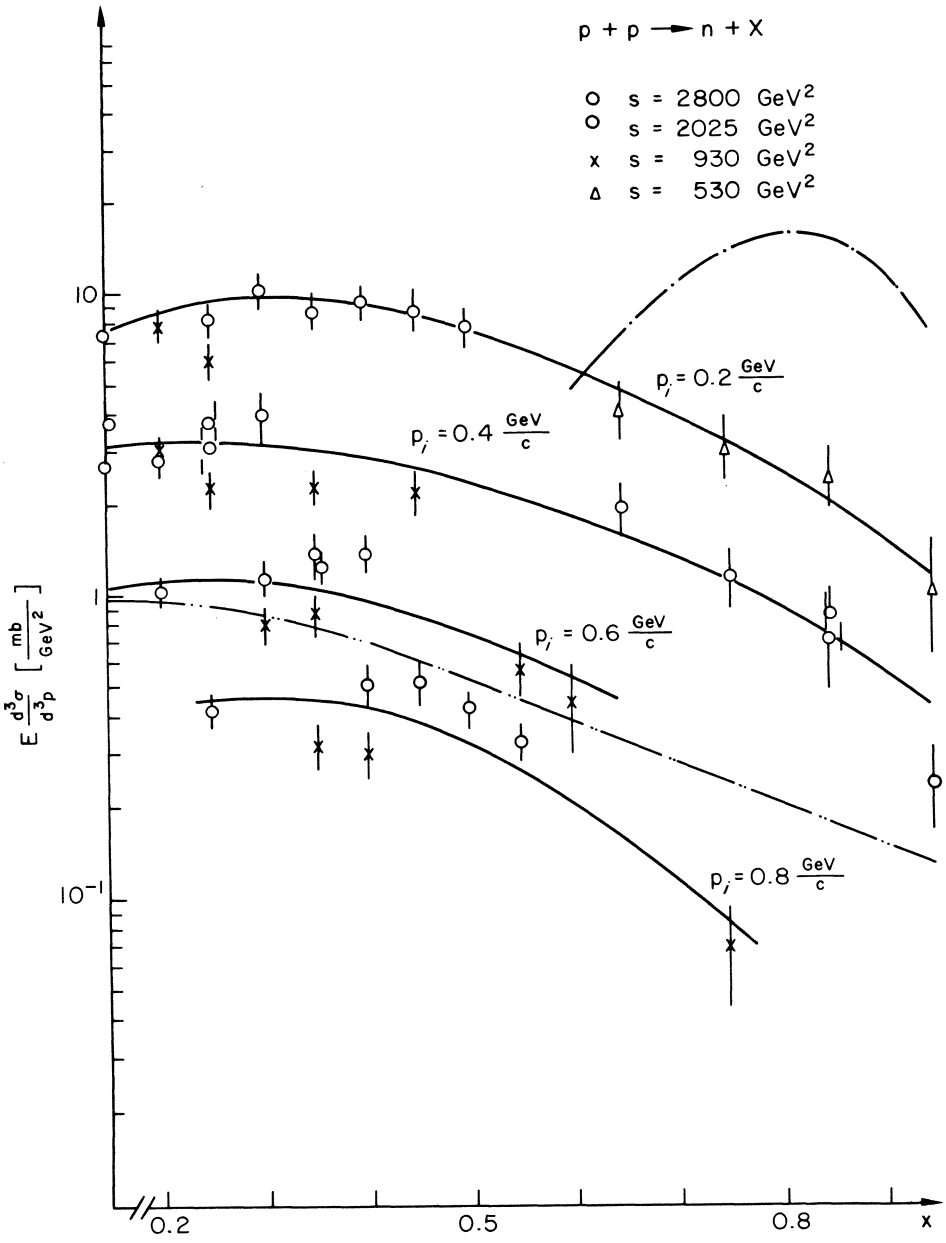

Fig. 9. Data of ref. 4 on pp → nX at various s and p_T. These data have been used to extract an effective meson trajectory, by fitting to the RRP triple-Regge term. The result suggests π-exchange dominance in pp → nX.

asymptotic limits as present apparatus permits, provides a consistent description of particle production data and leads to "reasonable" effective Pomeron, nucleon and meson trajectories.

VI.3 Processes Contributing to the Rise in σ_{TOT}

The data discussed in section VI.2 on $pp \to pX$ at $s = 551$ and 930 GeV^2 permit one further conclusion. Either by substituting the trajectory (VI.7) into (VI.6) or by using the "experimental" numbers for the slopes of the M^2 distributions at fixed t on a log-log plot one obtains the quantity $G_{PPP}(t)$ as a function of t. The result is shown in fig. 10 ("trajectory" data above, "measured slope" data below). The result at the two energies is the same, both in slope and in magnitude. (This latter conclusion depends on the normalization). The t-dependence is non-exponential and can be parametrized in several ways, e.g. as

$$G_{PPP}(t) = A \exp (Bt + Ct^2) \qquad \text{(VI.11)}$$

with

$$A = 150 \text{ mb/GeV}^2 \qquad B = 4.3 \text{ GeV}^{-2} \qquad C = 1.09 \text{ GeV}^{-4}$$

or as

$$G_{PPP}(t) = A_1 \exp B_1 t + A_2 \exp B_2 t \qquad \text{(VI.12)}$$

with $A_1 = 140$ $A_2 = 8.8$ mb/GeV^2 $B_1 = 4.3$ $B_2 = 0.76$ GeV^{-2}

(The latter fit is drawn as the solid line in fig. 10).

The quantity $G_{PPP}(t)$ is of fundamental interest. It links various processes and prescribes their behaviour at energies above the presently available ones. Inspection of the triple-Regge diagram shows that $G_{PPP}(t)$ is the product of 4 factors:

$$G_{PPP}(t) = |\beta_{ppP}(t)|^2 \beta_{ppP}(0)\, g_{PPP}(t,t,0) \qquad \text{(VI.13)}$$

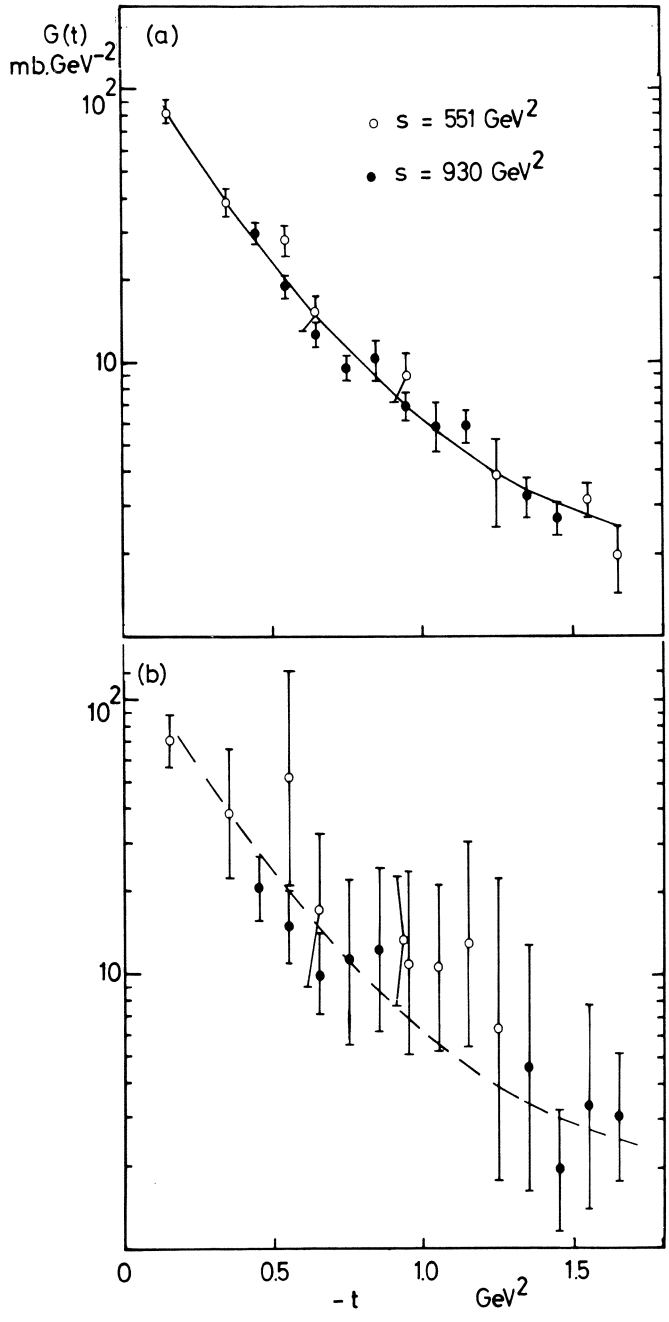

Fig. 10. The "overall" PPP coupling constant as a function of t, extracted from pp → pX data at s = 551 and 930 GeV^2, see text. See eq. (VI.13) for a break-down of $G_{PPP}(t)$ into its components.

Now in elastic scattering

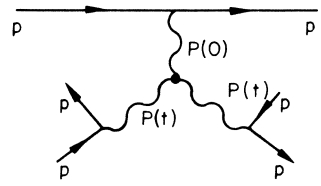

$$\frac{d\sigma}{dt}(t) = \frac{1}{16\pi} |\beta_{ppP}(t)|^2 |\beta_{ppP}(t)|^2 s^{2\alpha_P(t)-2} \qquad \text{(VI.14)}$$

while the total cross-section is given by

$$\sigma_T = \beta_{ppP}(0)\ \beta_{ppP}(0)\ s^{\alpha_P(0)-1} \qquad \text{(VI.15)}$$

and thus

$$g_{ppp}(t,t,0) = G_{PPP}(t) \left[16\pi\ \sigma_T \frac{d\sigma}{dt}(t) s^{2-2\alpha_P(t)}\right]^{-1/2} \qquad \text{(VI.16)}$$

Hence the triple-Pomeron coupling constant g_{PPP} can be determined from a combination of data on elastic scattering, the total cross-section and diffractive inelastic scattering. In putting in various recent data (details omitted here) it turns out that the t-dependence of $G_{PPP}(t)$ is largely cancelled by the t-dependence of the bracket in (VI.16), yielding a triple Pomeron coupling constant $g_{PPP}(t) \simeq 0.4\ \text{GeV}^{-1}$, not or very weakly dependent on t in the range $0.15 < t < 0.8\ \text{GeV}^2$ (above $t \simeq 0.8$ the dip at $t = 1.4\ \text{GeV}^2$ affects the results).

This result can be put into a different form by rewriting the triple Pomeron expression for the cross-section, with (VI.2) and (VI.13):

$$E\frac{d^3\sigma}{dp^3} = \frac{1}{16\pi^2} |\beta_{ppP}(t)|^2 \left(\frac{M^2}{s}\right)^{\alpha_P(0)-2\alpha_P(t)} \sigma_{pP}(M^2,t) \qquad \text{(VI.17)}$$

with

$$\sigma_{pP}(M^2,t) = \beta_{ppP}(0)\ g_{PPP}(t)\ (M^2)^{\alpha_P(0)-1} \qquad \text{(VI.18)}$$

(only the PPP-term has been retained for clarity; other terms could be included).

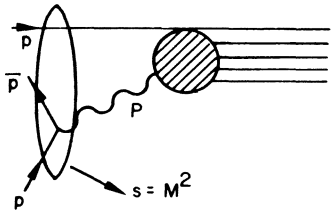

$\sigma_{DP}(M^2,t)$ is the Pomeron-proton total cross-section at total energy $s = M^2$ and with mass^2 = t

Since dependence on t in (VI.18) enters only through $g_{PPP}(t)$ the result above (constant g_{PPP}) seems to say that there is no strong dependence on the "Pomeron mass". As to the dependence on M^2: if PPP is a good description of the data, then $\sigma(M^2,t)$ should be independent of M^2. Explicit evaluation of (VI.17) and (VI.14) using the elastic and inelastic (with peaks corrected for fragmentation protons as in section VI.2) data at $s = 551$ GeV^2 and at $t = -0.15$ and -0.35 GeV^2 gives the points shown in fig. 11. The result is independent of energy (M^2), as is pp scattering in the same energy (s) range.

This view of the interaction in terms of the total proton-Pomeron cross-section has another interesting consequence. In the limit where this picture is valid (high s, high M^2, small t) the average multiplicity of events produced in proton-Pomeron interactions should depend in the same way on the total energy $s = M^2$ as the overall average multiplicity in proton-proton interaction depends on s. In particular the coefficient A in

$$\langle n \rangle_D = A \ln M^2 \qquad\qquad \langle n \rangle = A \ln s$$

should be the same. There is evidence in NAL bubble chamber experiments that this is in fact the case.

One remaining question is the value of $g_{PPP}(t)$ at $t = 0$ and how this value is approached. To get a feeling for how this might go we extrapolate the PPP cross-section obtained from the ISR data to the t-range covered by the recoil detection experiment at the same s at NAL (see section V). The RRP term has been added in order to account for the contribution of the fragmentation protons at large M^2. The result is shown in fig. 12. It is seen that in the mass range in which the PPP fit has been made ($5 < M^2 < 30$ GeV^2) the agreement between the NAL data and the PPP + RRP curve is reasonably good. One might interpret this as saying that down to $|t| = 0.056$ GeV^2 there is no sign of any turn-over in $G_{PPP}(t)$. If this trend were to continue down to $t = 0$ we would have that

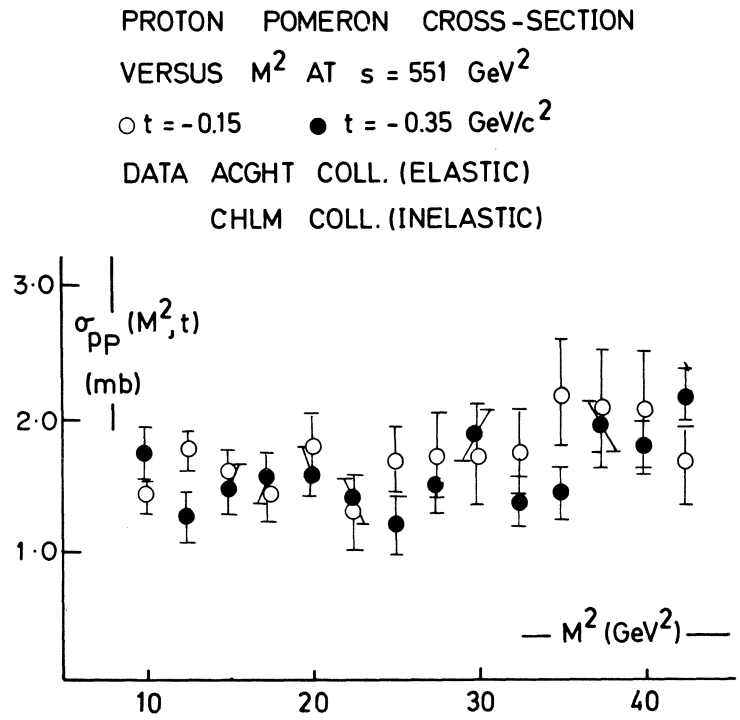

Fig. 11. Total effective Pomeron-proton cross-section as a function of the total energy M^2 and the "Pomeron mass" t, deduced from data on elastic (pp → pX) scattering, see eqs. (VI.14) and (VI.17) in the text.

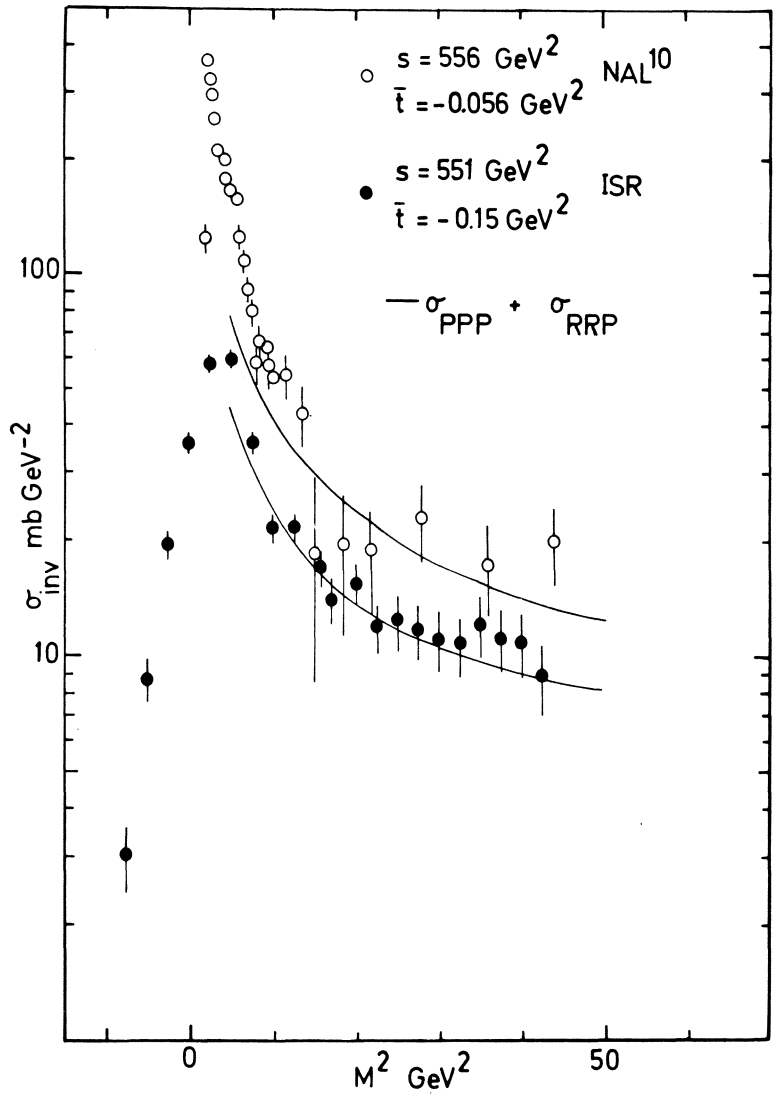

Fig. 12. The PPP cross-section obtained from ISR data (ref. 3) at $0.15 < t < 1.25$ GeV^2, extrapolated down to $t \simeq 0.056$ GeV^2 and compared to NAL data (ref. 5) at some total energy. The PPP line has been obtained in the range $5 < M^2 < 30$ GeV^2. At smaller masses other contributions enter, as suggested by the large peak at low t.

$$g_{PPP}(0) \simeq 0.4 \text{ GeV}^{-1}$$

This result is tentative and needs confirmation; ISR cannot easily contribute to its solution, due to the relatively short straight sections, making momentum measurements at small t very difficult to do.

The increase in σ_{TOT} with s observed recently naturally brings up the question as to which one(s) of the processes contributing to σ_{TOT} causes this dependence on energy. The rise in σ_{TOT} is 4.1 ± 0.7 mb between s = 551 and s = 2788 GeV^2. Subtracting the (rising) elastic cross-section we are left with a rise of 3.3 ± 0.7 mb to be accounted for by inelastic processes.

Consider first diffraction dissociation. We have seen that the inelastic peak in pp → pX roughly scales and that at small t the dependence on mass, $d\sigma/dM^2$, suggests something close to $1/M^2$. This suggests PPP dominance and hence we have proceeded to parametrize the data in this way after subtracting of the contribution of fragmentation protons and in a mass range where a) the contribution of fragments is reasonably small, $M^2 < 30 \text{ GeV}^2$, and b) where PPP dominates over any PPR terms, direct resonances or whatever, $M^2 > 5 \text{ GeV}^2$. The result thus represent a parametrization of the PPP content of the diffraction peak and hence by integrating it we whall get the triple-Pomeron part of the cross-section for diffraction dissociation. This is

$$E\frac{d^3\sigma}{dp^3} = \frac{s}{\pi}\frac{d^2\sigma}{dtdM^2} = \frac{G_{PPP}(t)}{16\pi}\left(\frac{M^2}{s}\right)^{1-2\alpha_P(t)}$$

$$\sigma = \frac{1}{16\pi}\iint G_{PPP}(t)\ z^{-1-2\alpha' t}\,dtdz$$

with $z = M^2/s$. The limits of integration are [m = m_p]

$$z_{min} = \frac{m^2}{s} \qquad z_{max} = \frac{(\sqrt{s} - m)^2}{s}$$

$$-t_{min} = \frac{m^2}{x}(1-x)^2 \simeq m^2\left(\frac{M^2}{s}\right)^2 \qquad -t_{max} = \infty$$

There are some delicate points about this integral, concerning the relevant range in mass and the influence of very small t. We shall not belabour this further here. To get an estimate we assume $t_{min} \simeq 0$ and $G_{PPP}(t)$ as given by eq. (VI.12). Then

$$\sigma_i = \frac{A_i}{32\pi\alpha_{\bar{P}}} \ln \frac{B_i - 2\alpha' \ln \frac{M^2_{min}}{s}}{B_i - 2\alpha' \ln \frac{M^2_{max}}{s}}$$

and this results in

$$\sigma(2788\ \text{GeV}^2) - \sigma(551\ \text{GeV}^2) \simeq 1.5\ \text{mb}.$$

Restricting the integration to e.g. $2 < M^2 < 50\ \text{GeV}^2$ results in 1.2 mb. Note that although we have obtained our PPP parameters in a restricted range of M^2 and t, we now extend the range in making the integral. Our tentative conclusion is that the PPP contribution to the rise in the diffraction cross-section is somewhere in the range 1 to 2 mb, and hence does not account for the entire rise in σ_{inel}.

Other contributions to the rise in σ_{TOT} could originate from:

1) $pp \to pX$ with $M_X^2 \lesssim 3$ GeV/c at small t. In this range terms other than PPP may contribute (see fig. 12).
2) π^+ and π^- production at $X \simeq 0$ and small p_T. At $p_T \gtrsim 0.1$ a small rise is observed.
3) At very large p_T there is a rise with increasing s in the invariant diff. cross-section for π-production.
4) $\bar{p}p$ production at $x \simeq 0$.

Data are not yet good enough to make quantitative estimates of the various contributions.

Acknowledgment

I am indebted to Mrs. M. Keller for taking excellent care of the manuscript, to S. v.d. Meer and K. Hubner for checking sections II.4, resp. II.5 and to member of the CERN/Holland/ Lancaster/Manchester collaboration fur useful comments.

SECTION VI

REFERENCES

1) A. Capella, SLAC-PUB-1198 (1973); A.B. Kaidalov et al., submitted to Phys. Letters; J. Gabarro and C. Pajares, LPTHE 73/17; R.G. Roberts and D.P. Roy, RL-73-065; M.G. Albrow et al., Nucl. Phys. B51, 388 (1972); and others.

2) M.G. Albrow et al., Nucl. Phys. B51, 388, (1972).

3) M.G. Albrow et al., unpublished.

4) J. Engler et al., contribution to the Aix-en-Provence Conference.

5) Childress et al., NAL preprint.